Local structure of lead halide perovskites for photovoltaic applications

Jiaxun Liu

Submitted in partial fulfillment
of the requirements of the Degree of
Doctor of Philosophy

September 2019

School of Physics and Astronomy
Queen Mary, University of London

Queen Mary
University of London

Statement of originality

I, Jiaxun Liu, confirm that the research included within this thesis is my own work or that where it has been carried out in collaboration with, or supported by others, that this is duly acknowledged below and my contribution indicated. Previously published material is also acknowledged below.

I attest that I have exercised reasonable care to ensure that the work is original, and does not to the best of my knowledge break any UK law, infringe any third party's copyright or other Intellectual Property Right, or contain any confidential material.

I accept that the College has the right to use plagiarism detection software to check the electronic version of the thesis.

I confirm that this thesis has not been previously submitted for the award of a degree by this or any other university.

The copyright of this thesis rests with the author and no quotation from it or information derived from it may be published without the prior written consent of the author.

.....

Jiaxun Liu

September 2019

The deuterated sample presented in chapters 4 and 5 was synthesised by Dr Peter Wyatt (School of Biological and Chemical Sciences). Neutron total scattering experiment chapter 4 was performed by Professor Martin Dove and

Dr Juan Du. Parts of chapter 3 has been previously published (Liu, J. et al. **2019** *Thermal Disorder and Bond Anharmonicity in Cesium Lead Iodide Studied by Neutron Total Scattering and the Reverse Monte Carlo Method*, The Journal of Physical Chemistry C. American Chemical Society, 123(24), pp. 14934–14940. doi: 10.1021/acs.jpcc.9b02936).

Abstract

Lead halide perovskites are becoming promising in the field of photovoltaics for their superior power conversion efficiency and simple synthesis. This thesis explores the structure of a wide range of perovskites, including hybrid organic-inorganic and inorganic perovskites using total neutron and X-ray scattering.

Local structure analysis of neutron total scattering data indicates that the Pb−I bonds in $CsPbI_3$ are extremely anharmonic, and thus it follows that all near-neighbour bond distributions are significantly asymmetric. The asymmetric distribution of nearest-neighbour Pb−I distances with a long tail, reflects an underlying anharmonic bond potential energy function which is well-represented by the Morse potential. The effect of anharmonicity was examined in the other two inorganic analogues $CsPbCl_3$ and $CsPbBr_3$ but with X-rays instead of neutrons. Local structures of these two materials do not show significant changes above the first phase transition temperature, but there is apparent peak splitting and merging in the diffraction patterns. Similar anharmonicity was observed by analysing the shape of the first Pb–X peak.

Rietveld refinement of the structure of the hybrid perovskite $MAPbI_3$ indicates the methylammonium cation remained disordered in both tetragonal and cubic phases and ordered in the low-temperature orthorhombic phase, but traditional crystallographic models are inadequate to describe the rotational disorder of the cation. Orientational distribution analysis of large configurations refined from total scattering data was applied to study the rotational behaviour across temperatures. Moreover, the flexibility of the PbI_6 framework and the anharmonicity of the Pb−I is reduced compared to that of $CsPbI_3$, which we attribute to the larger size of the methylammonium cation in the cavity. Additionally, the structural response of $MAPbI_3$ under pressure was

studied up to 1.8 GPa. The effect of pressure is comparable to the cooling effect, because the phase boundary in the pressure-temperature diagram is almost a straight line.

Acknowledgements

First, I would like to express my very great appreciation to my supervisors, Professor Martin Dove and Dr Anthony Phillips for their endless support and help. No matter what question I ask, they would point the direction for me to think and work out the solutions. The work presented in this thesis would not be possible without them at all. If I think back, those inspiring meetings became the best memory during my four years of PhD life.

I would like to offer my special thanks to Dr David Keen for his advice in data analysis. I am particularly grateful for the advice given by Professor Kostya Trachenko and Dr Alston Misquitta. Meanwhile, I wish to thank everyone in the CCMMP department for their help.

I wish to acknowledge our research group members for their helpful discussions, including Dr Juan Du, Dr Ling Wang, Zhengqiang Yang, Guanqun Cai, Mark Wilkinson, Ying Liu, Shurong Yuan, Lei Wang and Dr Helen Duncan. I would like to acknowledge my friends including Zhichao Weng, Chen Lyu for their company.

I would like to express my gratitude to the finiancial support by China Scholarship Council and Queen Mary University of London.

Finally, I am particularly grateful to my parents for their understanding and encouragement during my study. And I would like to thank my boyfriend Peide Zeng, who has been patient with my complaints all the time.

Contents

Chapter 1

Introduction

1.1 Perovskites: new photovoltaic materials

1.1.1 Background

The fast growth of the human population and economy poses a significant challenge on the capacity of current energy sources, especially if the trend keeps increasing. By 2050, the whole planet will need additional around 15 terawatts of energy far more than current capacity [1]. Many efforts have been made to search for renewable energy and escape the severe dependence on fossil fuels. For example, hydro, wind and solar energy are popular alternatives, due to the fact that they are clean and sustainable while the cost remains low. Regardless of different locations on the planet, almost every country has easy access to solar power. Therefore, this technology does have a huge potential to convert light into electricity for household uses.

The first generation solar cells are crystalline silicon solar cells [2] with an efficiency of over 26% [3]. They are still the mainstream of the photovoltaics market, despite the fact of being expensive and fragile. The second-generation solar cells are thin film solar cells, like cadmium telluride (CdTe) [4] and

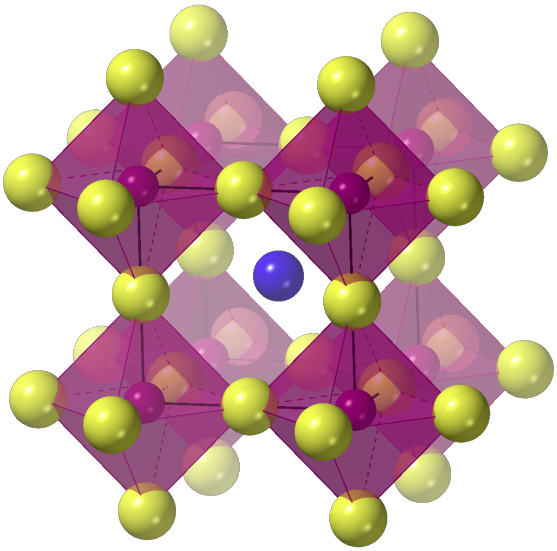

Figure 1.1: The aristotype cubic structure of perovskite material with the general formula ABX_3. The centre blue atom is the cation A, sitting in the cage of the B-centred BX_6 octahedra framework, where the B and X atoms are coloured purple and yellow.

$Cu(In, Ga)(Sn, Se)_2$ (CIGS). The certified power conversion efficiency (PCE) is relatively high above 20% [5], which makes them promising as solar devices. However, cadmium element is toxic when released, and the processing of such thin film materials under vacuum environment leads to additional cost. Dye sensitised solar cells (DSSC) [6] and perovskite solar cells (PSC) are so-called third-generation solar cells. Compared with commercial silicon solar cells, the development speed of PSCs has been extremely fast within the last nine years since the first report in 2009 [7, 8]. Apart from the high efficiency, there are many advantages related to PSCs, for example, low processing costs, exceptional photovoltaic properties and abundant natural elements for fabrication. However, PSCs also suffer the toxicity issue with the lead element and the stability of PSC-based solar cells is not comparable to traditional crystalline silicon solar cells. Nonetheless, the potential of PSCs in photovoltaic applications is still enormous, thus it is meaningful to study perovskites from

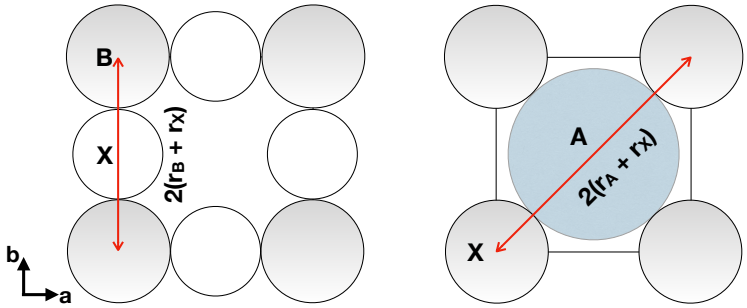

Figure 1.2: The hard sphere model for ideal cubic perovskite structure.

different physical and chemical aspects, to gain insights into the structure and better establish the foundation of the better design and full commercialisation of PSCs.

Perovskites refer to a family of materials with the general formula ABX_3. In 1839, German mineralogist Gustav Rose first discovered the mineral, calcium titanate ($CaTiO_3$), and then his Russian colleague Alexander Kämmerer named it perovskite [9]. After that, the term has been adopted for a series of compounds with the same basic structure. The parent cubic perovskite structure is formed by 8 corner-sharing BX_6 octahedra with cation A sitting in the centre. The anions, X are located at the vertices of the octahedron. The 'aristotype' perovskite structure ABX_3 is shown in figure 1.1. Albeit the 'aristotype' structure is the ideal cubic perovskite structure, symmetry-breaking distortions might occur, forming many different crystal structures [10]. The distortions from the 'aristotype' structure include four mechanisms: octahedral tilting, octahedral distortion, and A- and B-cation off-centering displacements. One of the most significant features of perovskite structures is they are topologically very stable and geometrically very unstable [11].

Goldschmidt proposed the idea of a 'tolerance factor' to study whether the ABX_3 perovskite structure is stable in terms of the ionic packing [12]. This model was later widely accepted as one way of explaining different perovskite

structures of many compounds. The Goldschmidt tolerance factor, t:

$$t = \frac{(r_A + r_X)}{\sqrt{2}(r_B + r_X)} \tag{1.1}$$

where r_A, r_B, r_X are the ionic radii of the cation A, cation B and anion X respectively. This equation is based on the hard-sphere model, as illustrated in figure 1.2. As shown in the figure, $a = \sqrt{2}(2(r_B + r_X)) = 2(r_A + r_X)$ holds. If we rearrange the order and cancel out the term 2 on both sides, $(r_A + r_X)/\sqrt{2}(r_B + r_X) = 1$, as shown in equation 1.1. Hence, we have the ideal cubic structure when $t = 1$.

The value of t determines whether an ion is compatible with the presumed crystal structure. If r_A is too big or r_B and r_X are too small, then $t > 1$ and A-cation can be too large to be accommodated that the material adopts a non-perovskite structure. The cubic structure is preserved if $0.9 < t < 1$ [13], but it will be distorted if $t < 0.9$. For example, the orthorhombic structure could be formed when the corner-sharing BX_6 octahedra tilt to fill the space. The orthorhombic structure has approximately the same a and c values as the cubic structure, but with around $\sqrt{2}b$ of the cubic structure. Attempts to predict structure stability on hybrid perovskites with this method has proved to be successful [14]. This model has been shown to hold true for solid solutions but it is something of an empirical guide that does not take into account, for instance, the shape of an organic A cation, and it does not even work well in the case of all inorganic perovskites. For hybrid perovskites, an extended tolerance factor has been proposed to account for the effective radii of the molecules [15].

The perovskite structure described above is three-dimensional, lower-dimensional perovskites have also aroused research interest due to more structural flexibility and excellent stability [16]. For example, two-dimensional perovskites are highly tuneable in terms of varying the thickness of the metal

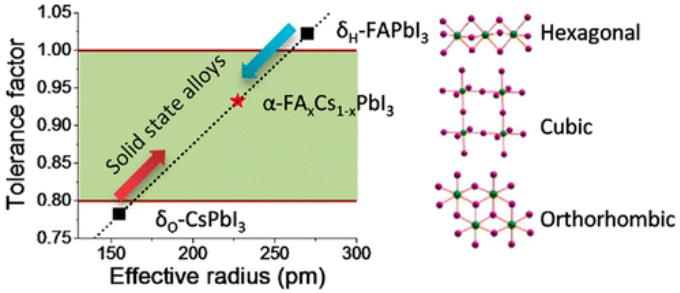

Figure 1.3: Goldschmidt tolerance factor for inorganic and hybrid perovskite structure. Cs atom as the A-site cation has a smaller radius, and the empirical factor is smaller than 0.8, so the formed structure prefers orthorhombic structure. On the other hand, the organic-inorganic perovskite $CH(NH_2)_2PbI_3$ is stable in the hexagonal structure, where $t > 1$ has been roughly assessed. By carefully tuning the tolerance factor, the desired perovskite structure can be stabilised. Graph from [14].

halide layer [17].

1.1.2 Inorganic perovskites

In the archetypal structure ABX_3 (figure 1.1), there is a wide range of possible A cations, including a single inorganic atom (for example, Cs^+) or an organic cation (for example, methylammonium $CH_3NH_3^+$ or formamidinium $CH(NH_2)_2^+$). The former one is called inorganic perovskite and the latter case is called hybrid perovskite. The choices for metal cation B and anion X could be extensive, however, only lead halides for photovoltaic application are discussed in this work.

The inorganic perovskite $CsPbI_3$ has a band gap E_g = 1.73 eV suitable for photovoltaic applications [18]. A band gap is defined as the distance between the bottom of conduction band and the top of valence band. $CsPbI_3$ has two stable phases, the well-known black perovskite phase and yellow non-perovskite phase with only edge-sharing octahedra. This δ-to-α phase transition has recently been exploited to create thermochromic photovoltaic windows with excellent stability [19]. The long-standing problem has been

how to achieve a stabilised black phase, and prevent it from transforming back to the more stable orthorhombic phase [20].

Recently, the stabilisation of the black phase of inorganic $CsPbI_3$ has been achieved through quantum-dot film synthesis, and it remained stable under ambient or even lower temperatures for several months. $CsPbI_3$ has been developed with an efficiency above 15%, after adding hydroiodic acid and phenylethylammonium iodide during synthesis [21]. Further details will be discussed in Chapter 3. In addition to solar cell applications, $CsPbI_3$ absorbs X-rays strongly and is a promising material for scintillators [22].

In addition to $CsPbI_3$, there are other inorganic perovskites including $CsPbBr_3$ and $CsSnI_3$. In terms of photovoltaic application, $CsPbBr_3$-based solar cells have exhibited high open circuit voltages [23].

1.1.3 Hybrid perovskites

In addition to the mentioned halide perovskites, there is also an enormous research interest on molecular perovskites when A or/and X are replaced by a molecular building unit [24, 25]. By far, the most extensively studied hybrid perovskites are still methylammonium lead halides $CH_3NH_3PbX_3$ (E_g = 1.7eV), where X is Cl^-, I^- or Br^-. Three phases have been identified, a low temperature orthorhombic phase, a room temperature tetragonal phase and a high-temperature cubic phase [26]. Another promising material is formamidinium lead iodide with a smaller band gap (E_g = 1.55eV), which allows broader absorption in the solar spectrum.

A mismatch of current has been found between the forward and reverse scan of the sweeping bias voltage, and the direction of this voltage seems to be significant in photocurrent current-voltage measurement on perovskite solar cells as well [27]. This discrepancy is the so-called current-voltage

hysteresis problem. This implies the device current not only depends on the present applied voltage but also on the past history of inputs. There are two possible explanations for hysteresis in hybrid perovskites. One is the motion of charged defects near interfaces [28], while the other comes from the ferroelectric polarisation of the organic components [29]. However, this has been challenged as no ferroelectricity is found experimentally for $MAPbI_3$-based solar cells at room temperature [30]. One of the experimental solutions is to replace organic cations with inorganic components and test if current-voltage hysteresis still exists [31]. The result is surprising, solar cells utilising inorganic perovskite (*e.g.,* $CsPbI_3$) still exhibited hysteresis, even though there is no polarisation in such materials.

Additionally, problems with long-term chemical stability and durability remain to be solved [32]. For example, $CH_3NH_3PbI_3$ ($MAPbI_3$) decomposes to CH_3I, NH_3 and PbI_2 when the temperature exceeds 80 °C for 20 minutes [33]. By contrast with $MAPbI_3$, sthe decomposition temperature of $FAPbI_3$ is higher [34], but with a less tendency to remain stable perovskite phases. The cubic perovskite transforms back to δ-phase at room temperature even in the inert gas atmosphere [35]. When it comes to size, the formamidinium cation is slightly larger than the methylammonium cation, and the tolerance factor should be higher in principle. We have to be careful here, as the size of molecules inside the cage, is difficult to define accurately due to their anisotropic shape [14]. Even more, these MA molecules undergo reorientation motion at high-temperature phase [36].

Hybrid perovskite solar cells are still at the top in terms of sunlight-to-electricity efficiency in the perovskites family. Indeed, such considerable interest in perovskites as photovoltaics originated from a published work by Miyasaka in 2009 [7]. Organic-inorganic lead halide perovskites, $MAPbI_3$ and $MAPbBr_3$ have been used as visible-light sensitisers in sandwich-like

solar cells, shown in figure 1.4 and by then, the efficiency was only 3.8%. However, it opened up many possibilities in the photovoltaics area to achieve better-performance solar devices.

The superior electronic properties exhibited by hybrid perovskites have attracted much interests. Low-carrier recombination rates [37–40], and long carrier diffusion length [41] are desired in solar-cell design, as they allow longer lifetimes and higher concentrations of charge carriers. Attempts have been made through improving the morphology of perovskite films [42], and optimising device architecture for performance [43] and the hybrid perovskite compositions [44, 45]. For example, doping the MA cation with some caesium has remarkably improved the device efficiency [46] .

Apart from experimental findings, theoretical analysis on perovskites sheds light on crystal and electronic structures from another point of view. Octahedral tilting in perovskites is universal, because of the nature of how these octahedra connect by the vertex. This inherent network flexibility has been shown to enable the formation of large polarons, and in turn, prolong the charge-carrier lifetimes [47]. Other than octahedral tilting, A-site and B-site off-center displacements and the orientational motions of the cation are believed to be the origin of the dynamic fluctuations of hybrid perovskites [48]. For example, NMR data have shown that MA ions reorient almost as freely rotating molecules in the cubic phase on the picosecond timescale [49]. The A-site cation undergoes orientational disorder at high temperatures, and the rotational dynamics has been shown to exhibit a similar trend to the electronic property changes, *e.g.*, dielectric permittivity [50]. Moreover, the coupling between the low-frequency modes of the inorganic PbI_6 framework and high-frequency modes of the organic cation have been studied using Raman scattering and first-principles calculations [51, 52]. These authors pointed out that, soft modes (imaginary component) are present at zone boundaries for in both inorganic

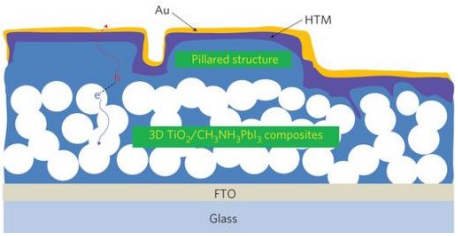

Figure 1.4: The heterojunction architecture of planar perovskite solar cells. The perovskite layer is used between the electron transport layer and hole transport layer, serving as the light absorber. The graph is taken from [53].

and hybrid perovskites.

1.1.4 Application in photovoltaics

For solar cells, two primary factors are of vital importance: the conversion efficiency and how the efficiency changes with time [54]. The latter is normally correlated with the degradation rate, a quantification of power decline over time [55]. Solar cells generally undergo degradation on exposure to moisture and ultraviolet radiation. Because a higher degradation rate translates directly into less power produced, we must know the rates to predict power delivery. Recent studies have determineds the mechanism of thermal degradation of $MAPbI_3$ as a function of temperature. The perovskite decomposes leaving only solid PbI_2 [33]. Researchers found that in two-dimensional perovskites, the moisture stability is more or less stable in contrast to three-dimensional perovskites, but the efficiency is still relatively low due to the difficulty in transforming excitons to free charge carriers. Furthermore, we need to consider other alternatives to lead in the hybrid perovskites for toxicity issues to both human and animals. Replacing lead with other metals, for example, Sn has also been explored, although hybrid perovskite $CH_3NH_3SnI_3$-based solar cells only achieved an efficiency as 5.73% [56].

1.2 Ordered crystal structures

Crystalline solids consist of repetitive atomic units in three-dimensional crystal lattices and are highly ordered. The infinite periodic arrays of points form a lattice. For unit cells, the region associated with each lattice point has an identical local environment. A primitive cell contains one lattice point only, and a conventional cell contains more than one lattice point. It should be noted the conventional cell is not the smallest unit cell.

Mathematically speaking, the position of any lattice point $\mathbf{r}$ can be found with respect to another point at position $\mathbf{r}'$ such that:

$$\mathbf{r} = \mathbf{r}' + i\mathbf{a} + j\mathbf{b} + k\mathbf{c} \tag{1.2}$$

where $\mathbf{a}$, $\mathbf{b}$ and $\mathbf{c}$ are three basis vectors and i, j and k are integers. This is known as translational symmetry.

1.3 Roles of disorder

In practice, crystalline solids are not always 'perfect' if that the symmetry is fully preserved due to experimental treatment or temperature changes. 'Perfect' implies the symmetry of structures is fully maintained. The diffraction pattern of a perfect crystal should give sharp Bragg peaks.

However, when atoms move about their equilibrium positions, a certain degree of disorder is introduced to the lattice. Correspondingly, the entropy increases. Thermal disorder increase as the temperature increases. In this case, the intensity of the diffracted beam will be reduced. The atomic displacement factor is used to describe such motions

$$DWF = \langle \exp(-8\pi^2 \langle u^2 \rangle Q^2) \rangle \tag{1.3}$$

where Q is related to the scattering angle 2θ and wavelength λ through

$$Q = \frac{4\pi \sin\theta}{\lambda} \tag{1.4}$$

Equation. 1.3 is restricted to the isotropic feature of harmonic potential. Of course, anisotropic parameters can be used in structure refinement if atoms vibrate with varying amplitudes in different directions. Because the harmonic approximation is not adequate when the anharmonic contribution to the lattice dynamics is not negligible. To visualise the anisotropic displacements, thermal ellipsoids are drawn to indicate atomic displacements and usually, have elongated shapes. It is an effective tool to estimate atom motions directly.

1.3.1 Orientational disorder

Orientational disorder refers to atoms or molecules that exhibit various orientational degrees of freedom. It is observed in several systems containing molecules, molecular ions or single atoms [57]. Examples include but not limited to adamantane [58] and tetrabromide [59]. The centre of mass of the molecules can be regarded as sitting on well-defined lattice points, but the orientations of molecules may be disordered due to the rotational degrees of freedom.

If the temperature is high or the potential that holds the molecules is weak, molecules rotate more freely, and the amplitudes of orientational motion become large. The system could become highly disordered. For example, in the cubic phase of $MAPbI_3$, the C–N axis in methylammonium ions exhibit fourfold rotational symmetry from neutron diffraction and quasi elastic neutron scattering study [60, 61]. But if the temperature is low and the potential to restrain the system is significant, molecules are localised but may reorient among symmetry-equivalent sites through quantum tunnelling. The orientation of molecules freezes when entering the low-temperature ordered phase. Initially,

the family of these materials were termed 'plastic crystals' by Timmermans, but later accepted as orientationally disordered solids [62].

A special case is sulfur hexafluoride (SF_6), which adopts a body-centred cubic structure that has been studied extensively due to the orientationally disordered phase between 96 and 223 K [63]. Most molecular crystals have a lower molecular symmetry than the site symmetry. In the case of SF_6, the site symmetry is identical to that of the molecule. It is reasonable to treat molecules as rigid bodies. X-ray diffraction and NMR shows the high-temperature phase could be orientationally disordered [64], but the origin is not fully understood. Later calculations confirmed the reorientation process but also suggested neighbouring molecules tend to orientationally order while next-neighbouring molecules strongly repulse each other and favour orientational disorder [65].

1.3.2 Site-occupancy disorder

In ideal crystals with no site-sharing, each atom occupies a crystal site with the probability of unity. However, when two or more atoms are present, there may exist some randomness on lattice sites. For example, after doping the sample by replacing half A atoms with B atoms, both atoms may occupy the site with a probability of 50%. This is often termed as site-occupancy disorder. Examples include metallic alloys and some non-stoichiometric compounds [66]. In some cases like alloys, two types of atoms could lead to superlattice ordering that changes the unit cell by some integer multiplication in one or more directions.

By refining the fractional occupancy in Rietveld refinement, the amount of atoms on specific sites can be estimated. However, it is often the case that diffraction data is insufficient to resolve this sort of problem using Rietveld refinement. In the fitting process, the diffraction intensities are fitted to those

from experimental diffraction data as a profile. Various parameters are involved while some can be highly correlated. One has to be careful here, instead of getting a more realistic refined value of site-occupancy, big anisotropic displacement factors (ADPs) might be given as the refined parameters.

Atomic motions in the crystals are often correlated that will influence the neighbouring atoms as well [67]. This influence is believed to shape many of the important physical and photovoltaic properties of the hybrid perovskite family. Hence, we need refinement techniques that don't implicitly assume no correlation in the system.

1.4 Framework of the thesis

The primary goal of this thesis is to study structural disorder in a range of perovskite materials for photovoltaic applications, while disorder is inevitable when perovskite-based solar cells function at working temperatures.

Chapter 1 gives a brief introduction to perovskite materials and disordered materials. It is followed by chapter 2, where detailed experimental and computational approaches are provided including neutron total scattering and atomistic simulation Reverse Monte Carlo (RMC) methods. Chapter 3 and 6 cover inorganic perovksites, $CsPbX_3$, where X = I, Br and Cl. In chapter 4, structural behaviour of the hybrid perovskite $MAPbI_3$ through phase transitions at varied temperatures were studied. The inorganic and hybrid perovskite share the same PbI_6 framework, hence the local interaction between the inorganic framework and organic or inorganic cations were directly compared. Also, high pressure was applied on the 'soft' perovskite $MAPbI_3$ in chapter 5, neutron diffraction data were collected to explore the phase transitions and the effect of pressure transmitting medium. Chapter 7 gives the conclusion of the work presented.

Chapter 2

Methods

This chapter introduces the methods used in this work. To investigate the local structures, neutron and X-ray total scattering experiments were carried out. The total scattering method, which incorporates both the Bragg diffraction and diffuse scattering data, is an extremely powerful way of studying the long-range and short-range order in a single experiment. Bragg and diffuse scattering data are collected as an integration over all energies for time-of-flight experiment. Bragg scattering data produce a time-averaged crystal structure. If we further take the diffuse scattering into account, this additionally gives the instantaneous structure with correlated motions of atoms. Total scattering data were analysed after multiple corrections and normalisation were performed, and many interesting features of the system become accessible. Beyond that, the RMC simulation method has been adopted to refine the configurations from initial models, through fitting of the experimental data.

2.1 Diffraction

2.1.1 Fundamentals

Crystallography represents the study of the periodic arrangements of atoms of crystalline materials. At the beginning, crystallography involved studying the macroscopic shape of crystals. The accidental discovery of X-rays by Röntgen in 1895 facilitated the generation of the first crystal diffraction pattern when X-rays were illuminated on a crystal by Von Laue in 1912. In the following year, W.M and W.L. Bragg used X-rays to solve the first crystal structure, sodium chloride (NaCl) [68].

The relationship between the diffraction pattern, and the structure put forward by the Braggs in its modern is given by:

$$\lambda = 2d_{hkl} \sin \theta_{hkl} \tag{2.1}$$

where λ is the wavelength of the radiation, d_{hkl} denotes the interplanar spacing. θ_{hkl} is the incident angle. Interplanar spacing describes the distance that separates different planes of atoms in the crystal. The lattice planes in reciprocal space are described by by three integers h, k, and l known as the Miller indices. Figure 2.1 shows two lattice planes in a cubic structure, the blue plane intercepts a, b and c axis at (0.5, ∞, ∞), the Miller indices are thereby calculated from the inverse of the intercepts (200). These three numbers are defined as the reciprocals of the intercepts along each reciprocal lattice vectors. Constructive interference of waves is observed. This is known as Bragg's law when equation 2.1 is satisfied.

Consider the scattering vector, $\mathbf{Q}$ as the change in wave vector of the radiation beam through the scattering process. Its modulus, $Q = |\mathbf{Q}|$. To achieve a higher Q_{max}, λ should be relatively small, e.g. 1 Å and that gives a Q_{max} roughly about 12.6 Å^{-1}.

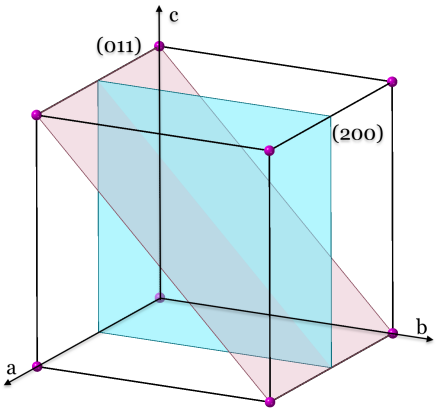

Figure 2.1: Planes with different Miller indices. The plane coloured pink denotes (011) and the blue one represents (200).

In pulsed spallation sources such as ISIS, the time-of-flight (TOF) diffraction technique is adopted. The detector is placed at a distance L from the source and counts the number of neutrons reached after each pulse [69]. Because neutrons have different velocities, different wavelengths can be distinguished by the flight time of each neutron according to the de Broglie equation

$$\lambda = \frac{h}{mv} \tag{2.2}$$

where h is the Planck constant. The relationship between time-of-flight t and wavelength λ is derived as

$$t = \frac{mL}{h}\lambda \tag{2.3}$$

where m is the neutron mass. Combining with equation 2.1, equation 2.3 becomes

$$t = \frac{mL}{h}2d\sin\theta \tag{2.4}$$

The scattering angle remains unchanged during the process. The diffraction pattern arises due to the different neutron wavelengths.

In principle, the scattering intensity of the radiation beam from a single particle will be a function of Q. This Q-dependence is determined by the Fourier transform of the interaction potential. For X-rays, the length scale

of the potential is set by the length scale of the electron density, so that the intensity will be strongly dependent on the magnitude of Q. On the other hand, for neutrons the interaction potential with the nucleus is virtually point-like compared to the size of the atom, so effectively the scattering power is independent of Q. The quantity is called neutron scattering length, b, the value of b does not change linearly with atomic number and is isotope specific.

2.2 Neutrons and X-rays

2.2.1 Basic properties

Traditionally, there are several scattering techniques available to determine crystal structures. Probe choices include beams of electrons, neutrons and electromagnetic radiation in the X-ray spectrum. Neutrons have the lowest energy among these probes, X-rays have much higher energy by 6 orders of magnitude at least. The key point is that they need to have a comparable or smaller wavelength to the spacing between atoms to better study the microscopic behaviour of matter. However, there exist a few differences, making each other a complementary method for structural characterisation.

The usefulness of neutrons in science can be appreciated from four points. Firstly, the wavelength of neutrons is comparable to interatomic distances of many materials. Neutrons have wave-like properties, and the wavelength λ can be calculated given its velocity v, from equation 2.2. Here, cold and thermal neutrons, with wavelengths of 1–30 Å(see table 2.1), become extremely useful. Hot neutrons are better for small lattice spacing materials, while thermal/cold neutrons have lower energy and are better for bigger lattice spacing materials. Secondly, neutrons do not have an electric charge and thus can penetrate deeper into a sample without the Coulomb barrier to overcome. Meanwhile,

Source	Energy (E/meV)	Temperature (T/K)	Wavelength (λ/Å)
cold	0.1 – 10	1 – 120	30 – 3
thermal	5 –10	60 – 1000	4 – 1
hot	100 – 500	1000 – 6000	1 – 0.4

Table 2.1: Approximate values for the range of energy, temperature, and wavelength for three types of source in a reactor [70].

neutrons do not damage the sample unlike X-rays. X-rays are scattered by electrons instead of nuclei, so the intensity of scattering increases as the atomic number gets larger. For neutron scattering, the scattering from atomic nuclei does not correlate with the atomic number. Thus, it is advantageous to use neutrons rather than X-rays to distinguish the light atoms like hydrogen, which have far fewer electrons than heavy atoms do. Thirdly, the neutron carries a spin of 1/2, making it an ideal probe for investigating magnetism. Fourthly, the energy of thermal neutrons is approximately the same order of most excitations. The energy changing between scattered energy and incident energy describes these excitations.

This is not to say that neutrons are superior to X-rays. It is apparent neutrons that can locate light atoms while it is difficult for X-rays. Indeed, hydrogen atoms are undesirable for neutron diffraction or total neutron scattering because they have a huge incoherent cross section due to spin effects, and it is often necessary to use deuterated samples to reduce the impact. Furthermore, lower amounts of sample are required to perform an X-ray diffraction experiment than in neutrons experiments. Neutrons and X-rays can both provide structural information, but different atoms would have various contributions in each case. Hence, they can be combined as complementary in providing distinct information about the crystal structure.

2.2.2 Neutron and X-ray sources

Ever since 1945, the nuclear reactor has been developing at a quick pace, and this opens up many possibilities for neutron diffraction studies. The mechanism of producing neutrons in reactors is through nuclear fission. When a neutron is captured by a nucleus (normally uranium-235 or plutonium-239), it splits into two fragments and releases 2 or 3 neutrons with high energy in reactors.

$$ {}^{1}_{0}\mathrm{n} + {}^{235}_{92}\mathrm{U} \longrightarrow {}^{236}_{92}\mathrm{U} \longrightarrow {}^{141}_{56}\mathrm{Ba} + {}^{92}_{36}\mathrm{Kr} + 3\,{}^{1}_{0}\mathrm{n} $$

$$ {}^{1}_{0}\mathrm{n} + {}^{235}_{92}\mathrm{U} \longrightarrow {}^{236}_{92}\mathrm{U} \longrightarrow {}^{140}_{54}\mathrm{Xe} + {}^{94}_{38}\mathrm{Sr} + 2\,{}^{1}_{0}\mathrm{n} $$

A stable chain reaction will be formed if the mass of fissile materials has been chosen carefully. Cooling moderators are placed before the diffractometers, and then produce usable wavelengths for each instrument. The other way of producing a neutron beam is a spallation source. Protons are accelerated in linear accelerator or synchrotron to gain high energy, before hitting a heavy metal target. Neutrons are knocked out from the target, and they have to be decelerated through collisions with light atoms to lose energy. Typically light atoms, such as liquid hydrogen or solid methane are used to reduce the velocities of fast neutrons quickly. ISIS is one of the highest-flux pulsed spallation neutron sources in the world and has two target stations as shown in Figure 2.2. The useful Q_{max} can be achieved up to 50-60 $\mathrm{\AA}^{-1}$ [71].

There are two ways of generating X-rays, in-house sources and synchrotron facilities. A synchrotron light source usually consists of linear accelerator (linac), booster synchrotron and storage ring. The synchrotron produces X-rays when electrons move at a speed near that of light and are made to change direction by a magnetic field. To divert the course of those electrons, bending magnets are placed inside the storage ring. Third-generation synchrotrons,

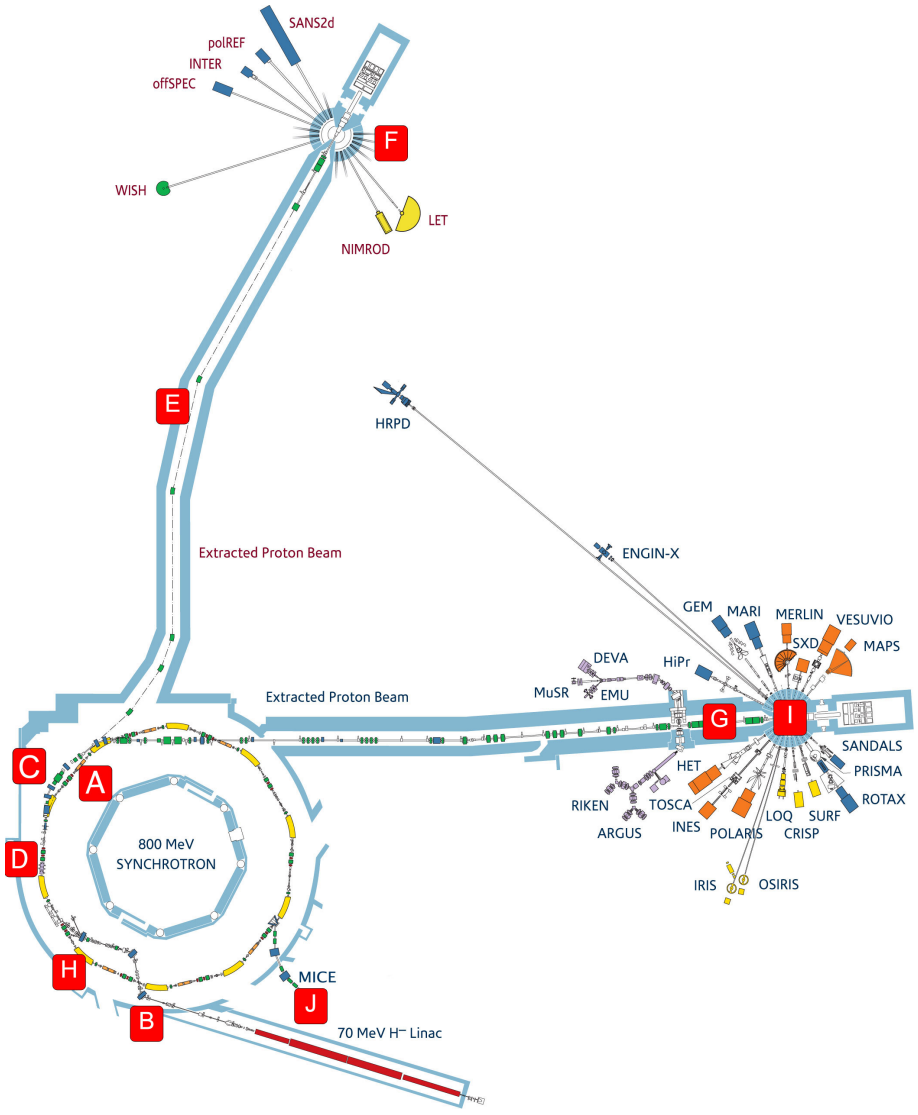

Figure 2.2: The layout of ISIS neutron and muon source at the Rutherford Appleton laboratory, UK. Target station 1 is located to the right of the synchrotron, while target station 2 is at the top in the graph. Graph taken from reference [72].

such as the Diamond Light Source in the UK, use wigglers and undulators to get stable and higher energy electron beams, without losing too much energy by following a wiggling path. The brightness of emitted X-rays is extraordinarily high, making it competitive for high-resolution study on crystallographic studies [73].

2.3 Rietveld refinement

Crystal structures are best solved by growing single crystals as the diffraction pattern would include every *hkl* that satisfies the Bragg's condition. But in polycrystalline materials, random orientations of the crystallites would be averaged, and all the symmetry-equivalent reflections that correspond to the same d-spacing or the same Q are contained in a single peak. The problem of powder diffraction data is that peaks with the same $h^2 + k^2 + l^2$ overlap. However, large and high-quality single crystals are not easily synthesised because of experimental limits.

The Rietveld refinement method was first published in 1969 [74] and is a method of profile refinement on powder diffraction patterns. It is designed to fit the complex profile and solve the overlapped-reflections problem. Instead of trying to extract intensity for each Bragg reflection, Rietveld used the total profile intensity for the refinement at once. The Rietveld method exploits a least squares approach to refine a computed line profile until it matches the measured profile. The refinement minimises M as in routine least-squares refinement, which is

$$M = \sum_i \omega_i (y_{io} - y_{ic})^2 \tag{2.5}$$

where y_{io} and y_{ic} represent observed and calculated intensity respectively. The sum is over all the independent observations with the weight factor ω_i of each point. To judge the goodness of the fit, the weighted profile R-factor R_{wp} is

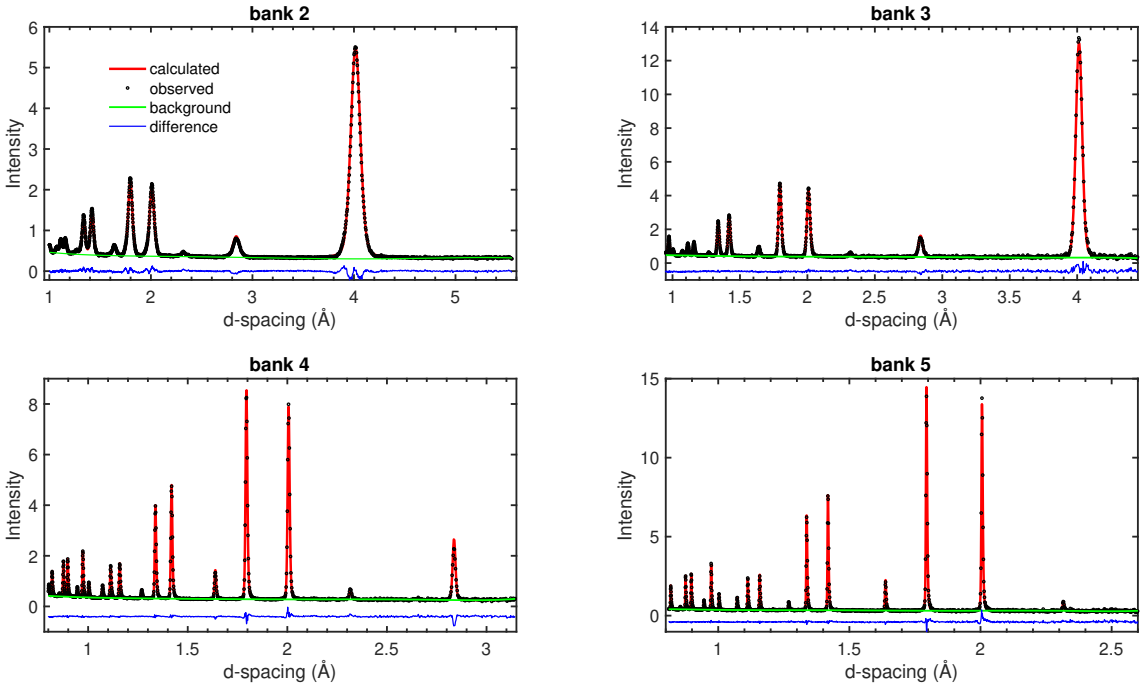

Figure 2.3: A representative good fit of ScF_3 from Rietveld refinement. Data were collected on POLARIS, ISIS, which has 5 detector banks at different angles. Bank 2–5 have been refined and plotted. The higher the scattering angle is, the lower d-spacing region that bank covers. Neutron diffraction data is provided by Martin Dove.

chosen to show the discrepancy in a straightforward way. It is defined as

$$R_{wp} = \sqrt{\sum_i \omega_i (y_{io} - y_{ic})^2 / \sum_i \omega_i y_{io}^2} \tag{2.6}$$

where the M score is scaled by the weighted intensities [75]. The R_{wp} factor emphasises peaks with intense intensity over the background, so it could be a bit misleading if a significant background exists in the diffraction data and the R_{wp} would become relatively small. The best way to decide how good the fitting is would be a direct comparison by eye and also whether the model is physically plausible.

In all the work presented, the EXPGUI interface of the GSAS package combined with GSAS-II package were used [76, 77].

Background is determined in two ways. On one hand, it can be refined by a polynomial function with many refinable parameters. The Chebyschev function

is the most common one in refining the background, and the refinement tends to be more stable because the terms are orthogonal. For more complex background, interpolation between selected points on the diffraction pattern is preferable for a better fitting [78].

Instrument parameters are often used to refine the positions of Bragg reflections. In time-of-flight neutron diffraction experiment, the time-of-flight t is calculated from the d-spacing of the Bragg reflections based on

$$t = \mathrm{DIFC}d + \mathrm{DIFA}d^2 + \mathrm{ZERO} \tag{2.7}$$

where the three coefficients are the diffractometer constants [79]. The first constant DIFC has an approximately linear relationship with d-spacing and could be estimated from equation 2.3. The constant DIFC is fixed and could be refined with a multi-histogram data collection experiment. The second constant, DIFA adds a small modification that allows small shifts due to the sample absorption. The constant ZERO should be fixed for each instrument.

The peak shape in Rietveld is described by the pseudo-Voigt approximation [80], a combination of Gaussian and Lorentzian functions, for constant wavelength X-ray and neutron data. It applies well to synchrotron data, but neutron time-of-flight (tof) data is more complicated and extra consideration is required. The spectrum of the pulsed neutrons indicates the intensity is strongest at low times-of-flight, and the intensity would fall off at longer t. One approach is to convolve two back-to-back exponentials with the pseudo-Voigt function to describe the decayed intensity. The full widths and at half maximum are parameterised to model a more accurate shape [79]. The Gaussian and Lorentzian widths are given in equation 2.8 and equation 2.9 respectively.

$$\sigma^2 = \sigma_0^2 + \sigma_1^2 d^2 + \sigma_2^2 d^4 \tag{2.8}$$

$$\gamma^2 = \gamma_0^2 + \gamma_1^2 d^2 + \gamma_2^2 d^4 \tag{2.9}$$

σ_0 and γ_0 are instrument dependent, so the other profile coefficients σ_1 and γ_1, or even σ_2 and γ_2 can be refined to model the size broadening. For neutron tof data, four profile functions have been described in GSAS package. Depending on the instrument design, the profile function may be different.

Figure 2.3 shows the diffraction pattern at different instrument banks. The resolution of each bank is decided by the partial differentiation of equation 2.3, where $\Delta d/d \approx$ constant. So Δd is bigger at high d values, and the θ is lower from Bragg's law. This explains that at lower angles, the instrumental broadening is worse than at higher angles.

The number of refinement parameters should be kept as small as possible, to avoid refinement diverging or falling into false local minima instead of the desired global minima. Due to thermal vibrations, atoms deviate from their average positions through isotropic or anisotropic mean displacements. The effect of the atomic displacement parameters (ADPs) is to decrease the intensities of those Bragg peaks. In equation 1.3, this is achieved by multiplying the expected diffraction pattern by the atomic displacement factor that describes the atoms looking larger. The ADP is usually below 0.1 Å for all atoms and any value bigger than that might be unrealistic [81]. However, the displacement parameters might be refined as negative values sometimes, and it is clear these values are not physically sensible. This is because some atoms have big absorption coefficients, and the absorption correction parameters are coupled with ADPs during the refinement cycle. The solution is to have proper absorption correction first and those ADPs could be refined at a later stage.

2.4 Instruments

Four diffractometers from both ISIS and Diamond facility have been used in this work. The General Materials Diffractometer (GEM) at ISIS is designed for

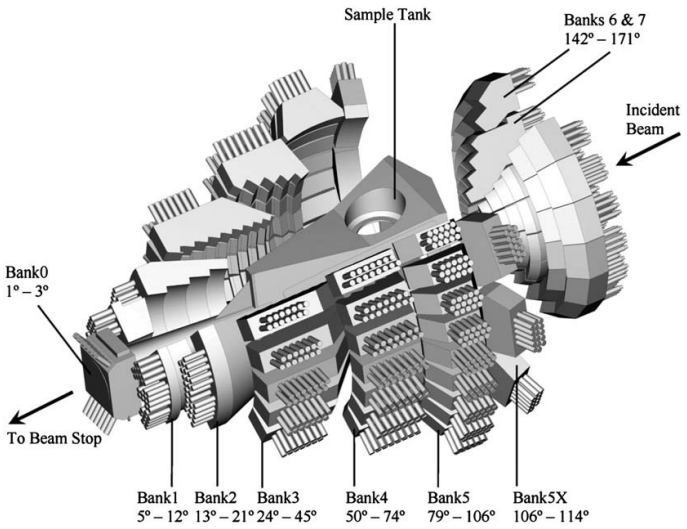

Figure 2.4: The sketch of the GEM diffractometer. There are 8 banks covering a wide range of scattering angles, although data from the lowest angle bank are usually not used in data analysis due to its low-resolution. Graph taken from reference [82].

good-resolution, high intensity neutron experiments. It covers a wide range of scattering angles from 1.1°to 169.3°, achieved by including eight detector banks, shown in figure 2.4. The incident flight path L_1 = 17.0 m , allows a high resolution in reciprocal space leading to accurate structural information [82]. Total scattering and diffraction measurements are carried out routinely on this instrument.

One other instrument, POLARIS is a high intensity powder diffractometer with five detector banks. The incident flight path is 12 m, shorter in length when compared to the L_0 of GEM and making it a medium-resolution diffractometer. It is an ideal instrument for studying materials under non-ambient conditions, with short counting times for data collection particularly good with relatively small samples, e.g. 1 mm^3. The sketch of the POLARIS instrument is given in figure 2.5.

The PEARL instrument is designed for in-situ high-pressure studies using a Paris-Edinburgh cell [84]. The Paris-Edinburgh cell is composed of two opposed tungsten carbide anvils to deliver pressure on the sample placed in

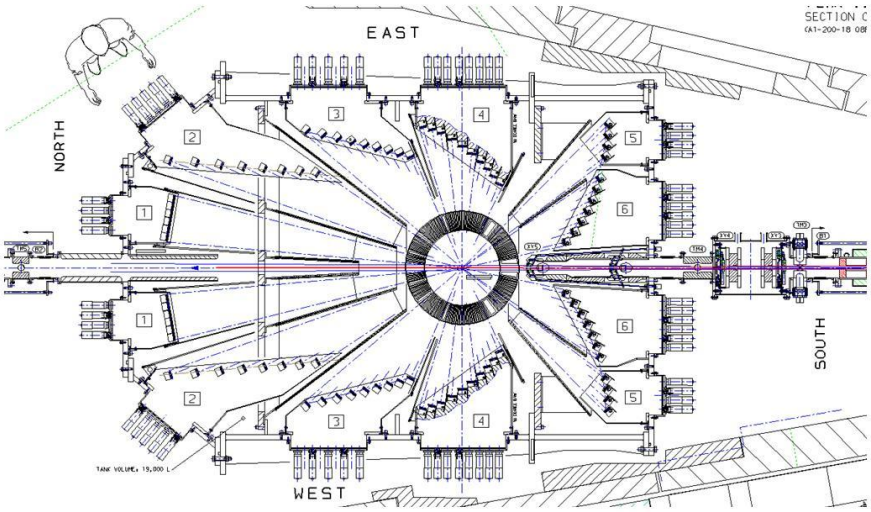

Figure 2.5: The POLARIS diffractometer at ISIS, and six detectors bank positions are numbered in the graph. Graph taken from reference [83].

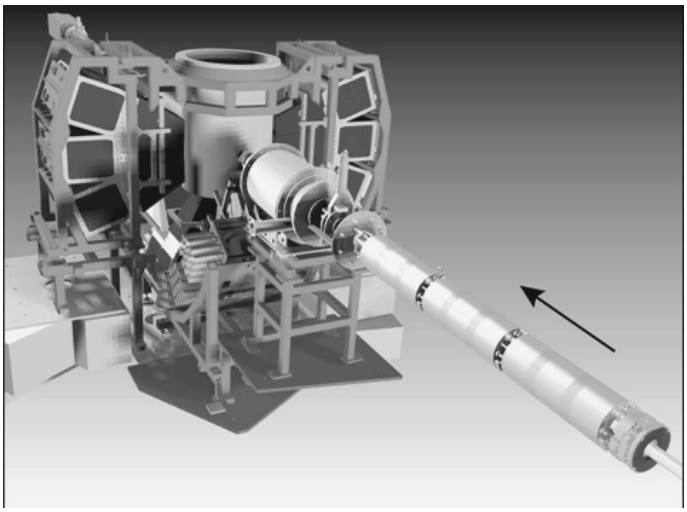

Figure 2.6: The PEARL diffractometer at ISIS. The incident beam passes the pipe from the direction of the arrow on the low-right-hand side, and arrives at the Paris-Edinburgh cell where sample is mounted. Graph taken from reference [84].

between. The pressure can go up to ca. 30 GPa at room temperature, with temperature ranging from 80 to 1400 K, making it applicable on a broad range of extreme-condition studies.

Apart from instruments at ISIS total scattering experiment has also been carried out at the XPDF (I15-1) beamline at Diamond. XPDF is capable of

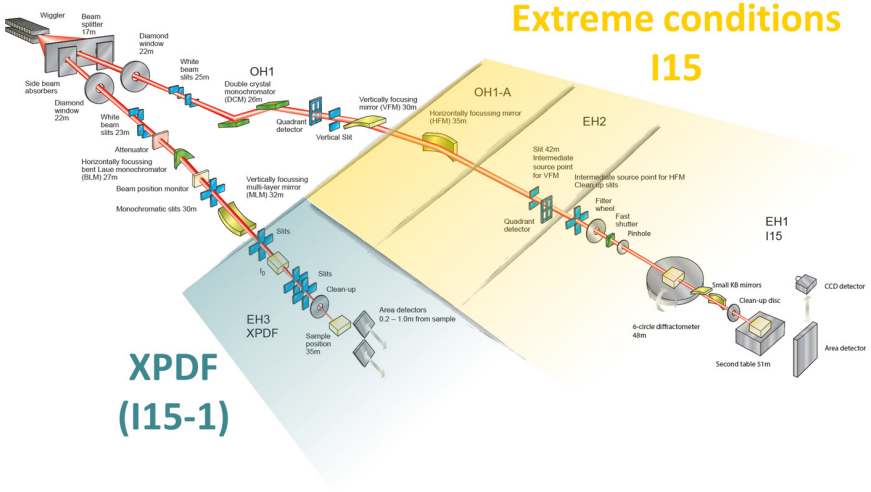

Figure 2.7: The XPDF beamline at Diamond. The synchrotron beam splits to two beams, one arrives at I15 for extreme conditions (extreme pressures and temperatures) while the other at I15-1 for total scattering experiments. Graph taken from reference [85].

producing high quality PDF data with high Q_{max} (35Å) and high flux. Two large area detectors, as in figure 2.7 collect PDF and Bragg data separately. The Bragg detector is placed further away, and the PDF detector is placed near the sample to collect the weaker diffuse scattering. It is designed for local structure studies with X-ray pair distribution functions.

2.5 Powder sample synthesis

2.5.1 $CsPbI_3$ sample preparation

The powder sample of $CsPbI_3$ was synthesised following a synthesis route of its analogue $CsPbBr_3$ [86]. First, 0.15 mol $Pb(NO_3)_2$ and 0.3 mol KI were dissolved separately in 100 mL of boiling water and 50 mL water, and then mixed by stirring while cooling over 15 minutes. The yellow precipitate of PbI_2 was collected by filtration and washed repeatedly with ethanol, and dried overnight under vacuum at room temperature. Second, 20 mmol prepared PbI_2 was dis-

solved in 30 mL 48% aqueous HI before adding 20 mmol CsI aqueous solution to it, leading to immediate precipitation of yellow solid. With the same collection method, the solid was collected and dried overnight. The yellow powder sample, in figure 2.8 a was ground into fine powder for diffraction experiments.

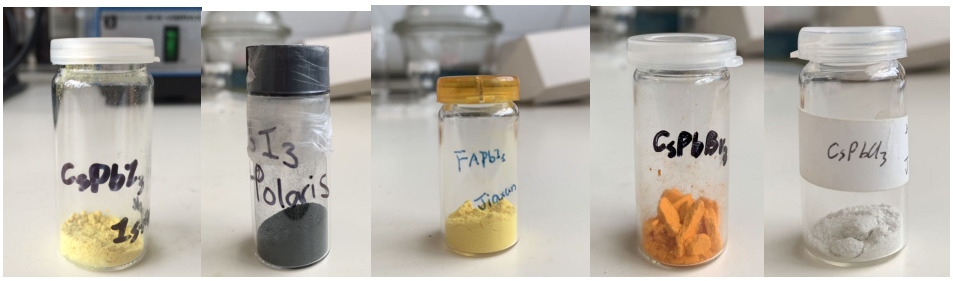

(a) (b) (c) (d) (e)

Figure 2.8: Samples prepared for each experiment. From left to right: (a) Yellow powder sample of $CsPbI_3$. (b) Deuterated black powder sample of hybrid perovskite $MAPbI_3$. (c) Deuterated yellow powder sample of hybrid perovskite $FAPbI_3$. (d) Orange powder sample of $CsPbBr_3$ and (e) White powder sample of $CsPbCl_3$.

2.5.2 $MAPbI_3$ sample preparation

The deuterated powder $MAPbI_3$ sample was synthesised using a similar method to that of Method 1 [87]. A solution of deuterated methylamine CD_3ND_2 was made from CD_3ND_2 gas dissolved into deuterated water in an ice bath environment under an ambient atmosphere. Then deuterated lead (II) acetate was dissolved in deuterated hydroiodic acid (DI) solution. The two solutions were added together to react while heated in an oil bath. The sample of $CD_3ND_3PbI_3$ was formed as a black precipitate while cooling from 100°C to 50°C over 5 hours. Then it was filtered and dried overnight. An excess amount of iodine sublimed from the product and could be observed in the container. The phase purity was confirmed by an X-ray powder diffraction measurement (Cu Kα radiation). The sample was held in a sealed glass container to avoid it

reacting with humid air. It was dried before being ground and transferred into a thin-walled vanadium can of diameter 8 mm for the neutron total scattering measurements. These latter operations took place within a glove box containing a dry atmosphere. The black powder sample is shown in figure 2.8 b. This deuterated sample was synthesised by Dr Peter Wyatt.

2.5.3 $FAPbI_3$ sample preparation

The method for sample preparation was taken from the reference [88]. The first step is to fully deuterate the formamidinium iodide (FAI, 4 g) in the powder form by dissolving in 250 ml of D_2O (99.9%). The mixture was heated to $94^{\circ}C$ in the rotary evaporator, sitting in the silicone oil bath under flowing nitrogen. The condensed was placed to prevent solution loss. Then the mixture liquid was evaporated at a reduced temperature, $70^{\circ}C$ under the nitrogen flow for 8 hours. White solid was collected and further dried at $100^{\circ}C$ for almost 2 hours. Then the deuterated FAI (1.22 g) and the powder PbI2 (99.999%, 3.13 g) and 1 mL D_2O were added to the γ-butyrolactone (10ml). The mixture liquid was fully dissolved by heating up to 150 $^{\circ}C$ using a hotplate in the glove box for 12 hours until the black solid $FAPbI_3$ was precipitated. The sample was cooled to room temperature and collected. The powder sample is shown in figure 2.8 c.

2.5.4 $CsPbBr_3$ and $CsPbCl_3$ sample preparation

Furnace synthesis of $CsPbCl_3$ has been previously reported [89] and was used in this experiment. 10 mmol CsCl and 10 mmol $PbCl_2$ was weighed and then sealed in an evacuated Pyrex tube. The sample was melted at 823 K for 3 h, and then annealed at 753 K for 1 day and 573 K for 1 day. The crushed sample was then measured using laboratory X-ray diffraction, and the diffraction pattern confirmed the sample was $CsPbCl_3$.

$CsPbBr_3$ was synthesised using a solution method [86]. First, 0.015 mol $Pb(CH_3CO_2)_2$ and 0.03 mol KBr were dissolved separately in 10 mL of boiling water and 5 mL water, and then mixed by stirring while cooling over in 15 minutes. The white precipitate, $PbBr_2$ was collected by filtration and washed repeatedly with ethanol, and dried overnight under vacuum. 5 mmol of the prepared $PbBr_2$ was dissolved in 15 mL 48% aqueous HI before adding 10 mmol CsBr dissolved in 10mL H_2O, leading to immediate precipitation of an orange solid. With the same collection method, the solid was collected and dried overnight. Here, it should be pointed out, the stoichiometry of CsBr and $PbBr_2$ is 2:1 instead of 1:1, as the former method leads to form the stable $CsPb_2Br_5$ rather than the desired $CsPbBr_3$ sample [90].

2.6 Total scattering method

2.6.1 Formalism

In recent years, one approach has emerged as the solution to provide complimentary information on liquids and amorphous materials, called total scattering analysis of X-ray and neutron scattering data [91]. It is also utilised as an approach to understand disordered crystalline materials. As the name implies, total scattering is a combination of the collected Bragg and diffuse scattering over all scattered energies. The diffuse scattering is the scattering that arises from the local (short range) configuration of the material and it can be difficult to quantify because of the wide variety of effects that contribute to it. Traditional crystallographic structure analysis approach like Rietveld analysis only give information about the long-range average structure of the material. Bragg scattering occurs when scattering amplitudes add constructively, while PDF uncovers the short-range, instantaneous local structure. The

PDF is collected through performing Fourier transform on the corrected and normalised total scattering data.

Here we introduce a brief description of the neutron total scattering theory. As is often the case, the scattering function is related to the Fourier transform of the density, $\rho(\mathbf{r})$ though a function called the structure factor:

$$F(\mathbf{Q}) = \int \rho(\mathbf{r}) \exp(i\mathbf{Q} \cdot \mathbf{r}) d\mathbf{r} = \sum_j b_j \exp(i\mathbf{Q} \cdot \mathbf{r}_j) \tag{2.10}$$

where b_j is the scattering length. Instead of measuring $F(\mathbf{Q})$ directly, the scattered intensity is proportional to $|F(\mathbf{Q})|^2$:

$$S(\mathbf{Q}) = \frac{1}{N} |F(\mathbf{Q})|^2 = \frac{1}{N} \sum_{j,k} b_j b_k \exp(i\mathbf{Q} \cdot \mathbf{r}_{jk}) \tag{2.11}$$

where $\mathbf{r}_{jk} = |\mathbf{r_j} - \mathbf{r_k}|$, When performing a time average over all fluctuations, the equation 2.11 then becomes:

$$S(\mathbf{Q}) = \frac{1}{N} \sum_{j,k} b_j b_k \left\langle \exp(i\mathbf{Q} \cdot \mathbf{r}_{jk}) \right\rangle \tag{2.12}$$

This is the equation we will use, but more generally there exists the dynamic scattering function which accounts for correlations between atom positions at different times:

$$S(\mathbf{Q}, \omega) = \frac{1}{N} \sum_{j,k} b_j b_k \int \exp(i\mathbf{Q} \cdot \mathbf{r}_{jk}(t)) \exp(-i\omega t) \mathrm{d}t \tag{2.13}$$

Its time Fourier transform is

$$S(\mathbf{Q},t) = \int S(\mathbf{Q},\omega) \exp(i\omega t) \mathrm{d}\omega = \frac{1}{N} \sum_{j,k} b_j b_k \exp(i\mathbf{Q} \cdot \mathbf{r}_{jk}(t)) \tag{2.14}$$

when t = 0, equation 2.14 becomes equivalent to equation 2.15. $S(\mathbf{Q})$ indicates the instantaneous correlations between the neighbouring atoms. Furthermore, this is equivalent to performing the integration over all scattered energies:

$$S(\mathbf{Q}) = \int S(\mathbf{Q}, \omega) \mathrm{d}\omega \tag{2.15}$$

Since we will carry out powder diffraction experiments, there will exist all possible orientations of the crystals within the sample. Hence the orientational average of Q and r needs to be performed:

$$\left\langle \exp(i\mathbf{Q}\cdot\mathbf{r}_{jk})\right\rangle = \frac{1}{4\pi}\int_0^{2\pi} \mathrm{d}\phi \int_0^{\pi} \exp(iQr_{jk}\cos\theta)\sin\theta \mathrm{d}\theta \tag{2.16}$$

Through calculating this integral, equation 2.16 becomes:

$$S(Q) = \frac{1}{N}\sum_{j,k} b_j b_k \frac{\sin(Qr_{jk})}{Qr_{jk}} \tag{2.17}$$

$S(Q)$ is then divided into two parts

$$S(Q) = \frac{1}{N}\sum_{j} {b_j}^2 + \frac{1}{N}\sum_{j\neq k} b_j b_k \frac{\sin(Qr_{jk})}{Qr_{jk}} \tag{2.18}$$

The first part, the case when $j = k$, is the self scattering. This term needs to be subtracted as it contains no information about the correlated information from atom-pairs. The second term describes the interference between different atoms.

First we define $4\pi r^2\rho_n \mathrm{dr} \times g_{mn}(r)$ as the number of pairs of atoms of types n with separation between r and $r + dr$, where ρ_n represents the overall number of atoms of type n per volume. Then the second term can be calculated as

$$\frac{1}{N}\sum_{j\neq k} b_j b_k \frac{\sin(Qr_{jk})}{Qr_{jk}} = 4\pi\rho \int \sum_{m,n} c_m c_n b_m b_n r^2 g_{mn}(r)\frac{\sin(Qr)}{Qr}\mathrm{d}r \tag{2.19}$$

The probability function $g_{mn}(r)$ will be 1 when the radius, r, approaches infinity, and this will give a δ-function at $Q = 0$ in the Fourier transform. Therefore it is better to subtract 1 from the probability function

$$i(Q) = 4\pi\rho \int \sum_{m,n} c_m c_n b_m b_n r^2 (g_{mn}(r) - 1)\frac{\sin(Qr_{jk})}{Qr_{jk}} dr = S(Q) - S_0 - S' \tag{2.20}$$

where S' represents the self term and S_0 is the delta function at $Q = 0$. Now the pair distribution functions can be defined

$$D(r) = 4\pi\rho r \sum_{m,n} c_m c_n b_m b_n (g_{mn}(r) - 1) \tag{2.21}$$

This is actually the Fourier transform of the function $Qi(Q)$. Researchers from many subjects use total scattering to study different things, in order to avoid the confusion a set of different definitions on total scattering functions have been explicitly compared in reference [92].

2.6.2 Experiments

A total scattering experiment collects Bragg scattering and diffuse scattering data concurrently. There are three points to be made for performing such an experiment. First, the scattering vector, Q, should be collected as high as the neutron or synchrotron source allows. This ensures that high quality scattering data will be obtained, with the resolution given by $\Delta r = 2\pi/Q_{\max}$. A high value of $Q_{\max}$ is desirable. Furthermore, the termination ripples introduced by the finite $Q_{\max}$ are suppressed. Second, all the energy-changing process should be collected to obtain a good integration of all the energies [93]. Third, scattering other than from the sample should be minimised. This refers to the background scattering, which primarily contains three scattering measurements. The scattering from the sample container, the sample environment, and the instrument.

Placing the data on an absolute scale makes the comparison between different datasets reliable. It can be achieved by normalising the diffraction data with the same quantity. Vanadium is known to have a small coherent scattering length, an ideal material as the sample container in neutron scattering. The main contribution is fro m the incoherent neutron scattering, which does not change too much with Q and has very few Bragg peaks. Therefore, data collection on a vanadium rod can be treated as the calibration constant.

2.6.3 Total scattering data correction

Data from total scattering experiments are raw radiation counts, and they need to be corrected to extract the normalised differential cross section $\sum_i c_i \bar{b}^2 / 4\pi$. In this thesis, all the raw data correction was performed using Gudrun. The Gudrun suite was developed by A.K Soper and has been widely used at ISIS and Diamond as the data reduction software [94]. It has two subprograms called GudrunN and GudrunX, for neutron and X-ray data respectively.

Figure 2.9 shows the workflow of the Gudrun software. The scattering data are first normalised to the incident beam monitor, which is essential to compare between different datasets because the incident intensity of radiation may not be the same. After proper monitor normalisation, the scattering from the background should be subtracted to obtain the sample differential cross section. Attenuation and multiple scattering are approximately calculated from the table of total cross-section. Gudrun analyses the scattering data from detector to detector and combines the detectors to obtain a single merged spectrum from all detector banks. By performing an inverse Fourier transform, the scattering function $i(Q)$ is then transformed to r space. The obtained function is the pair distribution function $D(r)$.

Tweak factor The sample tweak factor is designed to reflect the fact that a powder sample can never be fully packed in the container. So one will need a tweak factor to infer the local density. It is the reciprocal of the packing fraction

$$f_{\text{tweak}} = \frac{1}{f_{\text{packing}}} \tag{2.22}$$

$$f_{\text{tweak}} = \frac{\rho_{\text{local}}}{\rho_{\text{average}}} \tag{2.23}$$

where the tweak factor must be greater than 1. ρ_{local} is the local grain density, and ρ_{average} is the approximation of the actual packing density. The greater the

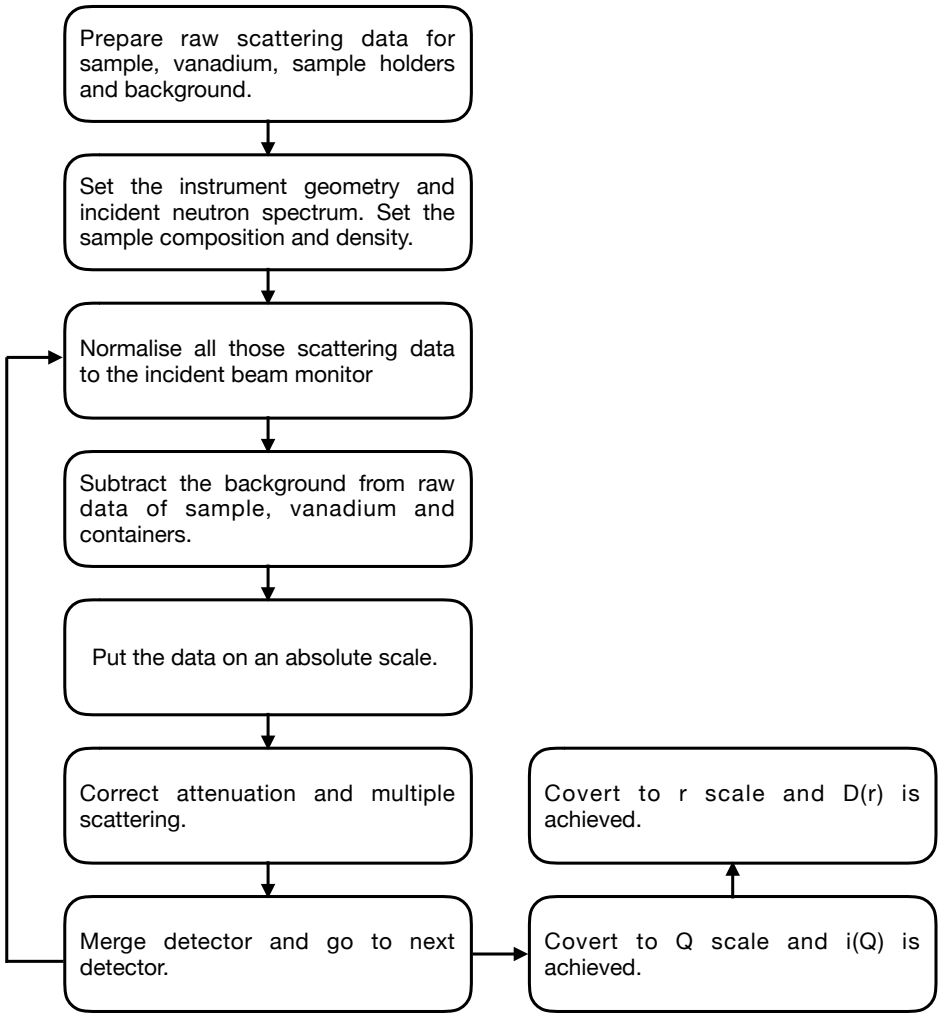

Figure 2.9: The workflow of GudrunN for total scattering data correction.

tweak factor is, the smaller the density is and thus, the first peak intensity is lower.

Inelasticity Light atoms such as H have a longstanding problem in neutron diffraction experiments, as they exchange large amounts of energy during the scattering process. The energy loss makes the scattered particle change momentum, where the 'static' structure factor can not be achieved as expected in the diffraction experiment [95]. The inelasticity process mainly affects the self scattering component. We are trying to get the static scattering factor, $S(Q)$ by integrating over all energies of $S(Q, \omega)$. Obviously this requires collection of

all the dynamic process to get an accurate $S(Q)$ and that is almost impossible. One solution is to use the Placzek correction. It is based on the assumption that the mass of the neutron is smaller than that of the scattering atom, and the neutron energy is smaller that that of the excitation energy of the atom [95]. The energy of the neutron is transferred to the scattering atom completely.

$$\hbar\omega = \frac{\hbar^2}{2M}(|\mathbf{q}_{\text{final}}|^2 - |\mathbf{q}_{\text{init}}|^2) \tag{2.24}$$

where $\mathbf{q}_{\text{final}}$ and $\mathbf{q}_{\text{init}}$ refer to the momenta after and before the scattering process [81]. Thus, a calculation using the ratio of the neutron and the scattering atom mass can be performed to approximately obtain the estimated differential cross section. In reality, the Placzek correction overestimates inelasticity and might subtract too much useful data as a result.

Top hat function Backgrounds need to be subtracted from the diffraction data, like self scattering from single atoms. The unremoved self scattering can not be distinguished from the useful interference scattering, and after transformation back to real space, some features are introduced to the low-r region of $D(r)$. The problem becomes more difficult with hydrogen atoms, as the desired interference scattering may only be 5% or less of the self scattering component [95]. This explains why samples with light atoms show distinct scattering functions for each detector bank. The idea is to convolve the data with a top hat function in reciprocal space, which would be then treated as the self scattering. The estimated self-scattering would be deducted from the diffraction data. The Gudrun manual gives a detailed explanation on how the top-hat correction works, and if we only focus on choosing the right value of top hat width, Q_T to perform the correction, the rule of thumb is,

$$Q_T > \frac{3}{r_{\text{min}}} \tag{2.25}$$

where r_{min} is the lowest r and before that, there are no physically plausible peaks in the $D(r)$ profile.

2.7 Reverse Monte Carlo (RMC) modelling

Total scattering experiments can produce PDFs to examine the short-range and long-range order. By analysing the PDF, atom-pair distances, coordination environment and other information are readily extracted. It is often useful to find whether an atomic model describing the experimental data is accessible.

The RMC method is developed based on the Monte-Carlo algorithm (MC). The idea is to start from randomness, and atom positions are allowed to change in a random manner to reduce the overall energy until χ^2 reaches the global minimum. Instead of choosing energy as the guiding parameter but the agreement between experimental and simulated data are parameterised with a χ^2 function. One advantage is the RMC method gives an unbiased model that is consistent with all the datasets.

The RMC method for studying disordered materials was introduced by McGreevy and Pusztai [96]. It is a structural modelling technique based on many sorts of experimental data, simultaneously if wished. A variety of data types, including powder and single-crystal neutron diffraction, X-ray diffraction and electron diffraction, extended X-ray absorption fine structure are applicable. When the RMC method was first published, limited datasets were used in the course of refinement because the target materials were liquids at that time, including total scattering function $i(Q)$ and pair distribution function $D(r)$. One might argue that these two functions are generated from a single total scattering experiment, but these two functions favour different space and thereby different aspects of the simulated system. $i(Q)$ is related to reciprocal space, while the PDF is defined in real-space. Bragg data have been added to the experimental datasets in RMC, which provides long-range order to crystalline materials [97]. Thus RMC can now be applied to many different systems like liquids, glasses, polymers, crystals and even magnetic materials

[98]. The version used in this thesis is RMCprofile [97], based on the original RMC code but with new features of separately utilising information contained in Bragg peaks and total scattering data.

The mechanism of RMC is easy to comprehend. A three-dimensional starting configuration of atoms is generated and followed by steps moves. RMC is a big box simulation method, and the simulation box is able to refine 10^4 atoms. Unit cell parameters are typically extracted from Rietveld refinements, and the initial configuration is built as a supercell of crystallographic unit cells. In each step, the difference between experimental and simulation is calculated and the goodness of the fit is quantitively judged by a defined agreement factor, χ^2

$$\chi^2 = \sum (y_{\text{obs}} - y_{\text{calc}})^2 / \sigma^2 \tag{2.26}$$

where we sum over all data points; y_{obs} and y_{calc} represent the observed and experimental quantities respectively, and σ^2 is a weighting factor which corresponds to the assumed experimental uncertainty on y_{obs}. The simulation follows a minimisation process, and keeps refining a starting model by moving an atom in the configuration randomly until it reaches better agreement with the data. Let us specify $\Delta\chi^2$ as the change of χ^2 for a single move. If $\Delta\chi^2 < 0$ the change is accepted. However, if not, the probability algorithm

$$P = \exp(-\Delta\chi^2/2) \tag{2.27}$$

is called to decide whether to accept the change, rather than reject it instantly. This ensures the model does not get trapped in a local minimum, and enables the model to converge.

The convergence is assessed by whether the value of χ^2 reaches the global minimum. The total χ^2 is the sum of each χ^2 calculated from every input dataset. It is given as

$$\chi^2_{\text{RMC}} = \chi^2_{\text{PDF}} + \chi^2_{i(Q)} + \chi^2_{\text{Bragg}} + \chi^2_{\text{constraints}} \tag{2.28}$$

$$\chi^2_{\mathrm{PDF}} = \sum_j \left[D_{\mathrm{calc}}\left(r_j\right) - D_{\mathrm{exp}}\left(r_j\right)\right]^2 / \sigma^2\left(r_j\right) \tag{2.29}$$

$$\chi^2_{i(Q)} = \sum_k \sum_j \left[i_{\mathrm{calc}}\left(Q_j\right)_k - i_{\mathrm{exp}}\left(Q_j\right)_k\right]^2 / \sigma^2_k\left(Q_j\right) \tag{2.30}$$

$$\chi^2_{\mathrm{Bragg}} = \sum_{h,k,l} \left[I_{\mathrm{calc}}\left(t\right) - I_{\mathrm{exp}}\left(t\right)\right]^2 / \sigma^2\left(t\right) \tag{2.31}$$

$$\chi^2_{\mathrm{f}} = \sum_l \left[f_l^{\mathrm{calc}} - f_l^{\mathrm{set}}\right]^2 / \sigma^2_l \tag{2.32}$$

The distance window, as the name implies, acts like a window to restrain atoms moving outside this set range. As RMC is driven by experimental datasets, there are no other constraints on the real system. Hence it might generate configurations where the coordination number of specific atoms becomes unphysical. The solution is to define a narrow distance window on the initial configuration, and use RMC to generate the correct topology of local atoms to ensure the model is physically reasonable.

For molecular systems, interatomic potential constraints are often used to avoid the molecules getting too close to each other. They are capable of defining the shape of the molecules. The weighting of the potentials is connected with the temperature used in RMC, by the underlying probability

$$P = \exp(-\Delta E/kT) \tag{2.33}$$

where T is the temperature and k is the Boltzmann constant.

2.8 Geometric Analysis of Structural Polyhedra (GASP) analysis

GASP is used to quantitively analyse the disordered atomistic models from RMC simulation [100]. GASP is a powerful tool designed to create an initial ideal polyhedra template from the configuration, then makes a direct comparison with the distorted counterpart. Basically, GASP treats each polyhedron

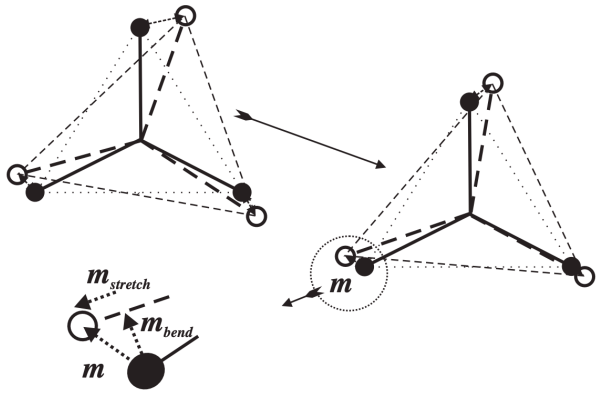

Figure 2.10: The mismatch factors are calculated through finding the best-fit rotation in GASP. The residue mismatch m are then separated into the bending and stretching terms as m_{bend} and m_{stretch}. Graph from Wells's paper [99].

as a rigid body, and as the name implies, calculates the geometric mismatch between structures and seeks the best described motions using minimisation of mismatches.

If we consider the structure bond by bond, then we could compare the differences between each bond vector from two configurations.

$$M = \sum_{q} {E_q}^2 \tag{2.34}$$

The M is called the mismatch score, and after summing over all bond vectors we get the total mismatch score. E_{q} refers to the mismatch factors, and q specifies how many bonds there are in each polyhedron. Take $q = 6$ for the PbI_6 octahedron. The sum of the squared distances between corresponding atoms in the two structures, referred to as the "mismatch", is decomposed into components due to rotation of the polyhedron as a rigid unit, bond stretching, and bond bending, as shown in figure 2.10. Then GASP searches for the minimum starting from a zero rotation until finding the best fit in rotation. The output then gives detailed distorted structural information, such as individual bond lengths and bond angles.

Chapter 3

Local structure of inorganic perovskite $CsPbI_3$

3.1 Introduction

Significant attention has been paid to hybrid organic-inorganic lead halide perovskites in photovoltaic applications due to their high efficiency, low cost and easy fabrication. However, problems with long-term chemical stability and durability remain to be solved. This instability has been demonstrated to be associated with the organic component, a promising alternative is then provided by the closely related inorganic perovskites [101]. One such material is $CsPbI_3$. Its band gap of E_g = 1.73 eV is suitable for photovoltaic applications, especially when the material is prepared in the form of quantum dots [18]. To manufacture higher-efficiency photovoltaic devices commercially, we need to better understand the structural properties behind the performance of these materials.

$CsPbI_3$ has two crystallographic phases at ambient pressure: the high-temperature cubic α phase with the ideal perovskite structure of cubic symmetry, space group $Pm\bar{3}m$ (figure 3.1a), and the low-temperature orthorhombic

δ phase of space group *Pnma* (figure 3.1b). The two phases do not have a group-subgroup relationship: the cubic perovskite phase consists of corner-sharing PbI_6 octahedra, but the orthorhombic phase contains edge-sharing PbI_6 octahedra. Moreover, the coordination number of Cs to I changes from 12 to 9 between the α and δ phases. The two phases transform to each other by a reversible first-order transformation with a wide co-existence temperature range around 40 K (560–600 K) [102]. Undercooling the α phase below this transition results in the formation of metastable β (tetragonal, space group $P4/mbm$) and γ (orthorhombic, space group *Pbnm*) perovskite phases, both of which transform back to the thermodynamically-favoured δ phase over time [103]. A recent DFT study has confirmed that, although the 'black' orthorhombic γ phase is more stable than the cubic α phase, the 'yellow' non-perovskite δ phase is still the most stable one [104].

The first crystallographic study of the phase transition in $CsPbI_3$, performed using Rietveld refinement of synchrotron x-ray diffraction data, reported anisotropic thermal motion of the iodine atoms, with significant motion transverse to the linear Pb–I–Pb linkages, in common with many other perovskites [102]; these results are consistent with neutron diffraction work on related materials such as $CsPbCl_3$ [105, 106]. However, these latter authors point out, conventional diffraction methods cannot in principle distinguish whether (1) this is due to the growth of small clusters of lower symmetry than the parent cubic phase, as precursors of a phase transition, or (2) this reflects bond anharmonicity, in the sense that the distribution of atomic positions is not well described by a Gaussian function.

One way of tackling this problem is by probing the atomic *dynamics* directly. Experimentally, this can for instance be done using inelastic neutron scattering measurements. In the closely related material $CsPbCl_3$, these confirm that the transverse acoustic modes remain below about 2 meV throughout the

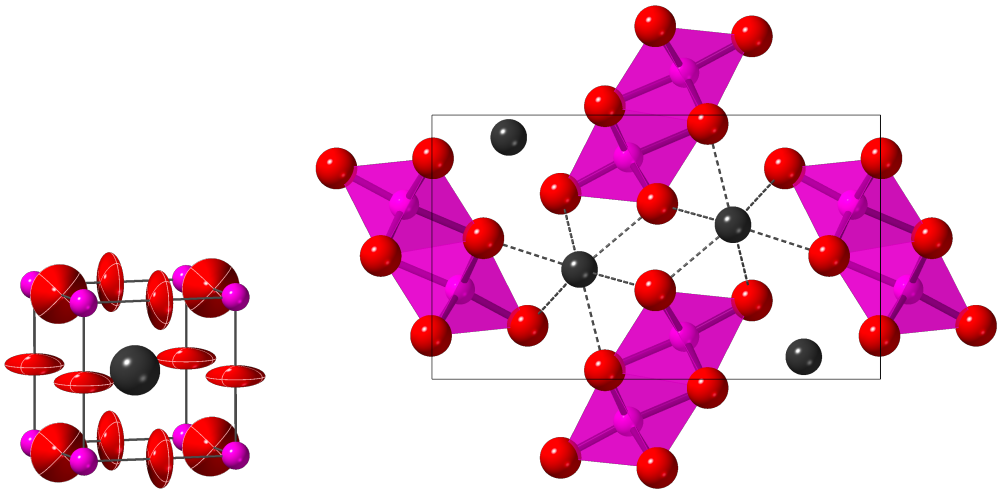

(a) (b)

Figure 3.1: Refined crystal structure models of (a) cubic α phase at 673 K in three-dimensional perspective, and (b) the orthorhombic δ phase at 293 K viewed down the [010] axis with the [001] axis in the horizontal direction. Cs atoms are grey, Pb atoms are pink. and I atoms are red. In (a) the atoms are represented by ellipsoids to represent their thermal motion, highlighting the large transverse motions of the I atoms. In (b) the PbI_6 coordination is represent by translucent shaded octahedra. The amplitude of thermal motion is smaller than observed in the cubic phase, and were not shown for this purpose. The 9 nearest Cs–I neighbours are connected using dashed lines. Both (a) and (b) are drawn to the same scale.

Brillouin zone, with low-frequency optic modes too at some special positions [107]. Computationally, one approach is to model the energy profile associated with normal modes. Density-functional perturbation theory calculations have revealed double-well potentials at both the Brillouin zone centre [108] and zone boundary [109].

Here, neutron total scattering data were collected, and combined with RMC simulation to generate the the "snapshot" configurations. These configurations involve the superposition of many different distortion modes, with varying amplitudes, and thus complement rather than being directly comparable to inelastic or computational results concerning a single mode. Nonetheless, some particular features in the local structure can be associated with zone-centre or

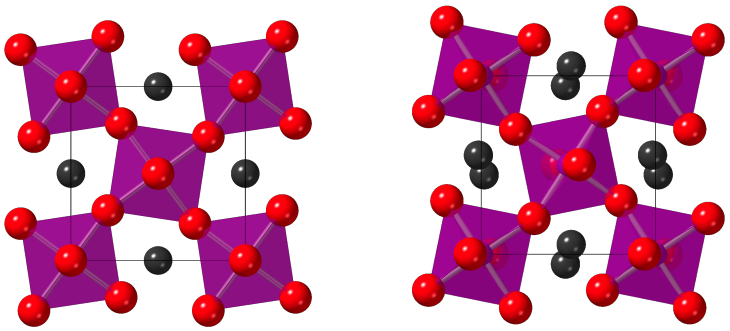

(a) (b)

Figure 3.2: Crystal structures of (a) tetragonal β phase of $CsPbI_3$ at 510 K and (b) orthorhombic γ phase at 325 K viewed down [001] axis. The structures are taken from Marronnier [103].

zone-boundary modes.

3.2 Experimental

3.2.1 Neutron total scattering experiment

Neutron scattering measurements were performed using the GEM diffractometer at ISIS, as introduced in section 2.4. The powder sample (3.352 g) was packed in a cylindrical vanadium can of 8 mm diameter (inner-diameter). Apart from measuring the sample in the can, sample background along with the vanadium rod data for normalisation were also collected. The V-5.14%Nb rod was specially made to give the scattering length as 0 with no sharp Bragg peaks to better normalise the data. Data were collected when heating the sample from room temperature to 673 K, and then cooling to 473 K. Collection at the same temperatures in both heating and cooling processes was carried out in order to check the existence of any hysteresis through phase transitions. Both long and short run time measurements were obtained for different reasons. Data from total scattering were obtained from long-run time measurements at temperatures of 293, 573, 613, 643 and 673 K. Shorter measurements for crystal

structure refinement were performed for temperatures from room temperature to 673 K in steps of 10 K.

3.3 Data processing

3.3.1 Rietveld refinement

The raw data were transformed into diffraction patterns using the Mantid software [110]. Rietveld refinement was performed using the EXPGUI interface to GSAS [76, 111]. For temperatures in the range 583–603 K the data showed diffraction from α and δ phases, and a two-phase refinement was carried out successfully. Above this temperature range the data were for the cubic α phase, and in this case the crystal structure refinement required variation of the unit cell parameter, isotropic atomic displacement parameters for the Cs and Pb ions, and 2 anisotropic atomic displacement parameters for the I anions. The iodine atoms oscillate about the Pb–I–Pb chain due to thermal motions, so displacements along the chain should be smaller than in the other two transverse directions. In the lower-temperature data where the crystal structure of the orthorhombic phase was refined, x and z atomic coordinates also need to be adjusted for all atoms. Because y atomic coordinates are on special positions due to symmetry, they were left unrefined. In this case only isotropic atomic displacement parameters were refined. Some hysteresis was observed in the phase transition between heating and cooling runs. For example, 573 K data show both phases on heating, but remains cubic in contrast during cooling process.

A representative Rietveld fit of both two phases is given in figure 3.3.

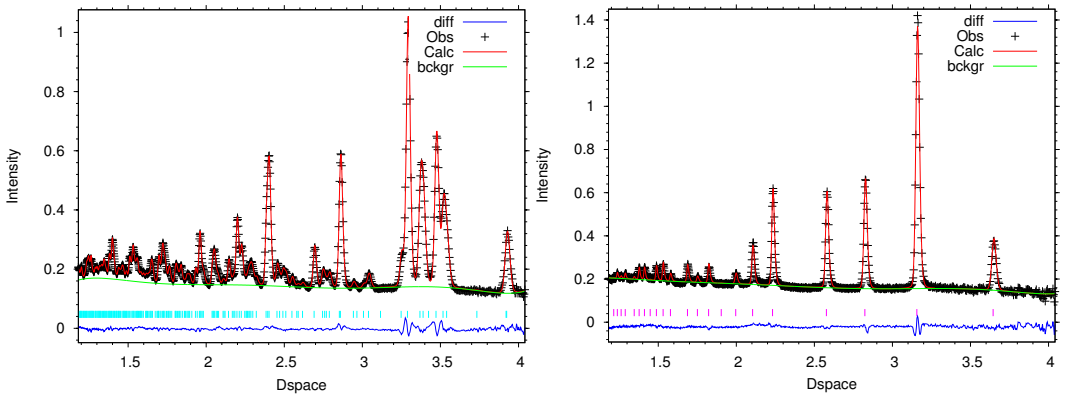

Figure 3.3: (a): Rietveld refinement for diffraction data collected at room temperature 293 K. The lattice parameters for the orthorhombic δ phase, space group $Pnma$, and a = 10.4670(2) Å, b = 4.8052(1) Åand c = 17.7908(3) Å. (b): Rietveld refinement for diffracted data collected at high temperature 673 K. The phase for refinement is cubic α phase, space group $Pm\bar{3}m$, and $a = b = c$ = 6.3130(1) Å. Bank 4 and 5 data were used in Rietveld refinement.

3.3.2 Total scattering data correction

The range of Q was chosen to be between 0.5–30 $Å^{-1}$ for merging the differential cross section data from all 8 detector banks, and the Q range for banks 3-8 were used with Q ranges up to 60 $Å^{-1}$. In principle, Q_{max} should be as high as possible to avoid the termination ripples. But in practice, the signal-to-noise ratio would be relatively low at higher Q region as in figure 3.4. The first two banks are placed at low angles, and as a result they might include background from the incident collimator. It would introduce problems when merging with other banks, and so these low angle data were excluded to avoid problems. Effective ranges of data used in Gudrun have been plotted from .dcs01 file in figure 3.4.

The 673 K data were taken as an example. The first thing is to get the correct sample composition and dimension information, as they are used in the theoretical calculation. For $CsPbI_3$, the sample composition is shown in table 3.1. The inner and outer radii of the packed sample inside the vanadium

Atom	Isotope	Composition
Cs	0	1.0
Pb	0	1.0
I	0	3.0

Table 3.1: The sample atomic composition used in pair distribution function analysis.

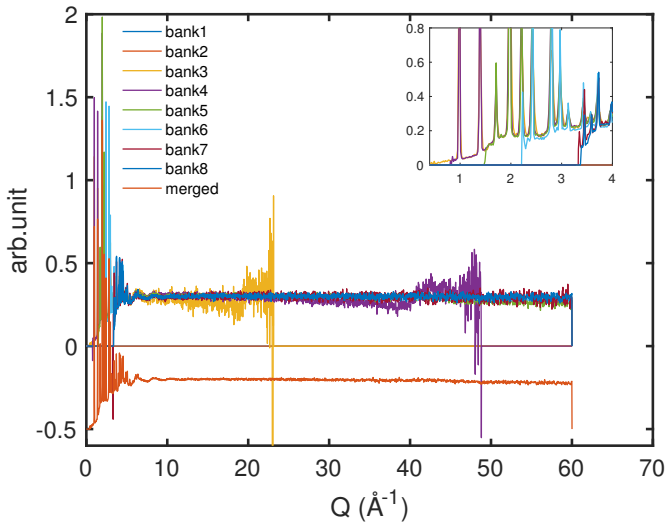

Figure 3.4: Differential cross section data measured from each bank were plotted against Q. The merged data were added an offset for easy comparison. The noise in bank 3 and bank 4 data becomes more obvious with increasing Q. The inset indicates data in the low Q region were consistent between different banks, because the sample contains no light atoms.

can is 0.0 and 0.415 cm, and the sample height is 5.0 cm.

The sample tweak factor was calculated to be around 3.3. In $CsPbI_3$, there is no physically plausible feature below 2.5 Å and the minimum radius for Fourier transform was set to be this number. In order to remove the background, the top hat width Q_T was specified as -17 $Å^{-1}$. The negative value does not perform a top hat function but an average value of the scattering function from Q_T to Q_{max} is subtracted from the data. The lorch function was applied to smooth the PDF data, and β and r_0 were set to be 0.05 and 0.02 here, respectively.

The goodness of the PDF data is difficult to judge, and GudrunN compares

the high-Q DCS level after merging with the calculated value, $\sum_i c_i \bar{b}^2/4\pi$. All the temperature data were processed using the same set of values in the Gudrun correction, except sample density extracted from Rietveld refinement.

3.4 RMC modelling

In the present study, the initial three-dimensional atomic configurations for each temperature were created from the crystal structure generated by the Rietveld method in each case using `data2config`, part of the RMCprofile software suite. For the cubic phase the configurations correspond to an $8 \times 8 \times 8$ supercell of the unit cell (2560 atoms), and for the orthorhombic phase the configuration was a $5 \times 10 \times 3$ supercell (3000 atoms). The RMC simulations were performed using the overall pair distribution function $D(r)$, the scattering function $i(Q)$ and the Bragg scattering profile as the sets of experimental data. We used distance windows to prevent any fragmentation of the atomic configurations. The distance window is to constrain atoms by defining the distance limits that atoms could move from their nearest neighbours as determined from the original configuration. This ensures the final configurations are physically reasonable models. Detailed values are shown in table 3.2. Here, the goodness-of-fit is judged by the calculated χ^2; If χ^2 no longer changes when generating more moves to the configuration, it is accepted as fully converged. Approximately 3.4×10^6 moves (1300 moves per atom) have been accepted to reach convergence in this case. A refined configuration at high temperature 673 K is shown in figure 3.5.

T (K)	Cs-Pb (Å)	Cs-I (Å)	Pb-I	I-I (Å)
673	4.17-6.78	3.06-5.88	2.70-4.05	3.22-5.66
643	4.17-6.78	3.06-5.88	2.70-4.05	3.22-5.66
613	4.17-6.78	3.06-5.88	2.70-4.05	3.22-5.66
573	4.19-6.78	3.09-5.88	2.70-4.05	3.25-5.63

Table 3.2: Distance-window constraints for different atom pairs used in RMC refinement.

3.5 Analysis

3.5.1 Crystal structure analysis

The results for Rietveld refinements (lattice parameters, atomic fractional coordinates, and atomic displacement parameters) for both α and δ phases are given in appendix A.1.

The lattice parameters are shown as a function of temperature in scaled form (to allow for comparison of temperature dependence) in figure 3.6. The three orthorhombic lattice parameters show similar thermal expansivity, with an average coefficient of linear thermal expansivity of 21 ± 1 MK^{-1}. The cubic phase shows positive thermal expansion with linear expansivity 52 ± 1 MK^{-1}, which is surprisingly around 2.5 times larger than for the orthorhombic phase, but there is no explanation for it yet.

The average structure of the α phase calculated from the RMC configurations agreed well with Rietveld refinement both in atomic positions and, more significantly, in the atomic displacement parameters. All atoms are on special positions with coordinates set by symmetry, and the average positions are consistent with the special positions to within 0.001 in terms of fractional coordinates. The ADPs calculated from the RMC configurations are given in appendix B.1. The ADPs from the RMC analysis were consistently slightly larger than from Rietveld refinement, which is attributed to the effects of attenuation of the neutron beam by the sample. It was noted that the ADPs

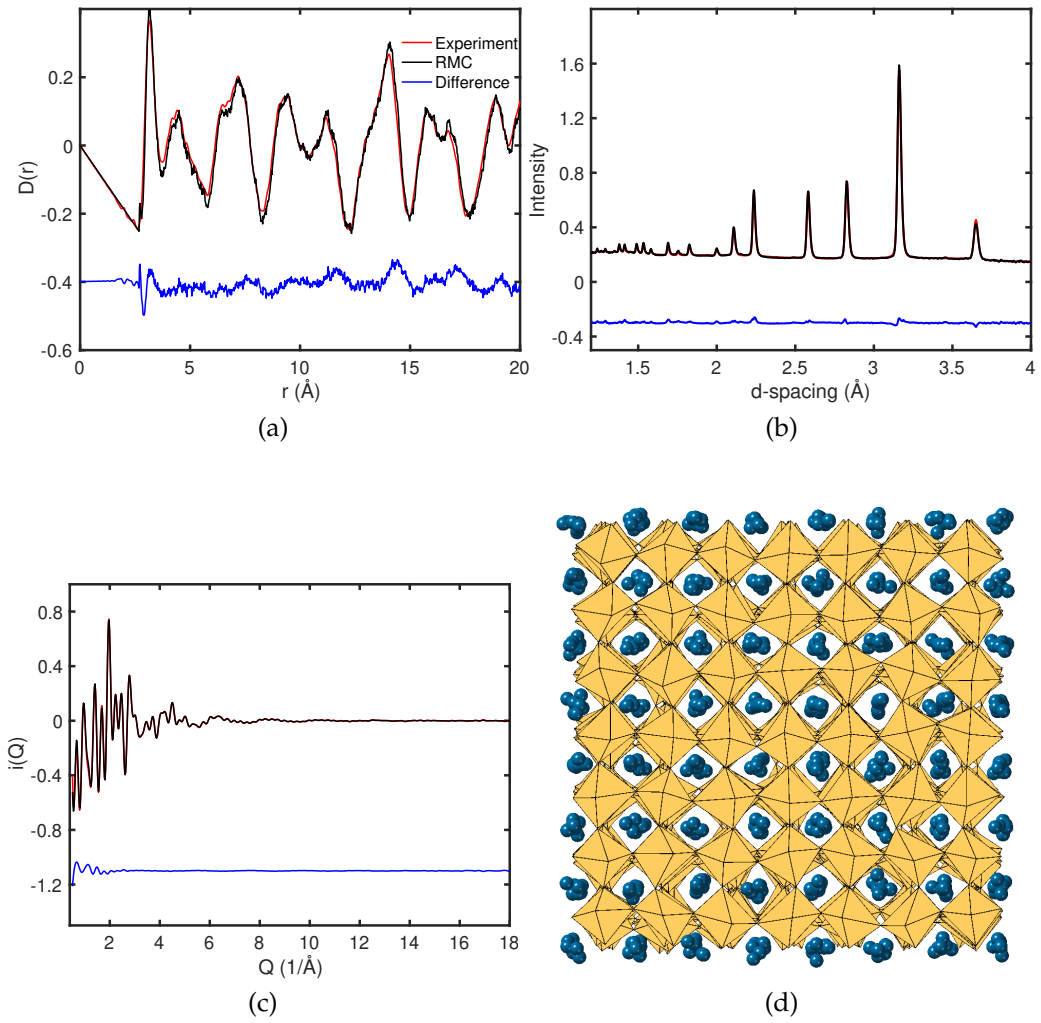

Figure 3.5: Representative fitted data for both phases of $CsPbI_3$, showing PDF $D(r)$ (a), Bragg scattering profile (b), scattering function $i(Q)$ (c). The end-RMC configuration at 673 K, view from [001] direction. The PbI_6 polyhedra are distorted and the A-site Cs atoms indicate large off-site displacements.

for the iodine atom show much larger displacements in the two directions perpendicular to the Pb–I–Pb linear linkage than in the direction along the linkage, with the transverse mean-squared displacements being around 6 times larger than for the longitudinal mean-squared displacements. Actually, an even larger difference between the transverse and longitudinal mean-square displacements was obtained in the previous crystal structure analysis of reference [102], the difference is probably because both the longitudinal and transverse

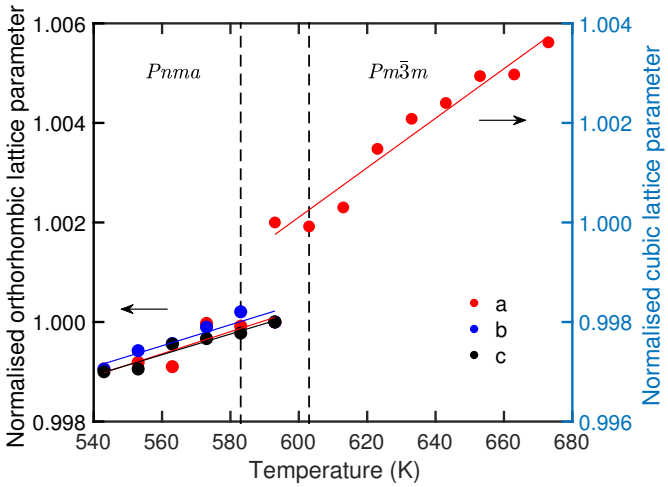

Figure 3.6: Variation of the lattice parameters of $CsPbI_3$ with temperature, obtained by Rietveld analysis. For convenience, lattice parameters were scaled by their values a_0, b_0, c_0 at 593 K. The three lattice parameters of the orthorhombic phase show almost the same thermal expansion. Because of the large change in volume at the phase transition (7% per formula unit), the orthorhombic and cubic phases are indicated on separate vertical axes; thus the change in volume cannot be read directly from this figure By contrast, the axes for the orthorhombic (left) and cubic (right) values cover the same difference in relative lattice parameter, so that the thermal expansion of the two phases is directly comparable. Statistical errors of the values of the lattice parameters are smaller than the size of the markers.

mean-squared displacements are underestimated by a constant amount in that study, due to the effects of beam absorption. The ADPs of Cs and Pb are isotropic by symmetry in the Rietveld refinement, with the value for Cs being about twice as large as for Pb. This is consistent with the displacement parameters calculated from RMC, shown in appendix B.1.

3.5.2 Local structure analysis

The experimental pair distribution functions $D(r)$ are shown in figure 3.7. The first peak corresponds to the Pb–I nearest neighbour distance at around 3.2 Å, and the position and integrated area are constant for all temperatures in both phases. It should be noted that the tail of the lowest-r PDF peaks overlap

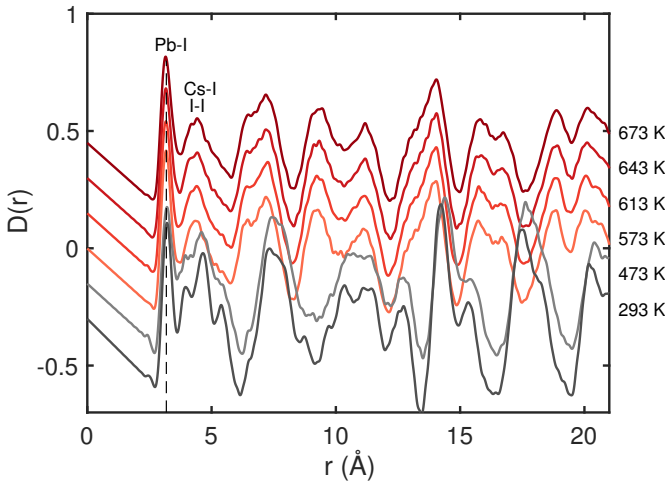

Figure 3.7: The pair distribution functions $D(r)$ for $CsPbI_3$ for all temperatures where there is a single phase. A constant offset has been applied to separate the separate $D(r)$ curves. The δ phase data are shown in grey and the α phase data in red.

with the next highest feature. The PDFs across the range of distances show little obvious variation with temperature in the cubic phase. The PDFs for the two temperatures in the orthorhombic phase are clearly very different from the PDFs of the cubic phase other than for the first (Pb–I) peak, reflecting the significant differences in crystal structure. For example, the second peak for the cubic phase is a direct overlap of the I–I and Cs–I distances, which have different mean distances in the orthorhombic phase. The PDF for the orthorhombic phase shows more variation between the two temperatures (temperature interval of 180 K) than across the span of temperatures of the cubic phase (100 K), particularly in the distance range 3.5–6 Å where the broadening of the peaks on heating was observed.

The distributions of nearest-neighbour distances from the RMC configurations are shown in figure 3.8. The interesting point about these diagrams is that the distribution functions are remarkably asymmetric in each case. For example, the Pb–I distribution has an especially long tail to higher distances, indicating substantial bond anharmonicity. The mean Pb–I distance at 573 K is

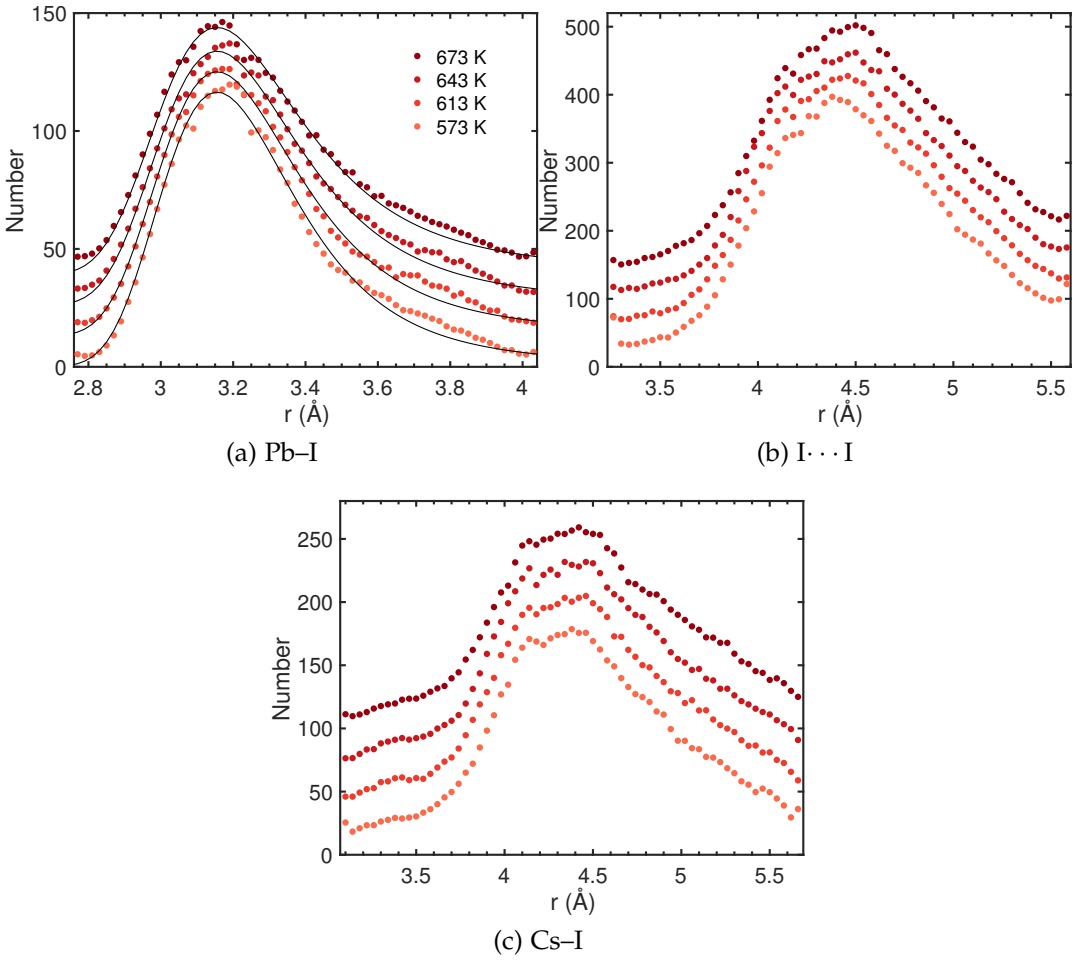

Figure 3.8: RMC distributions of nearest neighbour distances: (a) Pb–I; (b) I· · · I; (c) Cs–I. An offset has been added to separate the curves at different temperatures. The continuous curves are the result of fitting to an anharmonic potential energy function as discussed in section 3.5.4.

3.27 Å, and a standard deviation of the distribution of σ = 0.25 Å. The mean distance is around 4% larger than the distance between mean positions (equal to half the lattice parameter, 3.144 Å at 573 K), which is quite common in polyhedral framework material. The value of σ is consistent with the values of the ADPs; for example, the root-mean-squared displacement of the Pb atom is equal to 0.22 Å from the ADP data. The asymmetry of the I–I and Cs–I distances, which both have mean values around $a/\sqrt{2}$, similarly show a broad asymmetric distribution, reflecting the Pb–I motions.

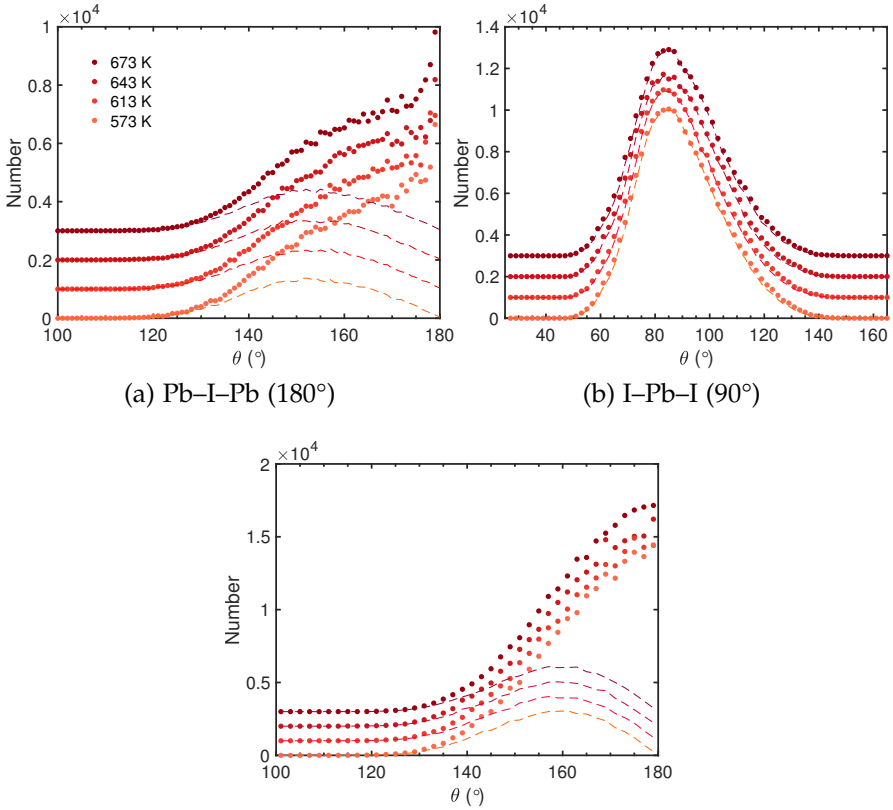

(a) Pb–I–Pb (180°)

(b) I–Pb–I (90°)

(c) I–Pb–I (180°)

Figure 3.9: RMC distributions of bond angles θ: (a) Pb–I–Pb (180°); (b) I–Pb–I (90°); (c) I–Pb–I (180°). The pure angle distributions are shown as dashed lines, while the normalised distribution functions by dividing by $\sin\theta$ are plotted with dots. An offset has been added to separate the curves at different temperatures.

It is interesting to compare the results here with previous RMC studies of $SrTiO_3$ [112] and $SrSnO_3$ [113]. In both these cases the distributions of octahedral bond lengths (Ti–O and Sn–O) have much shorter mean values, but also the distributions are narrower and symmetric. Thus the broad, asymmetric distribution of the octahedral bond lengths in $CsPbI_3$ cannot be attributed to the perovskite geometry alone.

The distribution functions for the linear Pb–I–Pb bond angles, and for perpendicular and linear and I–Pb–I bond, are shown in figure 3.9. The raw angle distributions $f(\theta)$ was plotted, where θ is the bond angle, together with

the scaled function $f(\theta)/\sin\theta$ to account for the diminishing size of the the solid angle $\mathrm{d}\Omega = \sin\theta \mathrm{d}\theta \mathrm{d}\phi$. The mean angles with standard deviations are $152 \pm 12°$, $89 \pm 15°$, and $157 \pm 11°$ respectively.

3.5.3 Rigidity analysis

An alternative to analysing bond angles is to consider the motion of the PbI_6 coordination octahedra as a whole. To analyse the refined RMC configurations in these terms, the Geometric Analysis of Structural Polyhedra (GASP) code [99, 100, 114] was used, as discussed in section 2.8. Roughly speaking, in the perovskite structure the rotational component corresponds to the low-energy zone-boundary octahedra rotation phonons, while the bond-bending and bond-stretching components correspond to higher-frequency phonons across the Brillouin zone.

Of these three components, it is found that bond bending contributed the most to the observed distortion, accounting for 0.52 ± 0.04 of the total mismatch. Rigid-body rotation contributed 0.30 ± 0.04, while bond stretching, expected to be more energetically expensive than bond bending, makes up the remaining 0.18 ± 0.02. Expressed in this way as a percentage of the total mismatch, the values of these three components show negligible temperature dependence between 573 K and 673 K as in figure 3.10, as would be expected.

Figure 3.11 shows, the distribution of PbI_6 orientations as determined by the GASP analysis. The mean deviation angle from the average structure at 673 K, with standard deviation, is $8.4 \pm 3.5°$. For comparison, consider the analogous angles in other perovskite materials. In $SrTiO_3$, which undergoes a displacive phase transition, the TiO_6 octahedra tilt only around 2° in the low temperature phase [112]. On the other hand, in ScF_3, an extremely flexible octahedral framework in which the perovskite A site is vacant, the RMC-

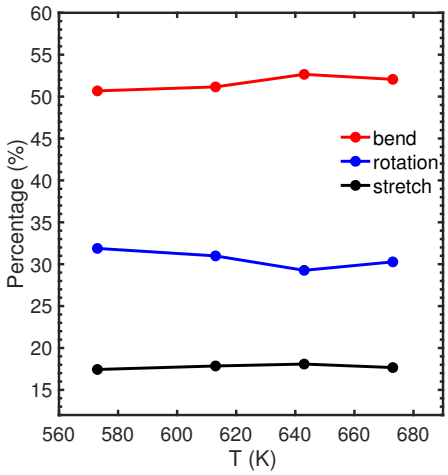

Figure 3.10: GASP analysis breaks the total motion into three kinds of motions, I–Pb–I bonds bending (red), whole-body rotations of the PbI_6 octahedra (black), and Pb–I bond stretching (blue). These components respectively account for 52%, 31% and 17% of the total motion.

derived octahedral tilting angle is around 10° in the high temperature phase [115]. This suggests that ScF_3 is extremely flexible in terms of the polyhedral network, and $SrTiO_3$ is relatively rigid while $CsPbI_3$ is between those two. Unlike the other two perovskite materials, there is no A-site cation in ScF_3, so the ScF_6 cage is quite empty, which allows the flexibility and the deformation of the ScF_6 octahedra.

3.5.4 Bond anharmonicity

As shown in figure 3.8, the Pb–I bond distribution has an asymmetric shape, a sign of significant anharmonicity. The Morse potential is one model of interatomic potential for diatomic systems. It differs from the harmonic oscillator model by adding an extra perturbation term to the harmonic models because it is not always the case that the potential is harmonic that all transitions occur at the same frequency. Also, the harmonic model does not allow bond breaking as the Morse model does, which becomes a better approximation of the interatomic potential for real bonds. Here in this case, the distance

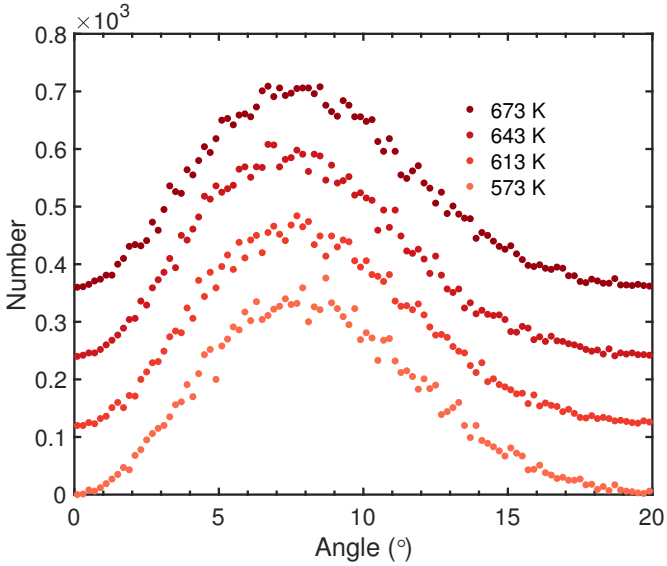

Figure 3.11: The distribution functions for PbI_6 rotations calculated in the GASP analysis. Offsets were added to top three temperature data for comparison.

distribution of Pb–I bonds shows an asymmetric shape and an anharmonic potential should be used to describe the bond potential. The Morse potential was used as it is simple and proper for the purpose.

The distribution data were fitted to the Boltzmann form $P(r) \propto \exp(-\phi(r)/k_B T)$, where $\phi(r)$ is the Morse potential:

$$\phi(r) = \frac{k}{2\alpha^2}\Big(\exp\left(-2\alpha(r-r_0)\right) - 2\exp\left(-\alpha(r-r_0)\right)\Big) \tag{3.1}$$

The three parameters are r_0, the equilibrium bond length; k, the harmonic spring constant at equilibrium; and α, a measure of the anharmonicity such that the nominal bond dissociation energy is $D = k/2\alpha^2$. Data for all four temperatures were fitted together, and reasonable fits to the Pb–I distribution functions between about 2.7 Å and 4.1 Å were obtained; above this distance, a slightly greater number of Pb–I pairs are observed than predicted by the Morse potential. The best-fit parameter values are $\alpha = 1.68 \pm 0.04$ Å^{-1}, $r_0 = 3.1559 \pm 0.0007$ Å, and $k = 1.477 \pm 0.003$ eVÅ^{-2}. The value of r_0 is very close to half of the value the cubic lattice parameter values given in A.1 as expected. The calculated distribution functions are shown in figure 3.8 for comparison

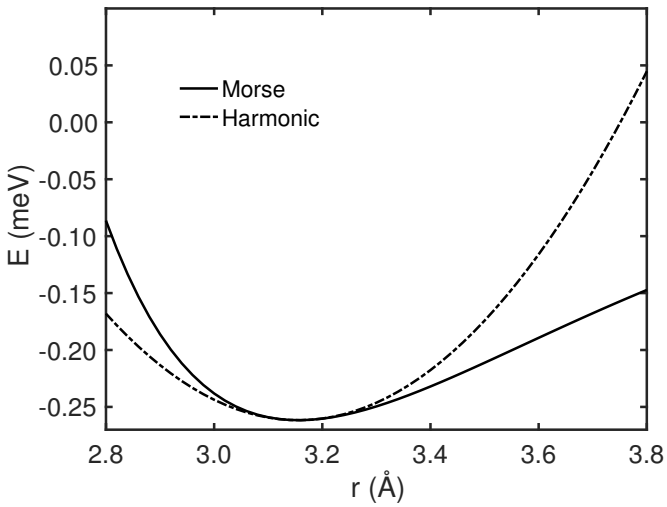

Figure 3.12: The variation of the Morse potential with distance using the potential parameters given in the text (solid line). This is compared with the corresponding harmonic function (dash-dot line).

with the RMC data. The agreement is very good, with the only discrepancy being at larger r which is in the tail of the Morse function.

Modelling the Pb–I bond as two atoms joined by a harmonic spring, the vibrational angular frequency is $\omega = \sqrt{k/\mu}$, where $\mu = 78.7\,\mathrm{g\,mol^{-1}}$ is the reduced mass. Substituting in the fitted value of k, we obtain an angular frequency of $\omega = 13.2\,\mathrm{THz}$. The frequency of the longitudinal optic mode at the gamma point is, to first approximation, $\sqrt{2}$ times this value [116], namely 18.6 THz; this is comparable, for instance, with literature first-principles calculations that give a value of approximately 17 THz [109]. The nominal Pb–I bond dissociation energy calculated from the fitted parameters gives $D = 262\,\mathrm{meV}$.

Given that the fitted values of the Morse potential appear to be plausible, we now consider the implication of the shape of this curve. The function with fitted values is plotted in figure 3.12, and compared with the harmonic value calculated from the value of k. It is clear that over the range of values of distance there is a significant difference that will contribute to the asymmetry of the bond distribution function. At $r = 2.8$ Å the Morse potential is 1.9 times larger than the harmonic energy relative to the minimum energy, and at $r = 3.8$

Å the Morse potential is lower than the harmonic value by a factor 2.7. These differences represent the intrinsic anharmonicity of the Pb–I bond, and provide the explanation for the marked asymmetry of the bond distribution function.

3.6 Summary

In summary, I have performed total neutron scattering measurements, combined with RMC modelling, on the optoelectronically active inorganic perovskite $CsPbI_3$. An atomistic model of the cubic α phase is in agreement with previous measurements, that there is substantial transverse motion of the I ions. The Pb–I bond is strongly anharmonic, and the distribution of bond distances as a function of temperature is well fitted by a Morse potential with reasonable equilibrium bond length and vibrational frequency.

Anharmonicity is a vital consideration for practical use of these materials, since it will substantially affect the structure at useful operating temperatures for photovoltaic devices. This insight into the behaviour of the cubic PbI_6 framework is not only relevant to the inorganic perovskites; it also provides a starting point to understand their hybrid analogues, as both materials have a PbI_6 inorganic-framework. Although in the case of hybrid systems the lattice vibrations will be coupled to orientational disorder of the organic cations [36].

Chapter 4

Local structures of the hybrid perovskite $CD_3ND_3PbI_3$

4.1 Introduction

Despite rapid developments in metal-halide perovskites solar cells, there are still problems with long-term stability and functional performance. Researchers have been seeking analogues of perovskite materials as a replacement, but none of them exhibit the high-efficiency of $CH_3NH_3PbI_3$ ($MAPbI_3$), as introduced in section 1.1.3. Thus, many unsolved problems of $MAPbI_3$, such as degradation and current-voltage hysteresis, should be addressed to understand and optimise high-efficiency photovoltaic devices for broad application.

The hybrid organic-inorganic perovskite, $MAPbI_3$ adopts a body-centred tetragonal structure with the $CH_3NH_3^+$ (MA) ion inside the PbI_6 cage at room temperature, and the MA ion is orientationally disordered. On heating, it transforms to the cubic structure at 327 K and remains stable until melting, with the molecule exhibiting orientational disorder. On cooling, the room-temperature tetragonal phase becomes the low-symmetry orthorhombic phase at 165 K, and the molecular ion is fully-ordered.

Phase transitions in perovskites with the ABX_3 structure have been extensively explored. Because of the corner-linked octahedral network, rotation of any individual octahedron causes the neighbouring octahedra to rotate as well [117]. Glazer characterises the octahedral tilting phase transitions, based on the octahedral rotations about three symmetry axes [117, 118]. The parent cubic phase is characterised as $a^0a^0a^0$, where the three letters denote zero tilting amplitudes along three crystallographic axes [100], [010] and [001]. As follows, it is convenient to define the Glazer notation of tetragonal and orthorhombic phase as $a^0a^0c^-$ and $a^-b^+a^-$. The $+$ and $-$ signs indicate the octahedra are tilted along the tilt axis in-phase or out-of-phase. The second a in $a^0a^0c^-$ means the equal amplitude and c indicates different rotation amplitude from the former two. In the tetragonal phase, the out-of-phase tilting along the [001] axis (c axis) causes the doubling of the unit cell. The tetragonal phase in $MAPbI_3$ is similar to $SrTiO_3$ with octahedra rotated about the z axis and in opposite senses in neighbouring layers, which explains the doubling of the unit cell along b axes In the orthorhombic phase, the symmetry is lowered through in-phase rotation along [010] and out-of-phase rotations along [101] axes.

Weller's group identified crystal structures of hydrogenous $MAPbI_3$ using neutron diffraction, which is better placed than X-ray diffraction to differentiate the methylammonium C and N atoms. Three phases of $MAPbI_3$ have been reported as ordered orthorhombic phase $Pnma$, partially disordered tetragonal phase $I4/mcm$ and highly disordered cubic phase $Pm\bar{3}m$. There have been diverging opinions over the structure of the ambient-temperature phase, but Weller's neutron diffraction data confirmed the space group as $I4/mcm$ [60]. The refined crystal structures are displayed in figure 4.1. The tetragonal phase with space group $I4/mcm$ is a subgroup of the cubic phase $Pm\bar{3}m$, and the orthorhombic phase with space group $Pnma$ could be seen as a distortion of

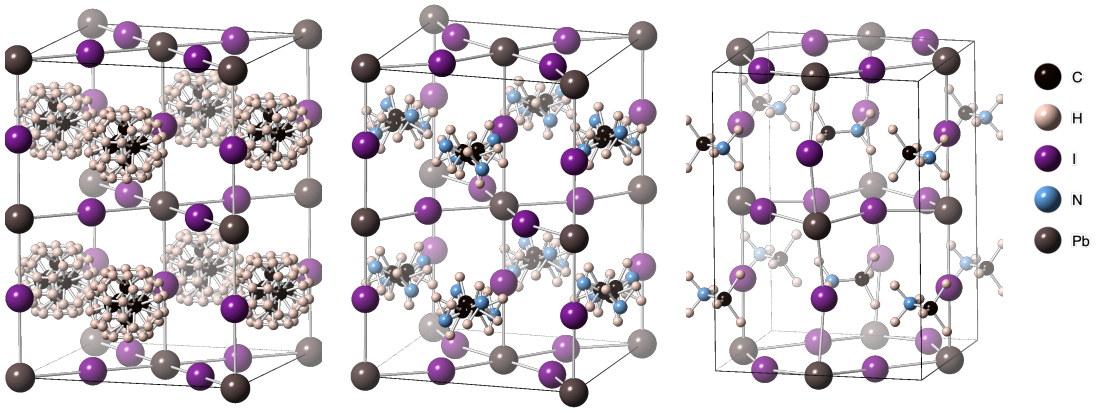

(a) $Pm\bar{3}m$ (b) $I4/mcm$ (c) $Pnma$

Figure 4.1: Schematic representation of (a) cubic $Pm\bar{3}m$ phase, (b) tetragonal $I4/mcm$ and (c) orthorhombic $Pnma$ phase by a $\sqrt{2} \times \sqrt{2} \times 2$ supercell of the cubic aristotype. The structures are adapted from Weller [60].

the cubic phase due to the group-subgroup relationship.

From diffraction data, it is frequently impossible to determine the distribution of molecular orientations. In some cases, where there the molecule has a limited number of distinct orientations, the atomic positions might be explicitly defined with partial occupancy, and the structure can be refined. One example is the molecular crystal adamantine, where each molecule has two possible orientations [58]. On the other hand, if the distribution of the molecular orientations is more complicated, with some degree of continuous orientational disorder, the atomic structure is not properly described as a series of atomic coordinates. In practice, it is conventional to try to reproduce the continuous distribution in terms of a set of atomic sites and large atomic displacement parameters, but in such a case the atomic sites may well have very little actual significance.

Here, total scattering is more useful than diffraction for giving the atom pair distances directly. Whitfield reported the local structures of fully deuterated $MAPbI_3$ using a combination of neutron and synchrotron total scattering [119].

Below 3 Å the PDF data represent the intramolecular atom pair distances and remain virtually unchanged. Minimal changes in the local structure were observed across the cubic-to-tetragonal phase transition, but peak shifting occurred from the tetragonal-to-orthorhombic phase transition. However, quantitive interpretation of the total scattering patterns is required to aid analysing orientationally disordered solids. Utilizing the 'real space Rietveld' method in PDFGui program [120], the author fitted the PDF data but could not fit the data within 3 Å where the full structural information of the MA molecules is wrapped. Given that the orientational dynamics of MA cations is still vague, elaborate analysis on MA orientation should be carried out to model the comprehensive data.

Previous NMR investigations have suggested that MA ions reorient as almost freely rotating molecules in the cubic phase on the picosecond timescale [49]. The dynamics of MA cations seem to be continuous in the cubic-tetragonal phase transition, but vary discontinuously across the tetragonal–orthorhombic phase transition . Considering the orientational disorder of $MAPbI_3$, currently, there are two views [121]. One is the molecules are almost freely rotating [122], while some think the orientations of the molecules are fixed [61]. Leguy proposed three rotational modes of the MA cation, but without further evidence of elastic incoherent scattering factor, they failed to distinguish between these three modes. Chen using quasielastic neutron scattering (QENS), interpreted that the C-N axes of MA ions exhibit four-fold and three-fold rotational symmetry in cubic and tetragonal phases, and only three-fold symmetry remains in the low-temperature orthorhombic phase. This interpretation again follows the assumption that simplifies the rotational dynamics of the MA cations, where the molecules with preferred orientations.

In summary, I will investigate the orientational disorder of $MAPbI_3$ with temperature using the technique of neutron total scattering coupled with the

RMC method. The pair distribution function analysis should provide detailed information about the short and intermediate-range order. Modelling of the total scattering and PDF data will provide new impetus to the characterization of the orientational dynamics of the highly mobile MA ions. Hopefully, the structural and dynamical properties could be further comprehended and even related to optoelectronic performance.

4.1.1 Neutron total scattering experiment

Neutron total scattering experiments were performed on the POLARIS diffractometer at the ISIS spallation neutron source. The sample temperature was controlled by a closed-cycle refrigerator (CCR) capable of heating above room temperature. Measurements were performed at temperatures of 10, 100, 155, 170, 293, 300, 320, 335, 350, 375, and 400 K. Data correction measurements were taken, at room temperature, of the empty instrument, empty CCR, and empty can within the CCR, together with a calibration measurement from a vanadium rod. Data for Rietveld refinement were obtained utilizing the Mantid software, and the GUDRUN package was used to obtain the corrected scattering functions and PDFs from the raw data.

4.2 Data processing

4.2.1 Rietveld refinement

First, the diffractometer constants were refined to fit the diffraction data. Since data were collected from multiple detector banks, the diffractometer constant DIFC was fixed for the highest-resolution bank and refined for lower-resolution banks to prevent unstable refinements due to high correlation between DIFC and the lattice parameters. The constant DIFC is explained in equation 2.7. The

aim is to correct the different positioning between the sample and standard for calibration. Peak shape function 3 was used to describe the peak profiles observed on the POLARIS instrument. During each refinement, the Lorentzian and Gaussian widths were also refined to match the shapes of the reflection peaks observed on POLARIS.

Orthorhombic phase The starting models were adopted from Weller's structure [60], but the H atoms were replaced with D atoms. The space group *Pnma* was used in the low-temperature refinement. The scale factor of each bank was refined to match the observed intensity. Six hydrogen atoms were included into the deuterated-sample model to check the deuteration degree. They were set to occupy the identical positions as those deuterium atoms by constraints, and the total occupancy was set to be refined as a whole. The converged model indicated that CD_3 were fully deuterated and ND_3 were partly deuterated. The total site occupancy of D in NO_3 was 0.5. The refined value of H/D occupancy was 0.109(3) and 0.391(3), so the ratio of H/D is about 0.2 on ammonium, and value was fixed for subsequent refinement. Soft restraints of C–N (1.460(1)), C–D (1.10(5)) and N–D (1.00(5)) were added [60], preventing the refinement diverging when refining all the atomic coordinates. The C–N bond was found to lie normal to the *b*-axis and orientation is fully ordered. The orthorhombic-to-tetragonal phase transition was reported to occur at 165 K, and the reported orthorhombic phase was successfully fitted to the observed diffraction pattern until 170 K. The ordered phase and the Rietveld refinement is illustrated in figure 4.2a.

Tetragonal phase For the room temperature phase, the tetragonal phase $I4/mcm$ was taken from Weller's work [60]. A previous QENS study has already shown that the rotational disorder of the MA group is dynamic [50]. The MA cations were found to be ordered end-to-end, and the C–N bond is four-fold orientationally disordered along the *c*-axis from the refined model.

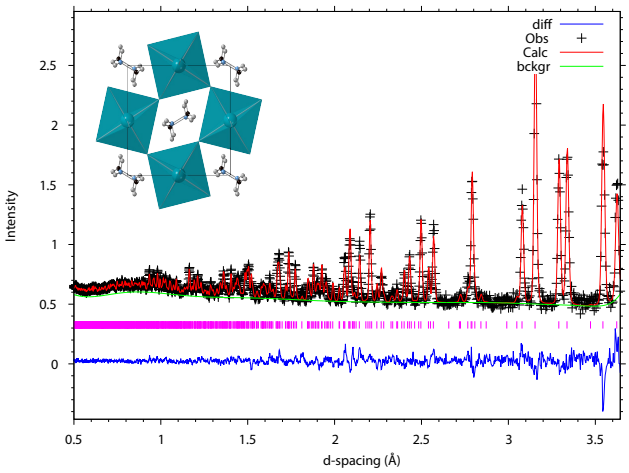

(a) 100 K

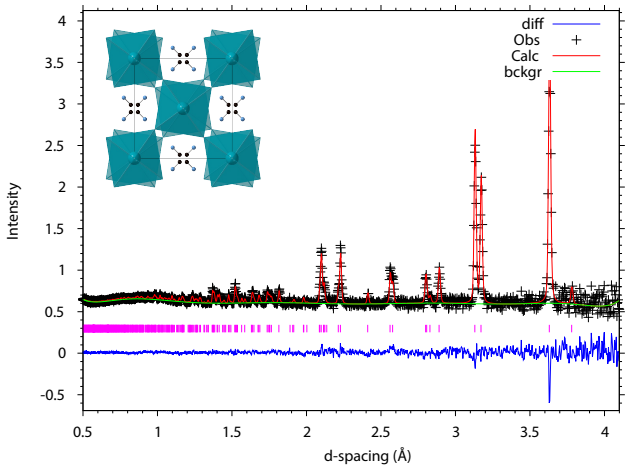

(b) 280 K

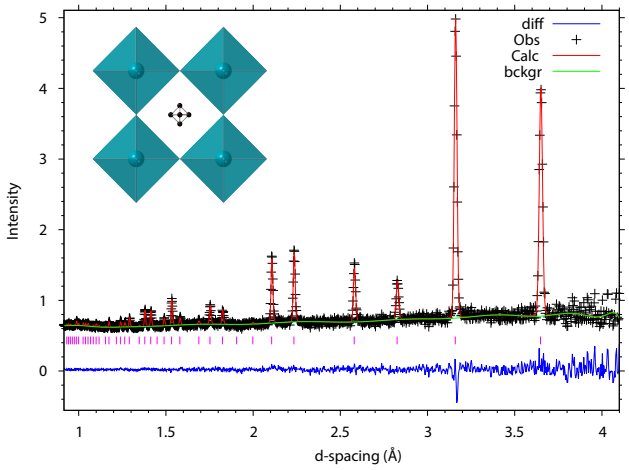

(c) 400 K

Figure 4.2: Three representative Rietveld refinement fits of three different phases and the average structures derived from Rietveld analysis viewed along the [001] direction. The deuterium and hydrogen atoms were hidden except in the orthorhombic phase, as the disorder of D/H makes the visualisation difficult.

By refining the ADPs of all the atoms, the refinement converged quickly, and large ADP values of deuterium and hydrogen confirmed the significant motion of the cations. The detailed structures are given in appendix A.2. However, the PbI_6 framework is less distorted than in the orthorhombic phase, as seen in figure 4.2b.

Cubic phase For cubic structure refinement, the space group $Pm\bar{3}m$ was used for temperatures above 320 K. The MA cation was refined to be disordered over six sites, as in figure 4.2c. Carbon and nitrogen atoms can be regarded as sitting on the equivalent sites, so only one atom C was used in the refinement for symmetry reason. Similar to all its inorganic analogues, $MAPbI_3$ was also refined in a way that iodine atoms have anisotropic ADPs, and the details are in appendix A.2.

At 330 K, the diffraction pattern from the high-resolution banks (bank 4 and 5) show that the (200) peak intensity does not match the experimental intensity very well. A closer look tells that two peaks were indeed observed in the experimental data, as seen in the tetragonal data. Then two-phase Rietveld refinement was carried out successfully, in agreement with previous Rietveld refinements [119]. The (200) reflection now splits into two reflection peaks (220)/(004). The scale factors of the two phases were allowed to be refined freely, and minimal cubic features of the diffraction data were present down to 300 K data. Therefore, the coexistence of both phases was assigned to the 300–330 K range, and the phase fractions at those mixture phases are given in table 4.1. The ratio of the cubic and tetragonal phases in the mixture-phase changes with temperature. The fraction of cubic phase changes on heating.

The lattice parameters extracted from Rietveld refinements are scaled by factors of 2 or $\sqrt{2}$ to better compare with each other and the lattice parameter of the cubic phase, shown in figure 4.3. For the tetragonal phase, $c/2$ was plotted. For the orthorhombic phase, $a/\sqrt{2}$, $c/\sqrt{2}$ and $b/2$ were plotted against

T(K)	fraction (cubic)	fraction (tetragonal)
330	0.715(16)	0.285(1)
320	0.614(6)	0.386(13)
310	0.488(5)	0.512(12)
300	0.18(3)	0.82(1)

Table 4.1: The phase fraction of the tetragonal and cubic phase in the two phase refinement.

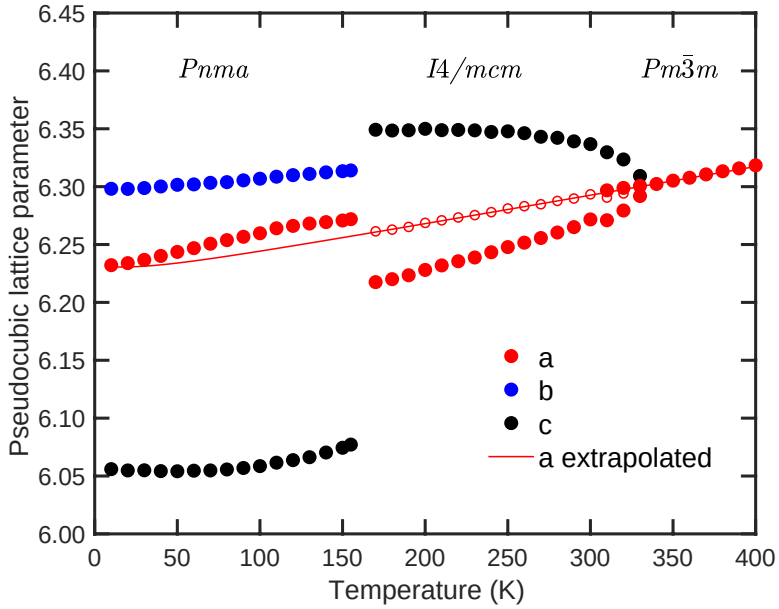

Figure 4.3: Pseudocubic lattice parameters a, b and c are represented in red, blue and black filled markers, and the average lattice parameter of the tetragonal phase is plotted with open circles. The red line is the extrapolation of the lattice parameter of the cubic phase.

temperature. Open circles are the average lattice parameters for the tetragonal phase.

In the tetragonal phase, the extrapolation of the cubic lattice parameter is defined as $a_0 = (2a + c)/3$. The value a_0 is extrapolated to low temperature by using a function of the form

$$a_0(T) = a_1 + a_2\Theta \coth(\Theta/T) \tag{4.1}$$

which describes both the linear dependence on temperature at high temperature and the limiting behaviour $\partial a_0/\partial T \to 0$ as $T \to 0$. The effect of the function is to have a curved and more flat end when approaching low temper-

ature. The choice of Θ is chosen to be Θ = 55 K and the obtained fitted values a_1 = 6.2168 Å and $a_2 = 2.5 \times 10^{-4}$ Å K^{-1}. The choice of Θ = 55 K was made to make the value of volume strain e_a more-or-less constant at low temperature, which will be discussed in detail in section 4.5.1. The value of a_2/a_1 represents the coefficient of linear thermal expansion at high temperature, equal to 40.2 MK^{-1}. This is similar in size to the coefficient of thermal expansion of $CsPbI_3$, 52 MK^{-1} in the cubic phase.

4.2.2 Total scattering data correction

The measured temperatures ranged from 10 K to 400 K with cryostat and furnace for low and high temperatures, respectively. Data correction was performed as two batches corresponding to two different sample environments. The total scattering data were collected from 5 banks on the POLARIS instrument, and individual bank's data were merged to give the final differential cross-section.

The large incoherent scattering from H atoms produces a background in the scattering data. If the H atoms are replaced by D atoms, the deuterated sample should in principle avoid the strong incoherent scattering. However, the complete sample deuteration is somewhat tricky. Furthermore, the perovskite samples suffer degradation problems when exposed to humidity. From Rietveld refinements, the refined occupancy suggested ND_3 was partly deuterated, so the assumption was that 20% hydrogen was in ND_3 only and 10% in total D atoms. The sample composition was changed accordingly as in table 4.2.

Deuterium atoms are light, and the unwanted inelasticity is always reflected in the data. The exchanged energy during the scattering process can not be neglected, though instrument scientists sought solutions to deal with inelastic-

ity correctly when designing the instrument. Nonetheless, data processing is complicated if inelasticity occurs. From chapter 2, we know the structure factor $S(Q)$ is divided into two parts, distinct or so-called interference scattering and self-scattering as in equation 2.18. The structural information is contained in the interference term, which oscillates about a baseline set by the coherent scattering from different atoms. It has been recognized that inelasticity affects the self-scattering part the most, while the interference scattering is affected only minimally. The primary effect was believed to make the bond distance slightly longer, but no new peaks are introduced in the Fourier transformed data $D(r)$ [95]. Experience has shown the most significant impact was on the lowest-r peaks in the PDF. Hence, the aim is to subtract the self-scattering term and get the correct interference scattering term. It should be noted there is limited resources for reference use to perform data correction on such light atom containing samples, and the knowledge is based on the experience with various samples. The corrected PDF data can be eminently sensible with the parameters used in the data processing software, so I had to try with different values and run RMC with the corrected $D(r)$ and $i(Q)$. The good thing is RMC will calculate $D(r)$ and $i(Q)$ with the starting model, and the integral of the first peak in $D(r)$ is used to check the experimental PDF and the criterion is whether it equals to the coordination number associated with the nearest atom pair.

Figure 4.4 shows the merging between different banks. Compared with the $CsPbI_3$ sample with heavy atoms only (figure 3.4), $MAPbI_3$ sees the absolute level of the measured data not agreeing well at all. Data measured at different detector angles are weighted by the statistical accuracy in the merging process. If the range of each detector bank data is not chosen properly, small steps could be introduced into the merged data. In principle, one can look at the data from each group and make a decision based on whether structural information or

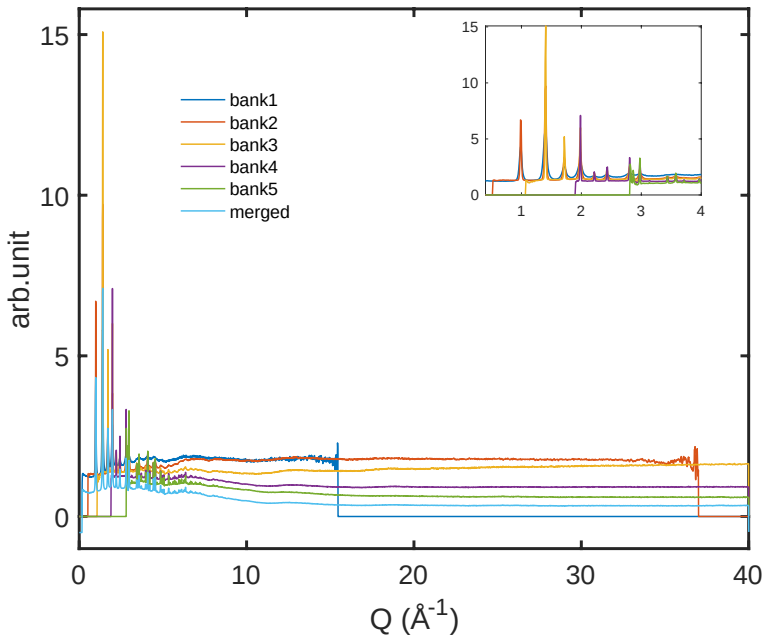

Figure 4.4: Each bank's differential cross-section data and the merged one were plotted to illustrate the merging process. A comparison between $MAPbI_3$ could be drawn with its inorganic analogue, where no light atoms are present, to demonstrate the effect of inelasticity in the data. The merged data has been added an offset to aid the comparison. The high Q region shows different bank measures the data with such a different result, and the inset shows that below 2 Å the DCS data are aligned consistently.

only the noise is present in the data. However, this method does not work in the case of $MAPbI_3$ due to the marked difference between detectors. Ultimately, the cut-off for each detector bank was set between 0.0 and 60.0 to avoid steps in the merged data.

The Q range used in Fourier transform was tweaked to not include too much noise, and was chosen to be 0.5 and 40.0 $Å^{-1}$. Also, the minimum r in Fourier transform was set as 0.88 Å to clean any spurious structures in real space. The value is inferred from the minimum distance of any atom pairs. Here, the first peak must be the combination of the C–D (1.09 Å) and N–D (1.04 Å) bonds from Rietveld refinement results.

The significant self-scattering background in the total scattering data was removed with the top-hat function, as discussed in section 2.6.3. Instead of

Atom	Isotope	Atoms/unit cell
H	2	5.4
C	0	1.0
N	0	1.0
Pb	0	3.0
I	0	6.0
H	0	0.6

Table 4.2: The sample atomic composition used in pair distribution function analysis. D/H ratio was changed according to the Rietveld refinement to keep consistency. Here, 0 means terrestrial abundance.

using a negative top-hat width, where the average of the total scattering data from Q_{T} to Q_{max} is subtracted from the data itself, the top-hat correction needs to be performed to get rid of the Q-dependent self-scattering. The width of the top-hat function was approximated by an empirical equation $3/r_{\mathrm{min}}$ [123], where r_{min} is 0.88 Å. The value was set to 3.0 $\mathrm{Å}^{-1}$ for all temperatures. After the top-hat correction, the self-scattering and background were subtracted, and only the interference differential cross-section was achieved as expected.

4.3 RMC modelling

Data included in RMC simulation were the scattering function $i(Q)$, the PDF $D(r)$ and the Bragg profile extracted by GSAS. Initial configurations were prepared using the RMCcreate tool, adapted to allow for the molecular ions to be oriented in any chosen state. Configurations for the cubic phase were prepared to contain $8 \times 8 \times 8$ formula units, with an approximate configuration edge length of 50 Å and 6144 atoms. For tetragonal and orthorhombic phases, starting configurations were prepared to contain $6 \times 6 \times 4$ and $6 \times 4 \times 6$ unit cells, with 6912 atoms each. A range of starting states were explored, including various degrees of the order or completely random disorder. Because of the molecular disorder, the MA molecules in the cubic and tetragonal phase were oriented randomly, and remained ordered in the orthorhombic phase.

atom pair	HT	RT	LT
C–N	1.38–1.65 Å	1.35–1.64 Å	1.38–1.65 Å
Pb–I	3.30–5.65 Å	3.30–5.65 Å	3.30–5.65 Å
I–I	2.55-4.95 Å	2.55-4.95 Å	-

Table 4.3: Distance window used in RMC for all temperature runs, including three phase at high temperature (HT), room temperature (RT) and low temperature (LT).

bond-stretching potential	D(eV)	r_0(Å)	bond-angle potential	D(eV)	angle(°)	r_0 (Å)	r_0 (Å)
C–N	2.551	1.505	D–C–D	6.866	107.6	1.06	1.06
C–D	2.275	1.06	D–N–D	6.866	107.6	1.06	1.06
N–H	2.947	1.06	D–N–H	6.866	107.6	1.06	1.06
N–D	2.947	1.06	H–N–H	6.866	107.6	1.06	1.06
			N–C–D	9.487	111.0	1.505	1.505
			C–N–D	9.487	111.0	1.505	1.505
			C–N–H	9.487	111.0	1.505	1.505

Table 4.4: Bond potential used in RMC for all temperature runs. Interatomic potentials include both the bond-stretching and bond angle potentials.

From the Rietveld refinement, the ND_3 group contains some H atoms. So the starting configurations produced for RMC have replaced 20% D bonded to N with H atoms, and CD_3 remained purely deuterated. The configuration was built using RMCcreate tool.

Distance window constraints were added to guide RMC and produce physically reasonable structures (see table 4.3). Potentials that describe the MA molecule were also included see table 4.4. These two constraints were discussed in section 2.7. It was found that including both potentials and distance window in RMC does not give good fits. The reason could be these two were competing, and the structure can not accommodate these two constraints simultaneously. In the end, only Pb–I, I–I and C–N were constrained as shown in table 4.3.

Representative fits are plotted in figure 4.5. The peak at 3.2 Å corresponds to the Pb–I bond, and the peak intensity of RMC data was much lower than of experimental data, suggesting the atomic density under the Pb–I peak is lower in simulation than experiment, but RMC cannot increase the intensity if the

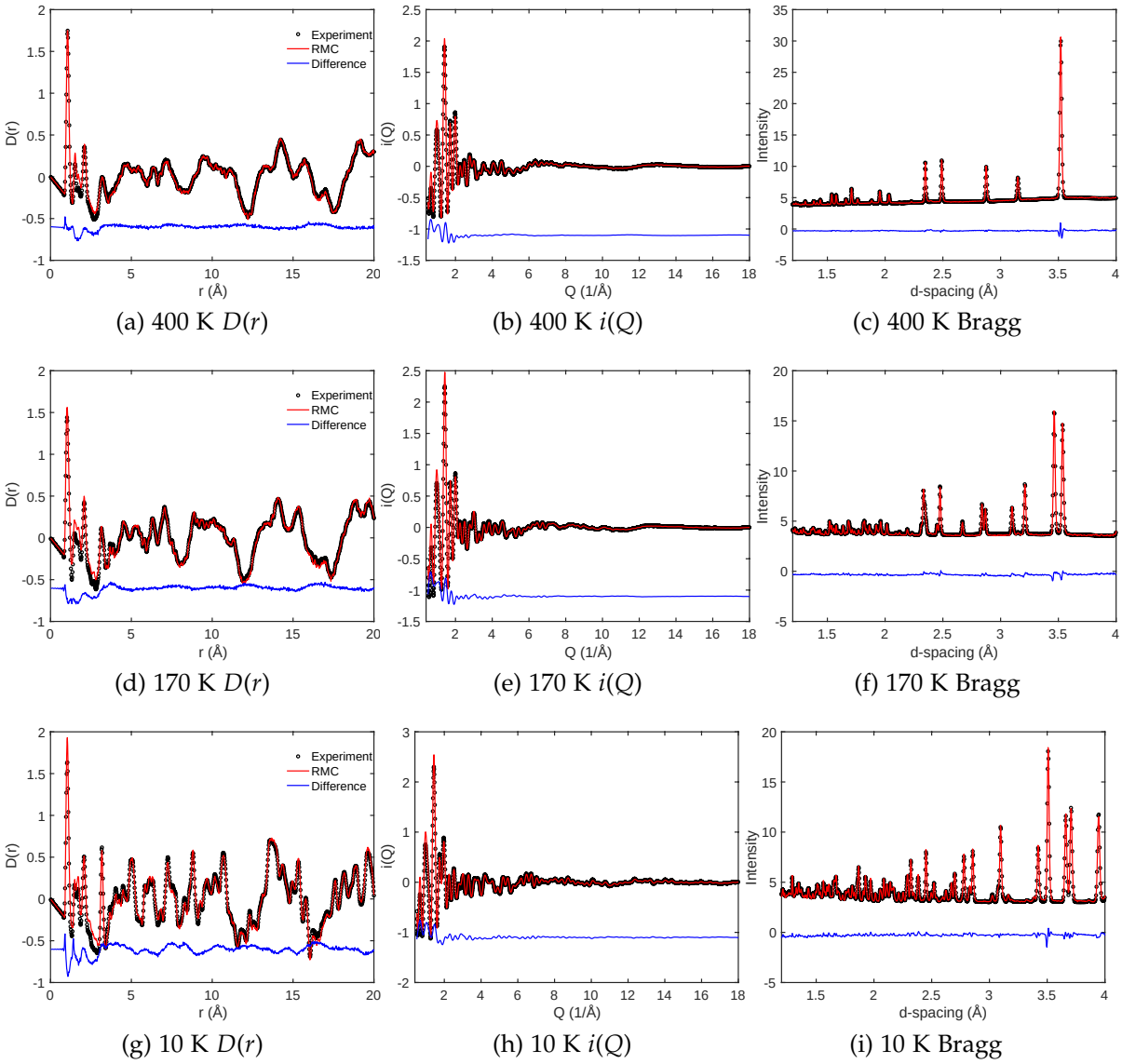

(a) 400 K $D(r)$ (b) 400 K $i(Q)$ (c) 400 K Bragg

(d) 170 K $D(r)$ (e) 170 K $i(Q)$ (f) 170 K Bragg

(g) 10 K $D(r)$ (h) 10 K $i(Q)$ (i) 10 K Bragg

Figure 4.5: Representative RMC fits to the experimental data, including $D(r)$, $i(Q)$ and Bragg diffraction for the HT, RT and LT phases. Bragg data has been transformed to d-spacing from time-of-flight.

simulation time limit is increased.

In figure 4.6, the supercell configuration of atoms in the cubic phase are collapsed into one unit cell. Only the molecules are shown. From the graph, the distribution of C and N atoms seem to form a ball with head-to-tail motion, while the distribution of D and H atoms form a shell outside the CN^-. What this reveals is the C and N atoms inside the cage are very disordered and

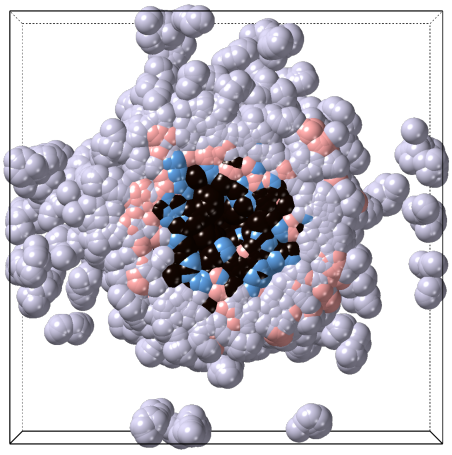

Figure 4.6: A sliced plane of the collapsed unit cell of the RMC configuration at 400 K. Black and blue balls represent for C and N atoms, while pink and silver balls are H and D atoms.

apparently translating a considerable distance as well as rotating. That is, the disorder is not simply a case of the molecule rotating about its centre of mass.

4.4 Structural analysis

4.4.1 Local structure analysis

The PDFs are plotted up to 18 Å in figure 4.7 as a function of temperature. The inset in figure 4.7 shows the atom pairs inside the molecule, and there are no obvious changes through phase transitions. The first peak in $D(r)$ is the mixture of two atom-pairs, C–D and N–D/H. The second peak belongs to the C–N pair and does not vary significantly with temperature across the phase transitions, and the third peak that represents D/H–D/H pair broadens when transforming to the cubic phase. The peak located at 2.1 Å corresponds to the longer distance of C–D/H and N–D within the CD_3ND_3 molecule.

The total scattering measurement went down to as low as 10 K, and the PDF at this temperature indicates the single Pb–I peak at 3.2 Å is relatively sharp, and the peak grows broad on heating. The temperature effect is seen

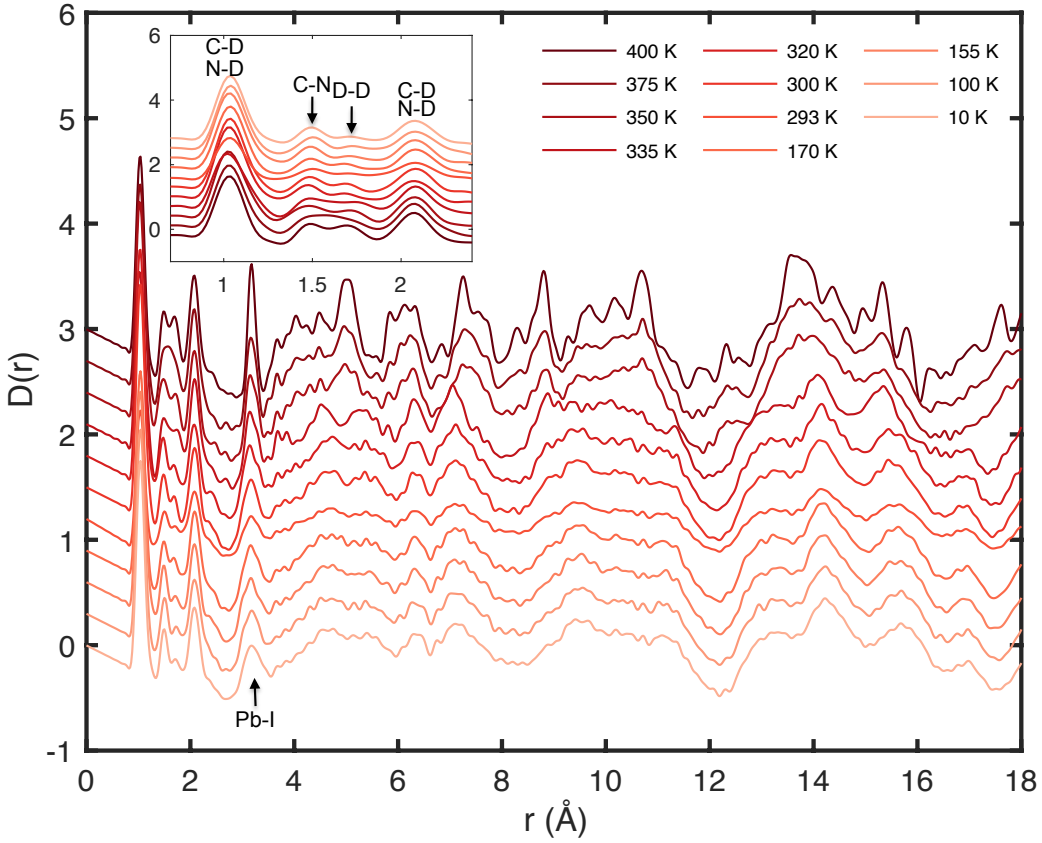

Figure 4.7: $D(r)$ calculated for each temperature from the scattering function $i(Q)$. There are clear changes through the two-phase transitions, cubic-to-tetragonal and tetragonal-to-orthorhombic. The first three peaks originate from the MA molecule, and little changes have been observed with the increasing temperature, consistent with the literature. The Pb–I peak at 3.2 Å is sharper at low temperatures due to smaller thermal motion.

not exclusively through the broadening of the individual peaks, but the peak also slightly shifts to smaller d when heating. Although the phase transition has been reported to occur at 327 K, the PDF at 320 K does not reveal a strong signal of cubic or tetragonal features. This is perhaps not surprising given the co-existence of cubic and tetragonal phases from Rietveld refinement. The similarity between the local structures of tetragonal and cubic phases indicates the local environment of the MA cation remains almost unchanged in terms of the atom-pair distances. However, it should be noted the relative intensities of the second, and the third peak changes, and if we combine that with the peak

Atom pair	$c_i c_j b_i b_j$(fm^2)
H–H	0.035
H–C	-0.207
H–N	-0.292
H–Pb	-0.293
C–C	0.307
H–I	-0.494
N–N	0.608
Pb–Pb	0.614
C–N	0.864
C–Pb	0.868
D–H	-1.122
N–Pb	1.223
C–I	1.462
I–I	1.742
N–I	2.059
I–Pb	2.069
D–C	3.325
D–N	4.683
D–Pb	4.706
D–I	7.925
D–D	9.012

Table 4.5: Faber-Ziman partial structure factors for the partial pair distribution functions $g_{ij}(r)$ to combine as the total PDF.

as mentioned earlier, the C–N bonding is relatively robust and the D/H–D/H have large thermal motion, which is in agreement with the reported rotational disorder of the molecular ion.

The weighting factors for each partial PDF are given in table 4.5. These are the weighting factors to sum each $g_{ij}(r)$ to get the total $G(r)$. The biggest coefficient, 9.01 fm^2 is from the D–D pair, while the C–N is only 0.86 fm^2.

4.4.2 Orientational disorder

Representative configurations of three different phases are shown in figure 4.8. From these refined configurations, MA molecules remain highly disordered in the high-temperature cubic phase and intermediate-temperature tetragonal phase, but the molecules are aligned in the orthorhombic phase. Generally,

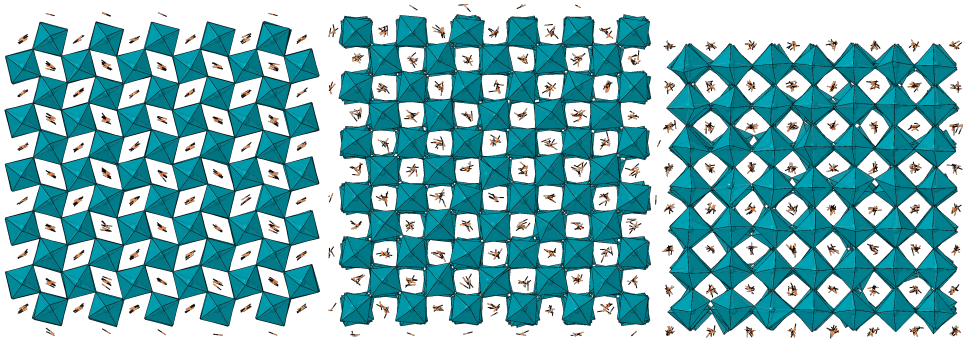

(a) (b) (c)

Figure 4.8: The configurations at three phases from RMC simulation. View from [010] direction for (a) orthorhombic phase, and [001] direction for (b) tetragonal and (c) cubic phase. C–N are sketched as sticks and rotated randomly in the cubic phase to the right of the graph, while they are aligned u in the orthorhombic phase. The PbI_6 framework is drawn in blue octahedra and the molecules are simplified as sticks that are equivalent to the C – N bonds.

orientational disorder is described by the distribution function $P(\Omega)$ [124], where Ω is defined as the pair of polar angles (θ, ϕ) with θ as the zenith angle and ϕ as the azimuthal angle ($0 \leq \theta \leq \pi$, $0 \leq \phi \leq 2\pi$). Here, θ is the polar angle, measured from the z axis, while ϕ is the azimuthal angle, measured from the x axis. $P(\Omega)$ is the full set of the bonds lying within a surface. By integration over all solid angles $\mathrm{d}\Omega = \sin\theta\,\mathrm{d}\theta\,\mathrm{d}\phi$,

$$\iint P(\Omega)\sin\theta\,\mathrm{d}\theta\,\mathrm{d}\phi = 1 \tag{4.2}$$

For molecules lying on sites of cubic symmetry $m\bar{3}m$, it is convenient to expand $P(\Omega)$ in terms of Kubic harmonics [124, 125]:

$$P(\Omega) = \frac{1}{4\pi}\sum_{\ell=0}^{\infty} c_\ell K_\ell(\Omega) \tag{4.3}$$

where ℓ is the order of Kubic harmonics. The Kubic harmonics term K_ℓ is the specific linear combination of the spherical harmonics, $Y_\ell^m(\theta, \phi)$. Like in Fourier transform analysis, the expansion is comprised of the sum of a series of sines and cosines to describe any given function. The spherical harmonics are also defined to represent arbitrary functions defined on a sphere. We

usually choose a limited number of terms and then terminate the expansion. The coefficients, $c_\ell = \langle K_\ell \rangle$ are the average of the Kubic harmonics over all molecules in a set of configurations. These Kubic harmonics terms are given in equation 4.4, and they are totally symmetric because of the cubic symmetry with respect to the crystallographic axes.

$$K_0 = 1 \tag{4.4a}$$

$$K_4 = \frac{\sqrt{21}}{4}(5Q - 3) \tag{4.4b}$$

$$K_6 = \frac{\sqrt{13}}{8\sqrt{2}}(462S + 21Q - 17) \tag{4.4c}$$

$$K_8 = \frac{\sqrt{561}}{32}(65Q^2 - 208S - 94Q + 33) \tag{4.4d}$$

$$K_{10} = \frac{\sqrt{455}}{64\sqrt{2}}(7106QS + 187Q^2 - 3190S - 264Q + 85) \tag{4.4e}$$

$Q = x^4 + y^4 + z^4$ and $S = x^2y^2z^2$, where $x = \sin\theta\cos\phi$, $y = \sin\theta\sin\phi$ and $z = \cos\theta$. The K_2 term is not possible due to symmetry. If the molecules are randomly oriented across the full unit sphere, then $P(\Omega) = 1/4\pi$.

We characterise the degree of order by focussing on the three-dimensional orientations of the C–N bonds. The full three-dimensional orientational distribution that includes the C–D and N–D/H bonds will be much more disordered. The experimental C–N distribution function extracted from all 512 MA cations in 30 configurations is close to the true experimental distribution.

Cubic phase Figure 4.9 is the experimental data for $P(\Omega)$ calculated function, and figure 4.10 shows the three-dimensional representations of the form of $P(\Omega)$ described by equations 4.3. The data were collected on both heating and cooling in the order of 350, 400, 375, 335 and 320 K. The Kubic harmonics terms were used up to K_{10}. Compared with other orientationally disordered crystals, the cubic phase of MAPI shows values very near a uniform distribution at all temperatures. For instance, for SF_6 [125], $P(\Omega)$ shows a clear maximum in the $\langle 100 \rangle$ direction and elsewhere the probability distribution function is below

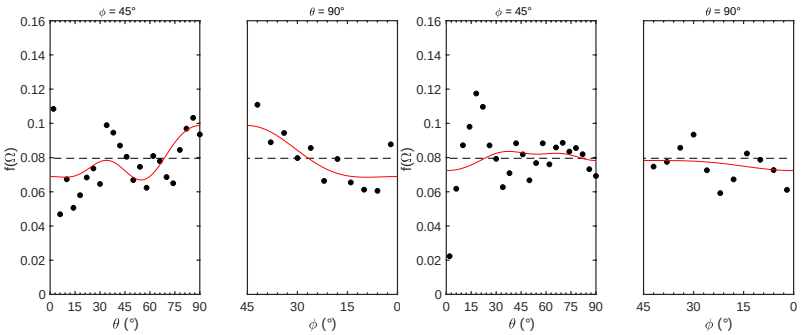

(a) 320 K (b) 335 K

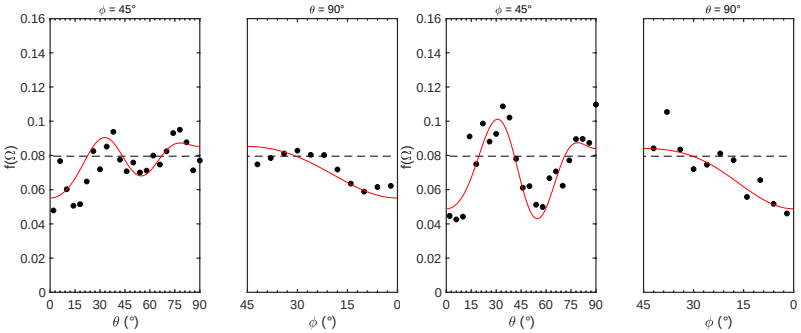

(c) 350 K (d) 375 K

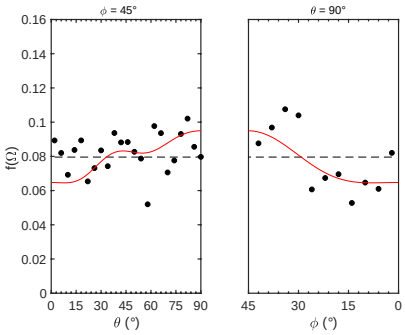

(e) 400 K

Figure 4.9: The partially symmetrised orientation distribution function (black dots) of C–N bond and the function calculated using Kubic harmonics (red lines) at various temperatures. The black broken line indicates $1/4\pi$, which represents the completely random orientation distribution. The left figure includes the direction from $\langle 001 \rangle$ to $\langle 110 \rangle$ and the right figure includes the direction from $\langle 110 \rangle$ to $\langle 100 \rangle$.

random. The isotropic rotational model is also in agreement with the previous assumptions [36, 61]. There are some maximum values of the $P(\Omega)$ near $\langle 110 \rangle$ direction and a preference towards directions in the (011) planes at an angle of around 30° to the nearest major axis.

In figure 4.10, the last five figures describe the high-temperature cubic molecular orientations. The colour has been scaled for all the representations of molecules. There are no obvious maxima on the spheres even the shapes of the molecules are different. However, these shapes can not be over interpreted as preferred orientations in the cubic phase. These near-isotropic spheres indicate the molecules are almost freely-rotating, a different scenario from some orientationally-disordered solids that have well-defined orientations. From chapter 2, it was introduced that RMC simulation is based on a set of experimental data and follows statistical mechanics. Thus, RMC will generate the model with more disorder that maximises the entropy. It is worthwhile to check whether RMC overestimates orientational disorder. One example is another orientationally disordered solid, d-adamantane. The RMC study on this material has proved the sensitivity of the well-defined orientations if they exist [58]. Therefore, it is credible that molecular ions have a nearly random orientational disorder in the high-temperature cubic phase of $MAPbI_3$.

Tetragonal phase The site symmetry of the MA cation in the tetragonal phase is $\bar{4}2m$, and the MA molecule itself has the symmetry as $3m$. Attempts have been made to fit the orientations of the MA cations via atomic sites with partial occupancy and allowing significant thermal displacement parameters [60]. However, two different models, allowing or not allowing head-to-tail disorder, have been reported, both apparently with satisfactory agreement between the observed and calculated diffraction patterns [119]. Because they allow large ADPs, the difference between C and N would not be significant.

In figure 4.10, the orientational order between the two room-temperature data (293 K and 300 K) appears to be very similar. The data at room temperature are much closer to random, whereas the data at 170 K start to show a preference for the ordering of the C–N bonds in the tetragonal (110) planes at angles of around $\pm 20^\circ$ to the (001) plane. Obviously, there is a significant

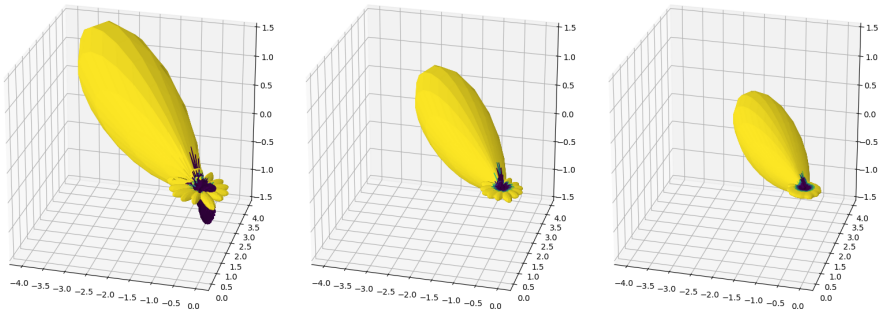

(a) 10 K (b) 100 K (c) 155 K

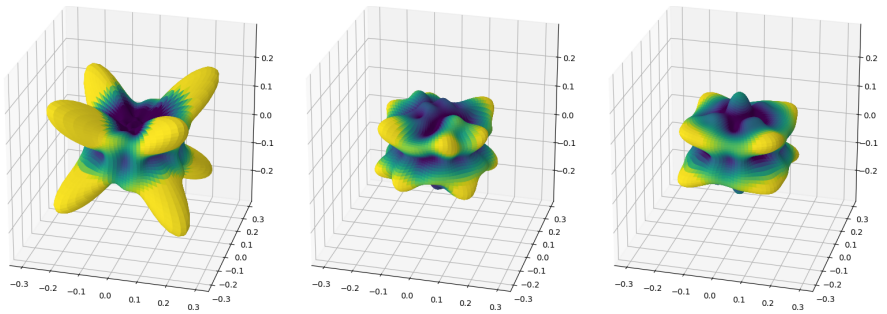

(d) 170 K (e) 293 K (f) 300 K

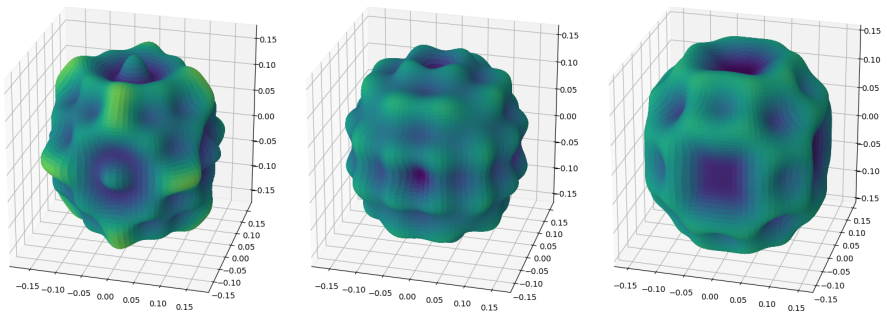

(g) 320 K (h) 335 K (i) 350 K

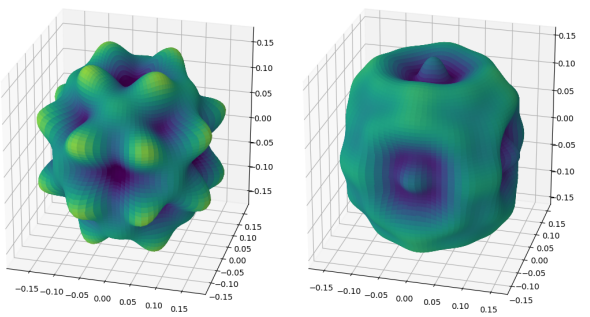

(j) 375 K (k) 400 K

Figure 4.10: The spherical harmonics representation of the MA molecule in three-dimensional space.

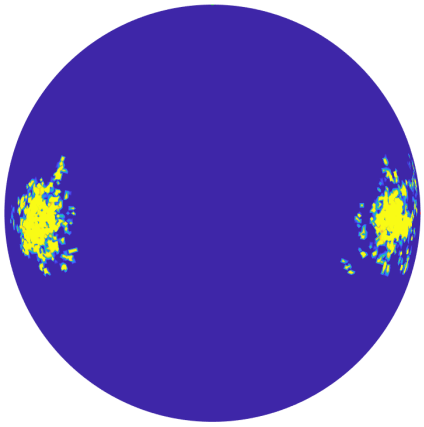

Figure 4.11: The orientation of C–N bonds from 10 K RMC configuration have been plotted in the sphere diagram. View from [010] direction shows that the C–N axis lies in the xz plane and remains highly ordered. The yellow colour is with more density while blue is the opposite.

difference between the room-temperature phase model and the cubic-phase ones. The C–N bond could be viewed as experiencing the ordering process from entirely disordered for a more ordered state, but a high degree of orientational disorder is still visible just below the transition point. Interestingly, this ordering of the MA cation in the tetragonal phase reflects a continuous process on cooling.

Orthorhombic phase Unlike the tetragonal and cubic phases, the site symmetry m allows complete orientational order of the MA cations. In figure 4.10, the molecules are aligned in a single orientation unlike the higher symmetry phases. The purple region at one end comes from the error rather than maximum. Moreover, the distribution functions of molecules are more elongated at lower temperatures within the orthorhombic phase, suggesting a more obvious preference in that direction.

Figure 4.11 shows the orientational distribution as an orthographic projection of the C–N bond to the sphere. It can be observed that only a slight degree of orientational disorder is present in the 10 K data, which is the result

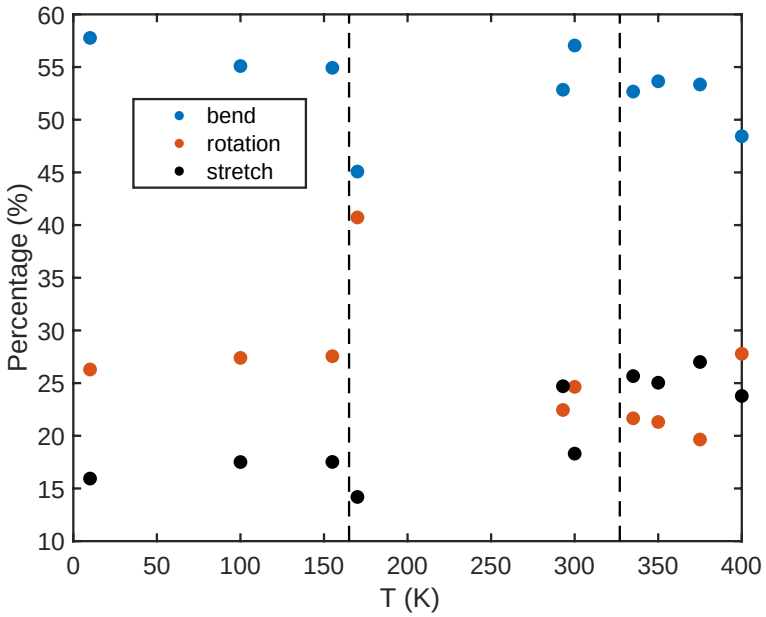

Figure 4.12: The breakdown of three motion inherent to the PbI_6 coordination octahedra. Bending contributes to the total motion as the biggest component at all temperatures, but the rotation and stretching are competing.

of thermal vibrations rather than the translational and rotational disorder as in the tetragonal and cubic phases. The bond orientation of C–N is calculated based on 30 configurations for statistics.

4.4.3 Rigidity analysis

A previous study confirmed the coupling between the PbX_6 octahedra and MA rotation has a strong impact on the optical properties, for example, the absorption spectrum [126]. Geometric analysis on the PbI_6 coordination network could separate the effects of the framework and the cations at the centre of the cavities, as discussed in section 2.8.

The flexibility of the octahedral network of the inorganic perovskite $CsPbI_3$ was assessed using GASP in chapter 3. Because $MAPbI_3$ has the same PbI_6 framework as $CsPbI_3$, the framework flexibility and the polyhedra rigidity were assessed for the cubic phase. Similar to $CsPbI_3$, the total motion of $MAPbI_3$ was broken into three components, the bending of the Pb–I–Pb bond (M_{bend}),

the whole-body octahedral rotation (M_{rotation}) and the stretching of the Pb–I bond (M_{stretch}). The total motion extracted by GASP from 30 configurations is plotted in figure 4.12.

If we compare the GASP results for the two perovskites, then M_{bend} has the fraction in total mismatch as 0.51 ± 0.03 in the cubic phase for $MAPbI_3$, identical within estimated uncertainty to the value of 0.52 ± 0.04 for $CsPbI_3$. The standard deviations are calculated from 30 configurations. It should be noted that 320 K data were excluded, because the coexistence of two phases was confirmed in the later analysis, and the two-phase RMC refinement is not compatible with the RMCprofile version used. In $CsPbI_3$, the rigid-body rotation component is higher than the bond-bending one. We attribute this to the higher energetic cost when stretching the bonds. For $CsPbI_3$, the PbI_6 whole-body rotation contributes 0.30 ± 0.04, and the bending only 0.18 ± 0.02 in the cubic phase. However, it is surprising that stretching is more prevalent than the PbI_6 rotation in $MAPbI_3$, indicating the distortion of the octahedra is more severe than in $CsPbI_3$.

In the tetragonal phase, data were collected at three temperatures and the simulation time for 170 K data is twice that of others. The temperature of 170 K sees the phase just transforming to tetragonal from the orthorhombic phase, but the relative percentage of each motion may be nothing but an artefact.

In the orthorhombic phase, the percentages of three motions are similar to the cubic phase of $CsPbI_3$. The bending component decreases with temperature, while the other two components increase with temperature. There is more motion related to the PbI_6 whole body rotation and stretching of the bonds at higher temperature.

Figure 4.13 plots the distribution functions of the PbI_6 rotation angles with the variable being temperature, based on the geometric analysis of the polyhedral network from 30 end-RMC configurations for each temperature.

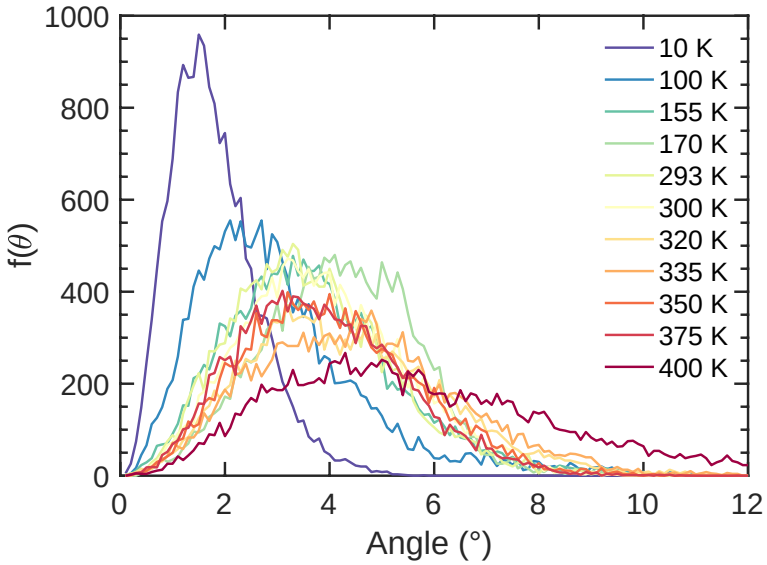

Figure 4.13: Angle distribution functions of the PbI_6 whole-body rotations from GASP calculation at different temperatures.

The rotation angles are calculated from the comparison with the undistorted starting configuration, and the distribution data were not normalised. As the rotation angle approaches zero, $f(\theta)$ is nearly zero because there is very little polyhedral motion in this range. The octahedral motion is less at the lowest temperature of 10 K, and significant growth in the magnitude of the rotation angles occurs when the temperature is higher within the orthorhombic phase is observed. In the tetragonal and cubic phases, the shape of each distribution does not change in a significant way. This might be associated with the behaviour shown in figure 4.12. At 400 K, the whole-body rotation is a greater fraction of the total distortion than of stretching, which is different from what occurs at other temperatures where the cubic phase is seen.

4.4.4 Distance distribution analysis

The Pb–I bond exhibits anharmonicity in $CsPbI_3$ as presented in chapter 3, and the same Pb–I bond was examined in the case of MAPI. The distance distribution is illustrated in figure 4.14 for the three phases. Here normalisation

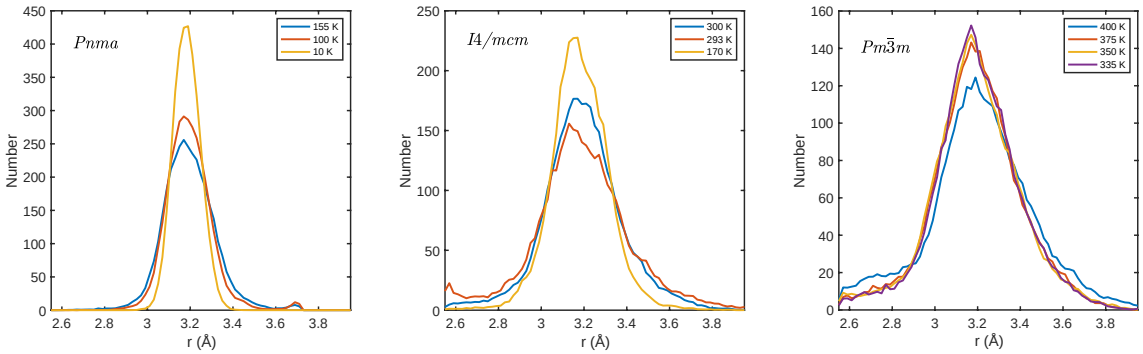

Figure 4.14: Distance distribution functions of Pb—I bond with temperature dependent.

was not performed.

Figure 4.14 shows the distance distribution of the Pb–I bond in the different phases. In the orthorhombic phase, the shapes of the distribution functions are highly symmetric. The peak grows higher and sharper on cooling, which is reasonable as the framework has less thermal motion. In the middle of the figure 4.14, three temperatures in the tetragonal phase are presented. The data at 293 K were measured in the cooling process, where the data at the other two temperatures were collected in the heating process after cooling. This explains why the peak width observed at 300 K is smaller than at 293 K. In $CsPbI_3$, five data sets at different temperatures in the cubic phase were collected, but there were little changes of the Pb–I distance distribution with temperature. In the cubic phase, 335, 350 and 375 K data show similar distributions and the slight changes in peak intensity and width follow the variation of temperature. More strictly, the 400 K distribution data are slightly different from other temperatures in figure 4.14. The curve has a more asymmetric shape than at other temperatures, even in the same phase. It could be better described by the anharmonic potential, and again, the Morse potential was chosen as in the case of $CsPbI_3$.

As shown in chapter 3, the Pb–I bond was modelled as two atoms joined by a harmonic spring and the vibrational angular frequency is $\omega = \sqrt{k/\mu}$, where

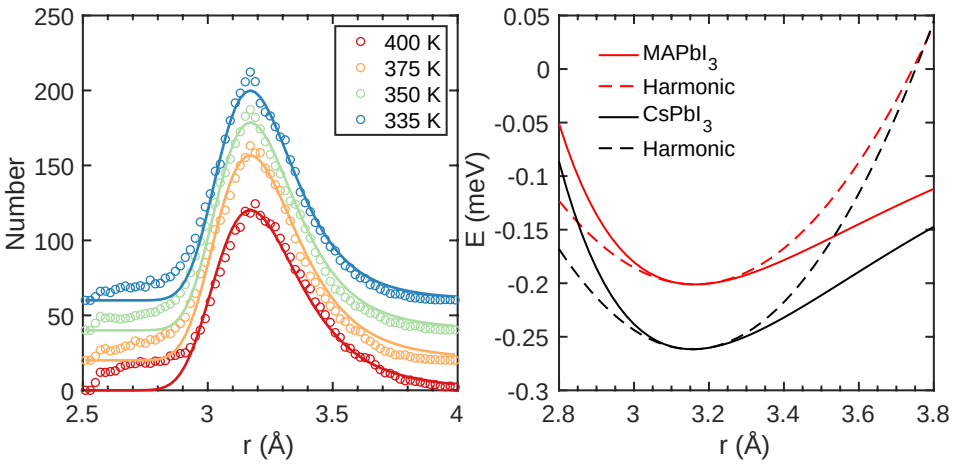

Figure 4.15: Left: Distance distribution functions of Pb–I fitted with Morse potentials. Right: Fitted Morse potential and the harmonic potential for $CsPbI_3$ and $MAPbI_3$.

$\mu = 78.7\,\mathrm{g\,mol^{-1}}$ is the reduced mass. The distribution data were fitted to the Boltzmann form $P(r) \propto \exp(-\phi(r)/k_\mathrm{B}T)$, where $\phi(r)$ is the Morse potential. The fitted distance distributions are shown in figure 4.15 with the Morse potential in equation 3.1. The fitted three parameters are r_0, α and k. Data for four temperatures were fitted simultaneously, over the range of r between 2.51 Å and 3.99 Å. The fitting is very good but some discrepancy below 2.9 Å was observed, which might originate from a wider distance window to the left of the data used in RMC modelling. The best-fit parameter values are $\alpha = 1.72 \pm 0.06$ Å^{-1}, $r_0 = 3.162 \pm 0.001$ Å, and $k = 1.19 \pm 0.06$ eVÅ^{-2}. The fitted average r_0 is very similar for $CsPbI_3$ and $MAPbI_3$ (3.162 Å and 3.1559 Å), but $MAPbI_3$ has a bigger value due to the larger dimension of the unit cell. From these values, the bond dissociation energy was calculated to be $D = k/2\alpha^2 = 176$ meV, smaller than that in the case of $CsPbI_3$ (262 meV). Substituting in the fitted values of k and α, an angular frequency of ω =12.167 THz was obtained. The value of frequency is a bit smaller 8% than what was obtained for $CsPbI_3$ where ω = 13.2 THz.

Figure 4.15 b plots the Morse potentials fitted to the distribution data of the two perovskites and also the harmonic potentials for each case. By comparison, the well depth of the potential is shallower for $MAPbI_3$ than $CsPbI_3$, as suggested from the bond dissociation energy D. Simply considering Hooke's law, the harmonic potential is calculated with the fitted parameters in each case, by

$$E_{\text{harm}} = \frac{1}{2}\frac{\partial^2 E}{\partial r^2}(r - r_0)^2 \tag{4.5}$$

where E is the Morse potential. The gap between the solid line and the dashed line at high r region suggests that $MAPbI_3$ is less anharmonic than $CsPbI_3$. After scaling the energy profile of both $CsPbI_3$ and $MAPbI_3$, there is not much difference in terms of the relative changes at high r. Therefore, the divergence between the harmonic and anharmonic model implies that the anharmonic effects in the nuclear displacements are common in both $CsPbI_3$ and $MAPbI_3$ and the degree of anharmonicity is similar for the two materials..

4.4.5 Flexibility of the Pb–I–Pb linkage

The Pb–I–Pb linkage should in principle remain 180° in the cubic phase; however, fluctuation occurs due to thermal vibrations of the atoms. Especially the large amplitude of the iodine atoms would strongly deform the linkage linearity. In those two lower-symmetry phases, the octahedral network is connected but with different rotations of the PbI_6 octahedra at adjacent planes, e.g. the out-of-phase rotations of the PbI_6 polyhedra in the tetragonal phase and the counter rotations within the xz plane in the orthorhombic phase.

The temperature effect on the Pb–I–Pb linearity is illustrated in figure 4.16. The Pb–I–Pb angle was separated into two angles in different directions; parallel and normal to the [001] direction.

In the orthorhombic phase, the Pb–I–Pb linkage in different directions show

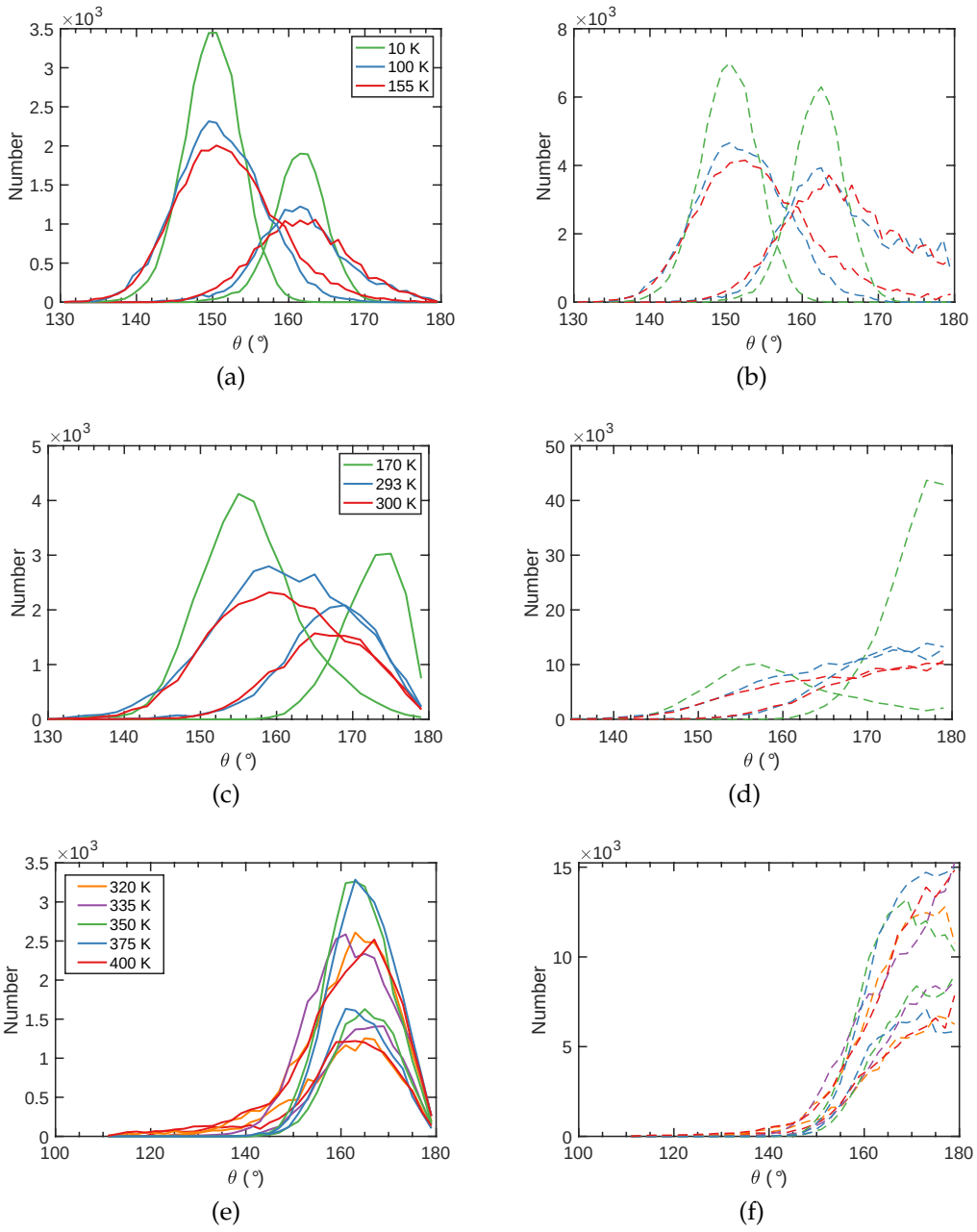

Figure 4.16: Left: The angle distribution functions $f(\theta)$ of the Pb–I–Pb angle, plotted for the direction parallel and normal to the [001] axis. Right: The normalised distribution functions $f(\theta)/\sin(\theta)$.

clearly two distinct peaks, at 150° and 162°. Surprisingly, in the tetragonal phase, these two angles (155° and 175°) at the lowest temperature 170 K show a substantial shift to 158° and 169°. The framework transforms into a phase that is less distorted. A previous neutron study showed that in the

tetragonal phase, the average Pb-I-Pb angles are roughly 165.3° at 180 K [60]. Here the local structure suggests the average angle is about 163.5° at 170 K, which is relatively consistent with the reported value. The small difference between these two values could be attributed to the temperature effect where the PbI_6 framework distorts less at higher temperatures. In the cubic phase, the distributions show little dependence on the temperature and direction. The two Pb–I–Pb angles become indistinguishable in the highly-symmetric cubic phase. Figure 4.16 b shows a gradual process of the changing of the linear Pb–I–Pb angle, which implicitly explains that the tetragonal-to-cubic phase transition occurs with the small displacements of atoms. It characterises the phase transition with a displacive feature without considering the molecular cations.

Compare the Pb–I–Pb bond angle distributions with the corresponding functions for Ti–O–Ti in $SrTiO_3$ [112] and Sn–O–Sn in $SrSnO_3$ [113]; other functions were not given in these two publications. The departures from linearity of the Pb–I–Pb bond angle is larger by around 10° than in $SrSnO_3$, whereas at the highest temperature the corresponding angle is just 4° from linearity in $SrTiO_3$. The Ti–O–Ti angle fluctuations are small even at high temperatures, so the effect of temperature is not the reason for linearity.

4.4.6 Pseudo-dipole analysis

Considering the Pb–I bond, there are six neighbouring iodine atoms of each lead atom in the centre. The average of the six Pb–I dipole vectors from the refined atomic models are plotted in figure 4.17. In the low-temperature and room-temperature phases, each unit cell contains four formula units, and each formula unit has one Pb atom. The unit cell of the cubic phase only contains one formula unit and thus one Pb atom. The values of these dipole

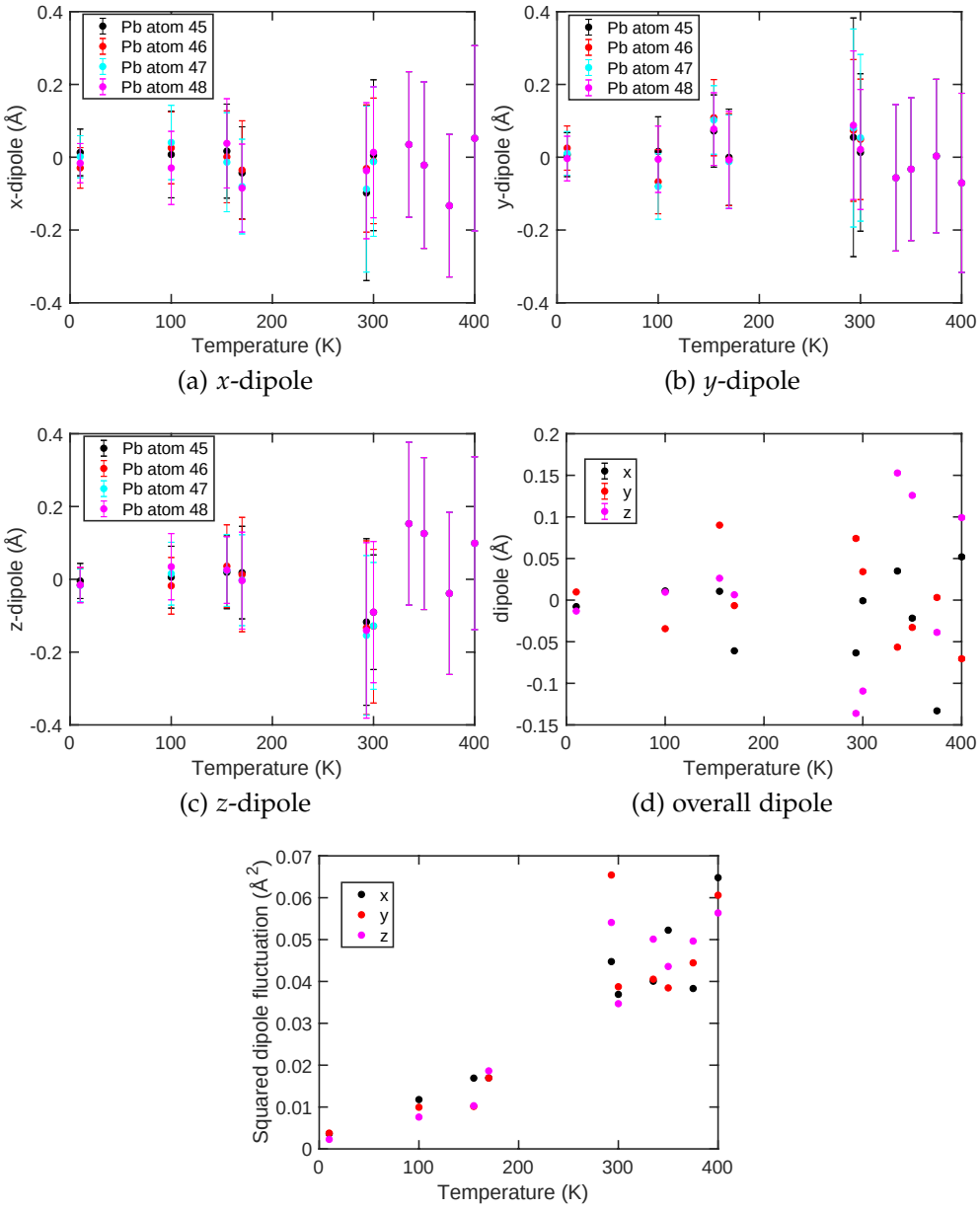

(a) x-dipole (b) y-dipole

(c) z-dipole (d) overall dipole

(e) squared dipole

Figure 4.17: Dipole analysis of the Pb–I bond. The first three figures show temperature evolution of the x-dipole, y-dipole and z-dipole, which only include the dipole moments along the three crystallographic axes.

moments are almost temperature-independent and oscillate around zero, but the standard deviation becomes bigger upon heating. The six Pb–I dipole vectors should be cancelled out due to symmetry, but the dipole moments are always fluctuating and give rise to the transient dipole moments. Figure 4.17

d reveals the average dipole moments. At low temperatures down to 10 K, the average dipole moments are close to zero as expected in three directions. As the temperature goes up, the average dipole moments are away from zero and more dispersed with the amplitude. Figure 4.17 e shows the squared value of fluctuation of the dipole moments, which are calculated from the deviation values of the dipoles from the average value:

$$\mu_{\text{fluc}} = \langle \mu_i \mu_j \rangle - \langle \mu_i \rangle \langle \mu_j \rangle \tag{4.6}$$

The squared dipole fluctuation increases linearly on heating, and the deviation from this trend at 320 K is because the cubic model at this temperature is insufficient to describe the two-phase behaviour. The magnitude of the squared fluctuations is around 10^{-2} Å^{-2} across the temperature ranges.

Compare this to the perovskite $BiFeO_3$. In this material, we can calculate pseudo-dipole moments from either the BiO_{12} or FeO_6 coordination polyhedra. The magnitude of the squared fluctuations are similar and about 10^{-2} Å^{-2} without much difference between the two sorts of dipoles [127]. However, this value is bigger than the OCu_4 in CuO, which is one order of magnitude lower at 10^{-3} Å^{-2} [128]. CuO is quite rigid and the hybrid perovskite $MAPbI_3$ is more flexible than CuO.

4.5 Order parameter analysis

4.5.1 Strain analysis

Order parameters are difficult to measure directly in most cases, but they are of great importance in explaining phase transitions. Spontaneous strains are characterised as secondary order parameters for perovskites, which do not break as many symmetry elements as primary order parameters do [129].

The strains in perovskites have been elucidated by Carpenter *et al.* [130]. Linear strains ϵ_1, ϵ_2 and ϵ_3 are defined alongs the crystallographic a, b and c axes. ϵ_a is the volume strain and ϵ_{tz} represent the shear strain normal to the tetragonal axis, and $\epsilon_1 = \epsilon_2$ in the tetragonal phase based on symmetry analysis. The cubic–tetragonal phase transition involves an elongation along the [001] axis and a uniform shrinkage in the perpendicular plane. The basic strains in the tetragonal phase are

$$\epsilon_1 = \epsilon_2 = \frac{a - \sqrt{2}a_0}{\sqrt{2}a_0} \quad ; \quad \epsilon_3 = \frac{c - 2a_0}{2a_0} \tag{4.7}$$

and

$$\epsilon_1 = \frac{a - \sqrt{2}a_0}{\sqrt{2}a_0} \quad ; \quad \epsilon_2 = \frac{b - 2a_0}{2a_0} \quad ; \quad \epsilon_3 = \frac{c - \sqrt{2}a_0}{\sqrt{2}a_0} \tag{4.8}$$

for the orthorhombic phase. The term a_0 is the extrapolation of the cubic lattice parameter to low temperature, and can be approximated to high accuracy as $a_0 = (\sqrt{2}a + c/2)/3$ in the temperature range of the tetragonal phase, as in figure 4.3. The relevant symmetry-adapted strain components are

$$\epsilon_a = \epsilon_1 + \epsilon_2 + \epsilon_3 \quad ; \quad \epsilon_{tz} = \frac{1}{\sqrt{3}}(2\epsilon_3 - \epsilon_1 - \epsilon_2) \tag{4.9}$$

in the tetragonal phase and they are defined as

$$\epsilon_a = \epsilon_1 + \epsilon_2 + \epsilon_3 \quad ; \quad \epsilon_{ty} = \frac{1}{\sqrt{3}}(2\epsilon_2 - \epsilon_1 - \epsilon_3) \quad ; \quad \epsilon_5 = \epsilon_1 - \epsilon_3 \tag{4.10}$$

in the orthorhombic phase. Here ϵ_5 is the shear strain in the xz plane. It is found that $\epsilon_{tz} \gg \epsilon_a$, the typical situation since ϵ_a is the symmetry-preserving strain of the cubic phase, whereas ϵ_{tz} lowers the symmetry.

The temperature dependence of the strains is given in figure 4.18. The magnitude of the tetragonal strain reaches as high as 0.025 for the $MAPbI_3$ case, and is only about 0.005 in inorganic perovskites, such as $CaTiO_3$ and $SrTiO_3$ [131]. In fact, ϵ_a has a value very close to zero within the accuracy of the data. e_{ty} and e_{tz} are the shear strains in the orthorhombic and tetragonal

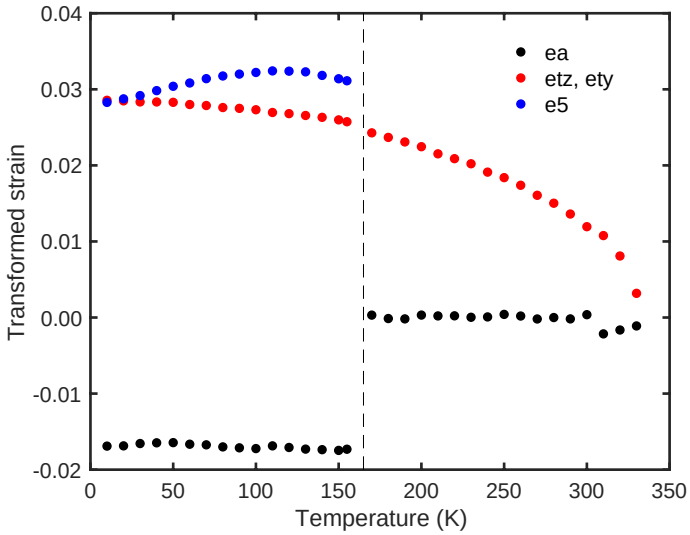

Figure 4.18: Spontaneous strains for the orthorhombic and tetragonal phase, obtained from the Rietveld-refined lattice parameters.

phase, respectively. These two strains vary more or less continuously across the phase transition, and e_{tz} is proportional to the square of the order parameter, which will be discussed further in section 4.5.2. The shear strain e_5 increases and then decreases when decreasing the temperature, which is not a squared relationship with the order parameter. The same behaviour of e_5 has been shown in another paper as well as [131], but the author could not identify the reason behind the phenomenon.

4.5.2 Phase transition

The temperature dependence of the cubic–tetragonal phase transition has been studied previously [119]. The authors analysed the tetragonal strain in terms of a critical exponent formalism, fitting a function of the form $(T_c - T)^{\beta}$, finding $\beta = 0.27 \pm 0.01$. The tetragonal structure $I4/mcm$ is a subgroup of the parent cubic structure $Pm\bar{3}m$, and the transition could be second-order according to Landau theory. However, the transition is slightly first-order as seen in small discontinuities in the properties at the transition point, some co-existence of the tetragonal and cubic phase, and in the existence of a small latent heat [132,

133]. Latent heat is a strong indication of a first-order transition, where a spike is seen in the heat capacity measurement in the vicinity of the phase transition. It would be more appropriate to do analysis in terms of a Landau free energy function, as in equation 4.12 with the negative quartic term and positive sixth-order term, anticipating that the value of β close to $1/4$ is consistent with the phase transition being nearly tricritical through the fourth-order term having a small coefficient.

The symmetry of the orthorhombic phase is not a subgroup of that of the tetragonal phase, and thus there is not a direct link between the two phases. The tetragonal–cubic phase transition being second order can be ruled out. Instead the orthorhombic phase should be seen as a distortion of the cubic phase, but in this case (unlike the tetragonal phase) the transition involves complete ordering of the orientations of the MA cations as well as involving rotations of the PbI_6 octahedra. It should be noted the orthorhombic phase is a subgroup of the cubic phase.

Octahedral tilting is common in many perovskites, and the tilt angles have been quantified as order parameters across the phase transitions. According to Landau theory, requirement for order parameters is that they need to drop to zero as approaching the phase transition either continuously or discontinuously. The phase transition is classified as first-order if the order parameter Q falls to zero discontinuously near the transition point. The transition is second-order or tricritical when $\beta = 1/2$ or $1/4$, by fitting

$$Q \propto |T_c - T|^{\beta} \tag{4.11}$$

The appropriate Landau free energy function for the first-order phase transition has the form

$$F = \frac{1}{2}a(T - T_0)Q^2 - \frac{1}{4}bQ^4 + \frac{1}{6}cQ^6 \tag{4.12}$$

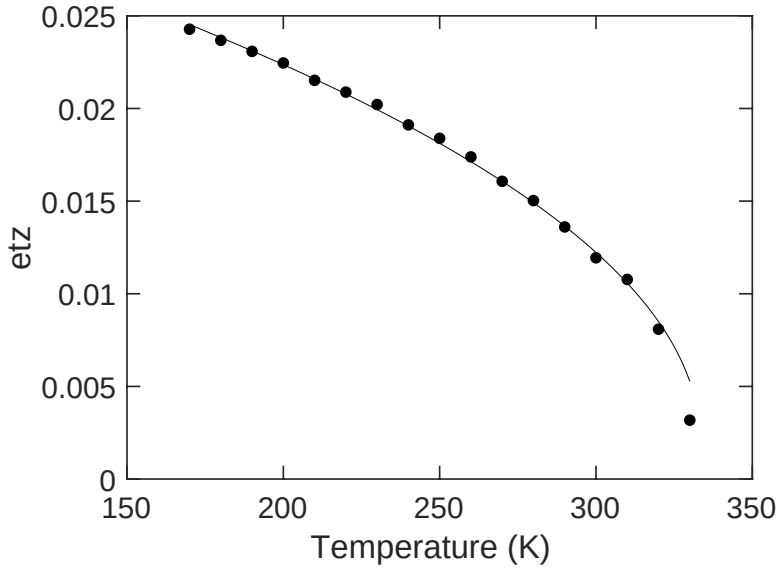

Figure 4.19: Fitted temperature-dependence of the strain ϵ_{tz} fitted from the minimum of a first-order Landau free energy function.

It should be noted a, $b$and c are not the lattice parameters. Minimising the free energy F with respect to order parameter Q, $\frac{\partial F}{\partial Q} = 0$ we get

$$Q^2 = \frac{b + \sqrt{b^2 - 4ac(T - T_0)}}{2c} \tag{4.13}$$

with the transition occurring at temperature

$$T_c = T_0 + \frac{3b^2}{16ac} \tag{4.14}$$

and with a discontinuous change in the order parameter of $\Delta Q^2 = \pm 3b/4c$ at temperature T_c.

The starting values of T_c and ΔQ^2 were assumed before the fitting the the strains. Writing $a' = a/c$ and $b' = b/2c$, we have for any temperature T_i

$$\chi_i = \left(Q_i^2 - b'\right)^2 - b'^2 + a'(T_i - T_0) \tag{4.15}$$

a' and b' were adjusted to minimise the function

$$\chi^2 = \sum_i \chi_i^2 \tag{4.16}$$

The fitting started from a fixed value of $b/2c$, which was chosen to reproduce the jump in Q^2 at the phase transition. The strain ϵ_{tz} was used as an accurate

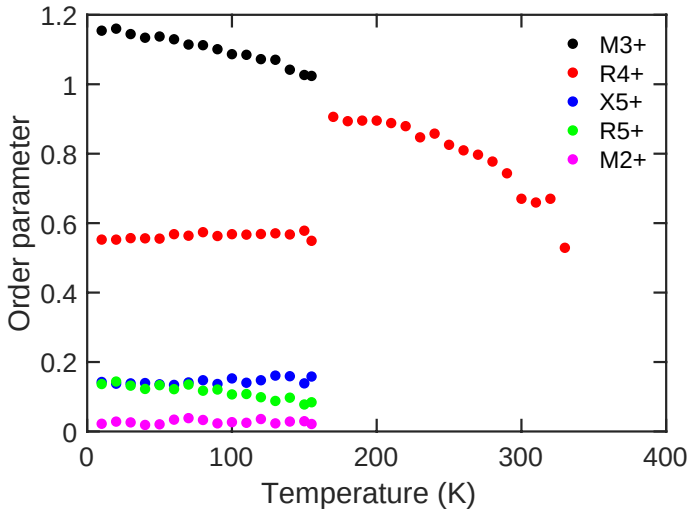

Figure 4.20: Temperature-dependence of the symmetry-adapted deformations associated with the two phase transitions in methylammonium lead iodide, labelled according to their irreducible representations of the cubic $Pm\bar{3}m$ space group.

measurement of Q^2. Because of the 10 K interval in measurements steps it is not realistic to obtain a precise estimate of T_c or ΔQ^2. The fitted measurement of e_{tz} is shown in Figure 4.19. From the fit the obtained value via equation 4.14 of $T_c - T_0$ is as small as 1.1 K (fitted value of T_0 is 331.8 K), which is (from equation 4.14) essentially pointing out that the parameter b in equation 4.12 is small and hence the phase transition is nearly tricritical, as suggested previously.

Although organic-inorganic perovskites are more complicated in terms of the molecule in the cavity, the distortion mode analysis can still be performed and compared with the inorganic oxide perovskites. Moreover, the distortion of the lead-halide framework is separate from the cation order disorder motion. The atomic displacements of the distorted structures can be described by the linear combination of different normal modes. The full crystal symmetry of the space group transforms each normal mode to a unique irreducible representation (irrep). The dimensionality of the irreps corresponds to the number of components of the order parameter in a phase transition.

IR	Space group	Pb	I1	I2
	$Pm\bar{3}m$	$(1/2, 0, 0)$	$(1/2, 1/4, 0)$	$(1/4, 0, 1/4)$
	$Pnma$	$(1/2, 0, 0)$	$(1/2-\delta, 1/4, -\delta')$	$(1/4-\gamma, \eta, 1/4-\gamma')$
M_3^+	$P4/mbm$	$(1/2, 0, 0)$	$(1/2, 1/4, 0)$	$(1/4-\gamma, 0, 1/4-\gamma)$
R_4^+	$Imma$	$(1/2, 0, 0)$	$(1/2, 1/4, -2\delta)$	$(1/4, \delta, 1/4)$
X_5^+	$Cmcm$	$(1/2, 0, 0)$	$(1/2-\delta, 1/4, 0)$	$(1/4, 0, 1/4)$
R_5^+	$Imma$	$(1/2, 0, 0)$	$(1/2, 1/4, -2\delta)$	$(1/4, -\delta, 1/4)$
M_2^+	$P4/mbm$	$(1/2, 0, 0)$	$(1/2, 1/4, 0)$	$(1/4+\gamma, 0, 1/4-\gamma)$

Table 4.6: Symmetry mode analysis of possible distortions that contribute to the phase transition from space group $Pm\bar{3}m$ to $Pnma$.

Here I use AMPLIMODES [134, 135] to calculate the amplitudes of each distortion mode. The reference high-symmetry phase is the cubic phase $Pm\bar{3}m$, and the other lower-symmetry phases (tetragonal $I4/mcm$ and orthorhombic $Pnma$) were compared with the reference phase to extract the structural distortions that connect two phases. The origin was selected as the A-cation centre. The amplitudes were normalised based on the multiplication of the unit cells as the low-symmetry tetragonal phase is body-centred unit cell, hence the primitive cells have different size.

In perovskites, we anticipate two distorted structures in the sequence of structural phases associated with two irreps $R4^+$ and $M3^+$ in the reciprocal space [131]. The amplitudes of those symmetry-adapted distortion modes are given in table 4.6 and the relationship with temperatures is also given in figure 4.20. The amplitudes of M_3^+ and R_4^+ indicate they are the most significant irreps in the two phases. In the tetragonal phase, there is only one irrep R_4^+ describing octahedral rotation. In the orthorhombic phase, however, things are more complicated and there are five irreps M_3^+, R_4^+, X_5^+, R_5^+ and M_2^+. The first is the rotation about the orthorhombic [010] axis, where adjacent layers parallel to (010) have identical rotations. The modulation corresponds to that of a phonon of wave vector $\mathbf{k} = [1/2, 0, 1/2]$, which is labelled M. This distortion leads to the expansion in [100] and [001] directions but does not double the

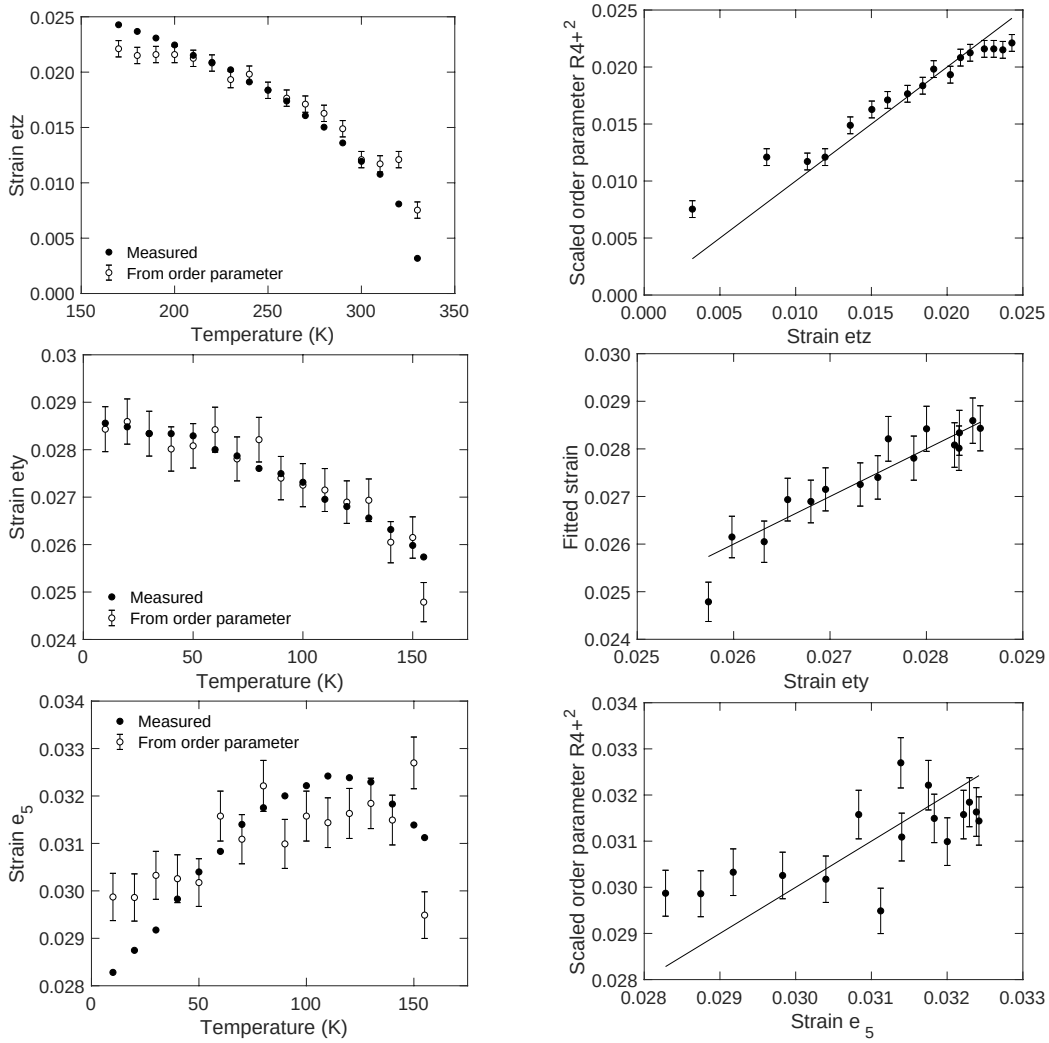

Figure 4.21: Fitted strains according to equations 4.17–4.19. The left side compares the dependence on temperature of three strains as determined by the measured lattice parameters and as fitted from the order parameters. The right side compares directly the measured strains and as constructed from the order parameters. The top two diagrams are for the tetragonal phase and the two lower pairs are for the orthorhombic phase.

periodicity in the [010]. On the other hand, the R_4^+ distortion, giving rotations in this case around both the orthorhombic [101] and [10$\bar{1}$] directions (that is, around the Pb–I bonds perpendicular to [010]), doubles the periodicity in all three directions which is described conventionally, as here, through a rotation of axes and designation of the I-centring of the unit cell. Both M_3^+ and R_4^+ give the distortion that is described in Glazer notation as $a^-b^+a^-$.

According to Carpenter, we have relationships between strain and amplitudes based on only the M_3^+ and R_4^+ modes. They are derived using the equilibrium conditions of the Landau free energy that the crystal must be stress-free. Writing the order parameters corresponding to the two modes as $Q(M_3^+)$ and $Q(R_4^+)$, we expect the following relationships in the $I4/mcm$ phase,

$$\epsilon_{tz} \propto Q^2(R_4^+) \tag{4.17}$$

also, the following relationships in the $Pnma$ phase,

$$\epsilon_{ty} \propto a_3 Q^2(M_3^+) - a_4 Q^2(R_4^+) \tag{4.18}$$

$$\epsilon_5 \propto Q^2(R_4^+) \tag{4.19}$$

Figure 4.21 demonstrates the extent to which the data are consistent with these relationships. The two strains ϵ_{tz} and ϵ_{ty} both have temperature-dependence typical of a phase transition, as do the temperature-dependences of the main rotation angles, namely $Q(R_4^+)$ in the tetragonal phase and $Q(M_3^+)$ in the orthorhombic phase. Equation 4.17 is seen to be reasonably-well reproduced by the data in Figure 4.21. Interestingly a plot of ϵ_{ty} and $Q(M_3^+)$ in the orthorhombic phase appears to present a good linear relationship, which is not consistent with the symmetry constraints. Instead the combination of both $Q(M_3^+)$ and $Q(R_4^+)$ as indicated in equation 4.18 does reproduce the relationship with ϵ_{ty} reasonably well, as seen in Figure 4.21. Moreover, the temperature dependence of both ϵ_5 and $Q(R_4^+)$ in the orthorhombic phase do not show the more-normal continuous increase upon cooling. This is seen most strikingly in the higher-precision strain ϵ_5 data, but from Figure 4.21, we can conclude that the behaviour of the order parameter is consistent with the strain data. Based on the analysis here so far, such an unusual dependence on temperature is not explicable. This analysis has not taken account of the two order parameters that lead to deformation of the PbI_6 octahedra.

4.6 Summary

Previous studies have already shown that the MA molecule possesses an orientational degree of freedom at high temperatures, but it is it is often an impossible task to identify the distributions of orientations with diffraction techniques. In this study, the configurations of $MAPbI_3$ were modelled guided by the neutron scattering data. By using symmetry-adapted functions, the C–N bond orientational distribution functions were directly calculated from the RMC atomic configurations and the Kubic harmonics. The distributions of molecular orientations indicate no preferred orientations, forming an isotropic shape in the high-temperature cubic phase. In the intermediate-temperature tetragonal phase, the molecular orientations were found to be quite disordered at the high-temperature end and gradual ordering in the (110) planes at angles of around $\pm 20^{\circ}$ to the (001) planes on cooling. Fully ordered C–N bonds were observed in the orthorhombic phase, with merely some thermal vibrations present.

Octahedral rigidity was evaluated as a function of temperature and compared with the inorganic perovskite $CsPbI_3$. The fraction of the bending of Pb–I–Pb linear angles was approximately the same, about 52% in the total motion of the octahedra. Surprisingly unlike $CsPbI_3$, the percentage of stretching motion is more than that of the PbI_6 whole-body rotation in the cubic phase, reflecting the higher-energy required component (stretching) was prevailent over the octahedral rotation component. The Pb–I bond was well fitted to the Morse potential, which describes the vibrational energy being anharmonic. The anharmonic behaviour of the Pb–I bonds were shown to be less than seen in $CsPbI_3$, and the vibrational frequency is lower in $MAPbI_3$.

With Landau theory, the characteristics of the phase transitions of $MAPbI_3$ were analysed in terms of primary and secondary order parameters. Symmetry-

adapted strain analysis based on the Rietveld-refined lattice parameters was demonstrated to be consistent with the order parameters. Furthermore, the amplitude of the distortion modes representing the octahedral rotations in perovskites was demonstrated to be also consistent with the strain behaviour. The increasing and decreasing trend of the ϵ_5 on cooling was curious and incomprehensible but was found to be consistent between different datasets. It could be attributed to the strain-coupling term in the Landau energy function. The $Pm\bar{3}m \rightarrow I4/mcm$ phase transition is characterised as weakly first-order, close to tricritical behaviour. The second transition $I4/mcm \rightarrow Pnma$ has first-order character.

Chapter 5

High-pressure neutron diffraction study on $CD_3ND_3PbI_3$

5.1 Introduction

Perovskite solar cells are fabricated in a unique way to form a sandwich structure, as discussed in chapter 1. The perovskite absorber is packed between two conductive layers, materials for electron transport and hole transport respectively. The strain generated between these layers can exert pressure on the perovskite absorber and distort the crystal structure [136]. This behaviour could be utilized to optimise the optical properties of the perovskite solar cells. Similar results have been reported with $BaTiO_3$, whose polarisation is tuneable by the strain between layers [137]. Furthermore, photochromism occurs when pressurising $MAPbX_3$ (X = Cl or Br), where the colour of the solids become lighter and then opaque black [138]. Therefore, the mechanical response of the hybrid perovskites is of considerable interest to a broad community.

In-situ photoluminescence (PL) experiment measured the band-gap evolution while varying the pressure exerted on the sample [139, 140], providing insight into the relationship between structure and pressure. PL spectra have

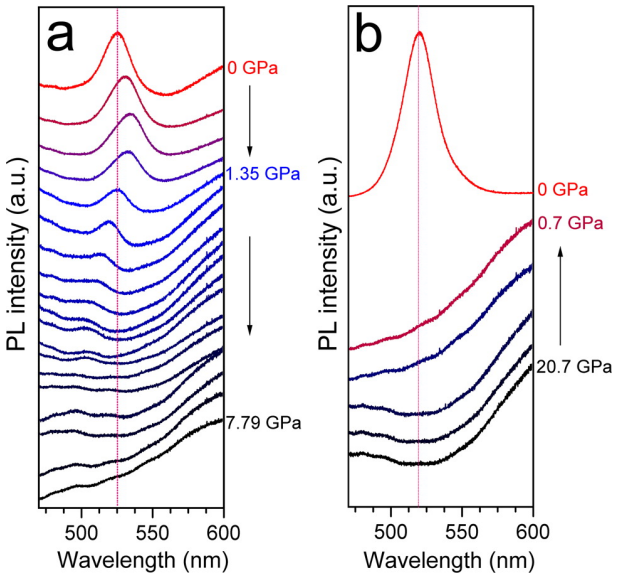

Figure 5.1: PL spectra of $MAPbBr_3$ indicate a red-shift upon compression followed by a blue-shifted trend if the material is compressed further. The graphs are adapted from [139].

been measured for $MAPbBr_3$ upon compression up to 20.7 GPa. From figure 5.1, the band-gap first experienced a gradual red-shift at 0–1 GPa, followed by a blue-shift above 1 GPa. Jiang *et al.* measured the band-gap of $MAPbI_3$ but within a considerably smaller pressure range of 0–1.95 GPa [140]. The PL spectra indicated a similar trend as in the $MAPbBr_3$ experiment. From DFT calculations, they obtained a similar trend of band-gap first decreasing to 1.62 eV from 1.67 eV and then increasing from 1.58 eV to 1.74 eV under compression. By studying both methylammonium lead bromides and lead iodides, these authors concluded the pressure-induced optical behaviour of two analogues is similar.

However, the structural response to pressure is inconsistent between these two analogues. A decade ago, Swainson *et al.* investigated the pressure-induced phase transitions of the organic-inorganic perovskite $MAPbBr_3$ through neutron diffraction [141]. The deuterated sample crystallises in the cubic space group $Pm\bar{3}m$ at ambient pressure and transforms to the $Im\bar{3}$ phase at 1 GPa. Their DFT calculation suggested the existence of the orthorhombic *Pnma* phase

ref	experiment	phaseI	phase II	phase III	amorphisation	PTM
[138]	powder	$Fmmm$	$Im\bar{3}$		2.9 GPa	helium
	X-ray	0–0.3 GPa	0.3–2.9 GPa			
[139]	powder	$I4cm$	$Imm2$		4.0 GPa	argon, silicone oil and KBr
	X-ray	0–0.3 GPa	0.3–4.0 GPa			
[140]	single-crystal	$I4/mcm$	$Im\bar{3}$	$Immm$	3.5 GPa	
	X-ray	0–0.3 GPa	0.3–2.7 GPa	>2.7 GPa		
[143]	powder	$I4/mcm$	$Imm2$		3.65 GPa	helium
	X-ray	0–0.26 GPa	0.26–3.65 GPa			

Table 5.1: Pressure-induced phase transitions of $MAPbI_3$ from literature.

at higher pressures without experimental evidence. Subsequently the predicted phase was successfully identified by Wang *et al.* at 1.8 GPa using powder X-ray diffraction [142].

However, the pressure-induced phase transition of $MAPbI_3$ is not as clear as the scenario of $MAPbBr_3$ [142]. As characterised in chapter 4, $MAPbI_3$ adopts the tetragonal polymorph with the space group $I4/mcm$ at ambient temperature. If we pressurise the hybrid perovskite, we might expect it to transform to the low-temperature orthorhombic $Pnma$ phase. To my best knowledge, there have been no reports on the tetragonal–orthorhombic phase transition found under compression.

Single crystal and powder X-ray diffraction using diamond-anvil cells (DAC) have been performed on $MAPbI_3$ [138]. The structural behaviour from both experiments are similar in term of phase evolution, a high pressure phase was observed except the transition point of single-crystal (0.6 GPa) is higher than the powder sample (0.3 GPa). Rather than adopting the ambient temperature tetragonal phase $I4/mcm$ as the starting point, these authors refined the ambient pressure structure as a tetragonal-like orthorhombic structure with space group $Fmmm$, and the high-pressure phase transformed to a cubic structure $Im\bar{3}$. Another high-pressure X-ray diffraction reported a structural transformation from the $I4/mcm$ tetragonal phase to the $Im\bar{3}$ cubic phase at 0.4 GPa, and then to the orthorhombic phase $Immm$ at 2.7 GPa before amorphisation at 3.5 GPa [140]. Capitani [143] and Wang [139] have identified only one

phase transition near 0.3 GPa, with the ambient tetragonal phase transformed into the orthorhombic *Imm*2 phase. However, they did not report details about this *Imm*2 structure other than for lattice parameters. Pressure-induced phase transitions of $MAPbI_3$ from literature are shown in table 5.1.

Notably, the impact of PTM on pressure-induced structural behaviour is rather significant [144–147]. For example, all the hybrid perovskites $MAPbX_3$ eventually transform into the amorphous phase under pressure [146], but the transition pressure is affected by choice of PTM. Moreover, the medium may itself be incorporated into the material under investigation. For instance, an X-ray diffraction study has showed that the noble gases Ar and Ne, used as PTMs, are gradually incorporated into the $MAPbI_3$ structure as the pressure increases. From a previous X-ray diffraction study, the PTMs (noble gas, Ar and Ne) have been progressively incorporated into $MAPbI_3$ when increasing the pressure [144]. This possibility adds to the complexity of an explicit understanding of the pressure-induced behaviour of this material.

In summary, most previous high-pressure diffraction experiments on $MAPbI_3$ were performed with X-rays and different transmitting media. Instead, I used neutron powder diffraction to study the hybrid organic-inorganic perovskite $MAPbI_3$. The advantages of neutrons over X-rays have been elucidated in section 2.2, especially when the material contains light atoms. Two PTMs will be used to draw comparison concerning the structural evolution.

5.2 Experimental

5.2.1 Neutron diffraction experiment

The same powder sample of $MAPbI_3$ as used previously (chapter 4) was used here. Neutron high-pressure diffraction experiments were performed on the

PEARL instrument at the ISIS neutron facility. PEARL is a high pressure neutron powder diffractometer for *in situ* experiments, as discussed in section 2.4. Datasets were collected on the 90° bank using a Paris-Edinburgh press [84]. The sample was held in a Ti-Zr gasket with a toroidal profile. The gasket is pressed by two opposed anvils made from zirconia-toughened alumina (ZTA), which produces a lower background compared with other types of anvils. That is because ZTA has a smaller absorption coefficient than the standard choice of tungsten carbide. The anvils also have a toroidal profile to match with the gasket, preventing the overflow of the central parts of the gaskets when being pressed. This essentially guarantees the increasing of the pressure.

Two different PTMs were used, perdeuterated 4:1 methanol/ethanol and FC84/87 fluorinert. The first experiment was with methanol/ethanol and pressed at the applied loads of tonnes of 5 to 20 with a step of 2.5 tonnes, then decompressed from 20 to 2.5 with a step of 2.5 tonnes. The other experiment with fluorinert as PTM, loads of 5, 5.5, 6, 6.5, 7, 8, 9, 10,11, 12, 13, 14, 15, 16, 16.5, 17.5, 18.5, 19.5, 20.5, 21.5 and 25 tonnes were used. Note that these forces refer to the pressure put into the system rather than exerted on the sample. A small piece of lead wire was included in the cell as the marker to extract the exact pressure at the sample position. By knowing precisely the equation of state of lead, one is able to refine the lattice parameters of the lead each time after the pressure changes, and the absolute sample pressure is obtained from the equation of state. Data corrections were performed by focussing and summing the raw data from individual detectors, and normalising with respect to the incident beam intensity before correction on the detector efficiency with the MANTID software [84, 110].

5.2.2 Effects of PTM

The majority of the pressure experiments are performed with PTM present [138, 139, 144–147], but some are performed without any hydrostatic medium [140]. If the pressure is not hydrostatic, the structure evolution on pressurisation could vary [136]. The inhomogeneity caused by pressure-caused strain on the sample may pose a problem in data analysis.

Perdeuterated methanol-ethanol (4:1) is the most common PTM in high-pressure experiments. This allows the hydrostatic pressure up to 10.5 GPa [148]. The substantial background from hydrogen is prevented by deuterated compounds. It should be noted the $CD_3ND_3PbI_3$ contains methylammonium ion, which is dissolvable in polar solvents like methanol. Hence, the pressure-induced behaviour was compared with the one with fluorinert as PTM.

The other PTM is FC84/87 fluorinert. Unfortunately, this is not available in deuterated form and therefore inevitably introduces some incoherent background. The pressure can go up to 2.3 GPa for the FC84/87 fluorinert (1:1) [149]. The mix of two similar liquids has been demonstrated to increase this pressure limit.

5.3 Crystal structure refinement

Rietveld refinement was performed on all the diffraction data. Some background peaks were present from the ZTA anvils and lead, and therefore were fitted with additional phases [150]. Two phases for the ZTA anvils (space group $R\bar{3}c$ and $P42/nmc$) and one phase for the pressure calibrator lead (space group $Fm\bar{3}m$). The background was described by an eight-term Chebyshev function. In total, there are four phases in the fitting cycle, one from the sample while the others are the contaminant phases, so the scale factor of each phase was

allowed to be refined. The lattice parameters of the sample phase, along with the lattice parameters from additional phases, were refined simultaneously. After the lattice parameters had converged, the peak profile was also allowed to refine. The pressure was calculated with errors from the error bar of lead's refined lattice constant. Those additional peaks were labelled with triangle markers in the diffraction patterns, and the rest of the peaks belong to the sample.

FC84/87 fluorinert The diffraction patterns collected with fluorinert plotted in figure 5.2. The first batch of data is the sample with FC84/87 fluorinert as the medium, with compression process only. Unlike cooling in the experiment as a function of temperature, the decompression process is difficult as the peak broadening becomes substantial as the load is reduced, and exactly the same state can rarely be recovered.

From the diffraction patterns plotted in figure 5.2, we noted clear structural changes with the increasing pressure. The highest pressure achieved was at 1.515(15) GPa. The lowest pressure was 0.011(4) GPa with error and could be treated as the low-pressure phase at ambient temperature. Because the same sample was used in the previous chapter 4, the room-temperature tetragonal phase was descibed with the space group $I4/mcm$. This model was successfully fitted to the low-pressure diffraction data (phase I), and the Rietveld refinement result is shown in figure 5.3 a.

Apart from two existing D atoms, two H atoms were added to the tetragonal model in the ambient-pressure data to confirm the deuteration degree. These atoms were forced to occupy the identical position as D atoms by constraints, and the occupancy of two atoms was refined as discussed in chapter 4. The reduced χ^2 increased to 0.6370 from 0.6317 with the assumption that CD_3 is partly deuterated, while it reduced to 0.6294 from 0.6317 assuming that ND_3 is partly deuterated. Thus, the decision is made by only refining the occupancy

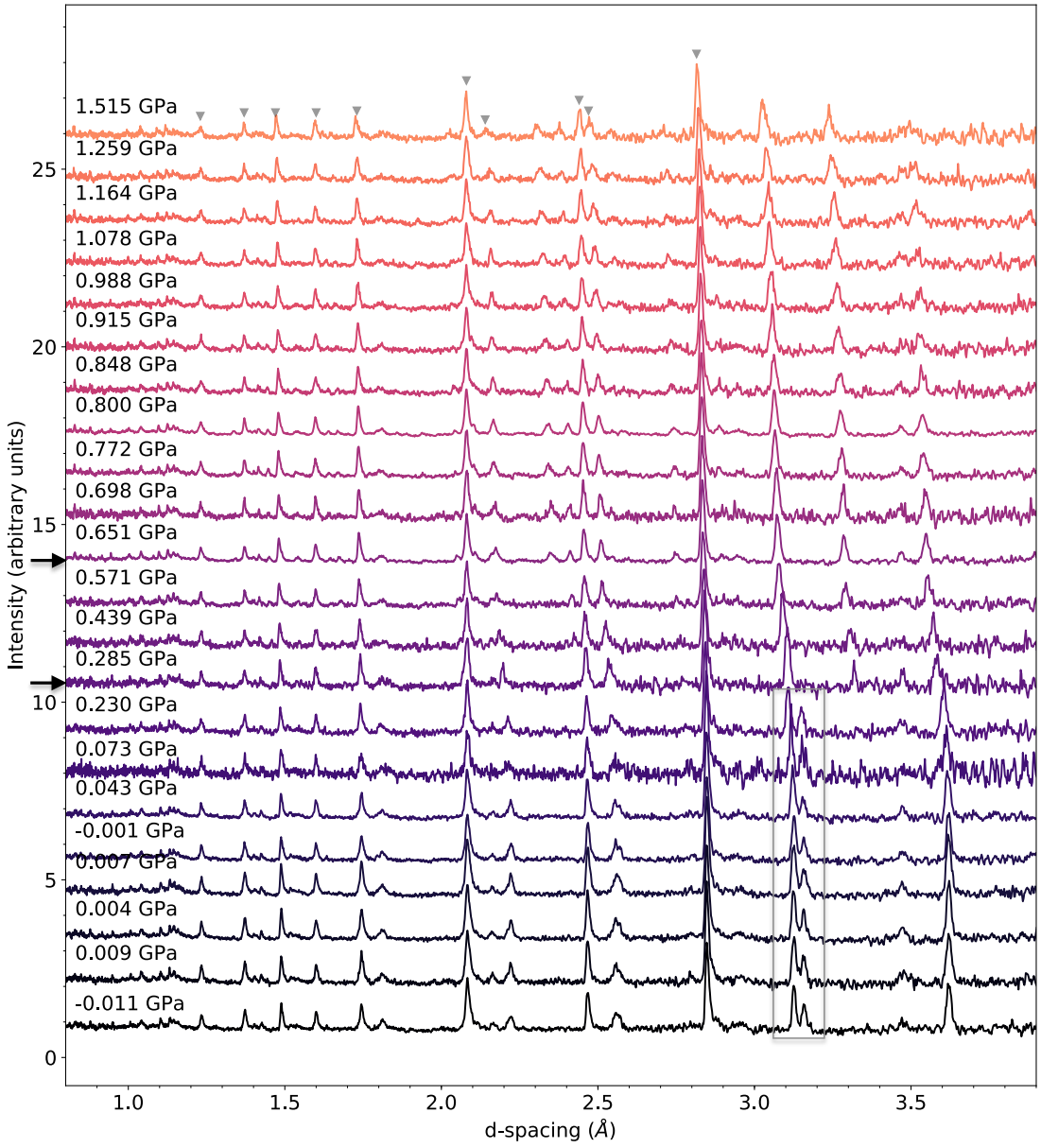

Figure 5.2: The diffraction patterns of $MAPbI_3$ upon compression with the PTM as FC84/87 fluorinert. The dark arrows indicate the structural changes in the diffraction data. The square region includes two Bragg peaks from the main sample peaks, and only one peak exist after the first phase transition.

of H atoms bonded to N atoms, in agreement with the previous refinement in chapter 4. The ratio of H/D atoms belonged to the ND_3 group was set as 5% as the total amount of D, with the occupancy of H being 0.047(9). This is slightly different from the refined percentage of H atoms as in chapter 4, where it was

set to be 10% as the total amount of D. Given that this diffraction experiment is performed after the experiment with methanol/ethanol, the difference may be arising from the fact that there might be some H/D exchange from the deuterated methanol/ethanol.

Rietveld refinement was performed in sequential order, and the result from the previous low pressure was copied to the next pressure data and each refinement quickly converged.

Phase I (tetragonal, $I4/mcm$) at low pressure was fitted successfully until 0.285(11) GPa, after which new peaks were observed. The diffraction pattern of the sample could no longer be fitted with the tetragonal structure with space group $I4/mcm$. Because the pressurisation process resembles the cooling process, the low-temperature orthorhombic phase with space group *Pnma* of $MAPbI_3$ was then used as the model for the intermediate-pressure data (phase II). The representative Rietveld refinement result is shown in figure 5.3 b. Two peaks at 3.12 Å(220) and 3.16 Å (004) merged to a single peak (040/202), and a new peak (221/122) started to grow at 3.34 Å. All the peaks were indexed with phase II. Between 0.285(11) and 0.651(5) GPa, the diffraction data were refined successfully with the orthorhombic *Pnma* phase.

However, two lesser peaks emerge at 2.35 and 2.93 Å when the pressure goes up. These two small peaks are persistent in the diffraction data even upon further pressurisation. Surprisingly, the diffraction pattern is adequately described by the *Pnma* model apart from these two small peaks. To solve the structure, I also tested other proposed structures from current literature, *Imm*2 and *Immm* using the Le Bail method. However, these existing structures are inadequate to describe the two observed peaks in phase III. There is ongoing work with the ab-initio structure searching on that high-pressure phase (phase III). With the current data, the solution structures are inadequate to fit the diffraction pattern. We have been awarded further beam time on

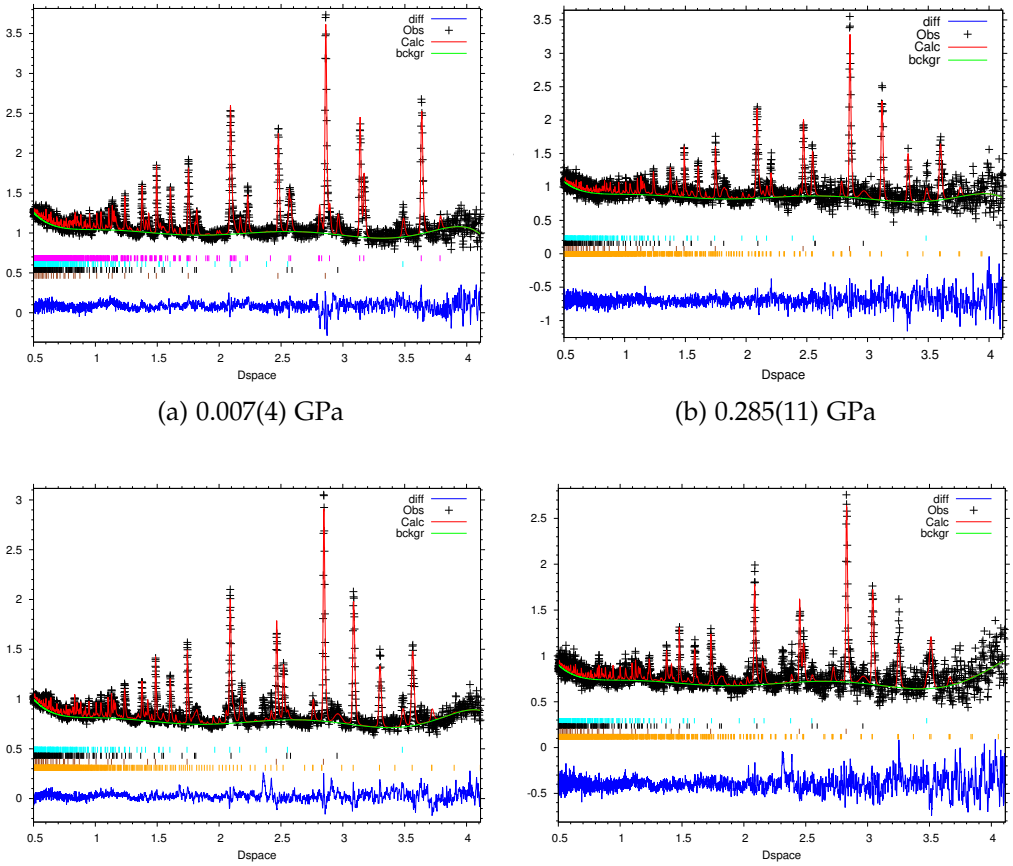

(a) 0.007(4) GPa

(b) 0.285(11) GPa

(c) 0.651(5) GPa

(d) 1.515(15) GPa

Figure 5.3: Representative fits of Rietveld refinements on $MAPbI_3$ with FC84/87 fluorinert.

the GEM instrument to explore this further; the resolution of these data will be better since GEM is a high-resolution diffractometer while PEARL is a medium-resolution diffractometer.

One possibility is the $MAPbI_3$ sample decomposed at elevated pressure, and the newly emerged peaks belong to the decomposition product. From chapter 1, $MAPbI_3$ decomposes to CH_3I, NH_3 and PbI_2 at temperatures exceeding 80 °C. The solid product PbI_2 could be left in the cell. PbI_2 crystallises in a trigonal structure with space group $P\bar{3}m1$, and the lattice parameters are $a = b = 4.6894$ Å, $c = 7.5032$ Å. However, the scale factor of the phase was refined to be negative and was not considered to be present in the data.

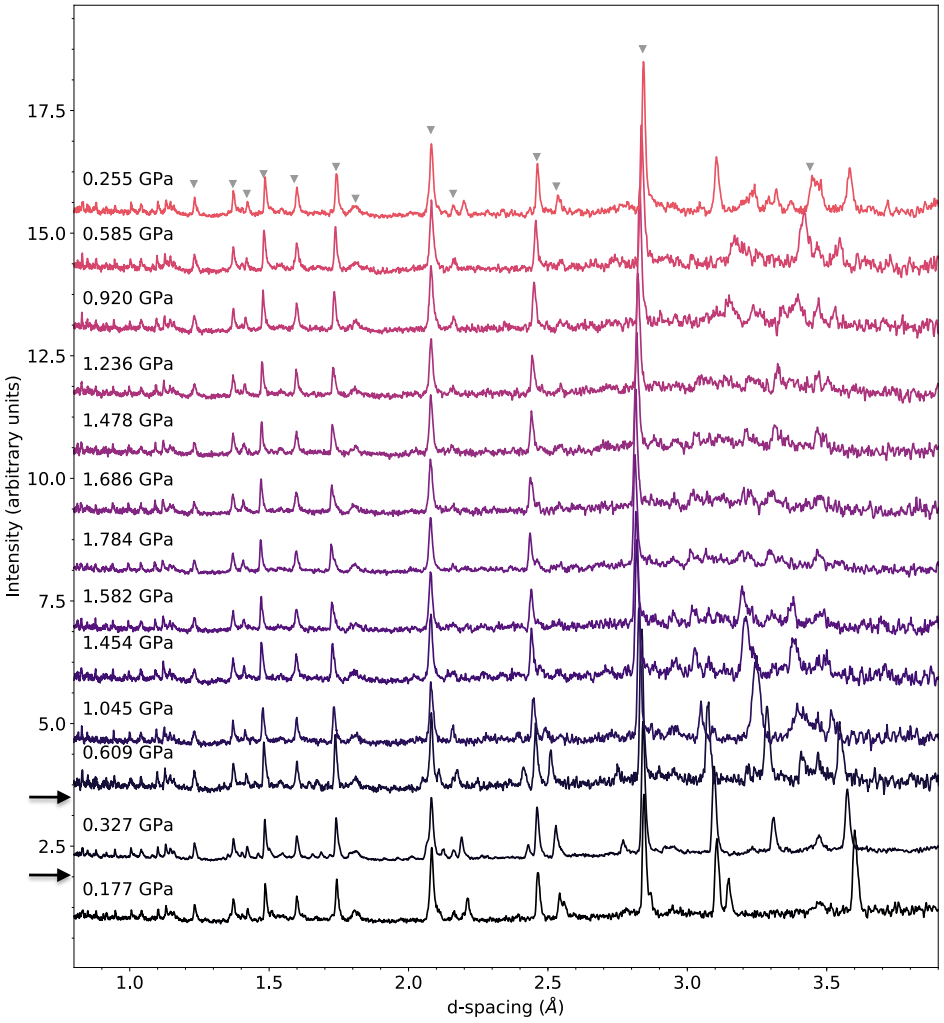

Figure 5.4: The diffraction patterns of $MAPbI_3$ upon compression and decompression with the PTM as methanol/ethanol = 4:1.

From 0.915(11) GPa, some Bragg peaks become broader in the region of 3.5 Å, indicating the onset of the amorphous structure with some loss of the crystallinity. Rietveld refinement on the highest pressure, 1.515(15) GPa data is plotted in figure 5.3. The ratio of the peak intensities of peaks at 3.1 Å (202/040) and 3.3 Å (122/221) varied from observed in the 0.651(5) GPa data, which indicates the onset of the new phase.

Methanol-ethanol (4:1) In figure 5.4, the $MAPbI_3$ sample was pressurised from ambient pressure to 1.784(6) GPa, and then decompressed until the

pressure reached 0.255(5) GPa. If we compare the evolution of the diffraction patterns with those using fluorinert, we notice the pressure-induced structural behaviour is apparently more complicated. The first phase transition occurs between two observations at 0.177(3) and 0.327(5) GPa. The transition points are in agreement with the transition points in section 5.3. The new peaks at 2.43 and 3.32 Å emerged in phase II, and the peak at 3.15 Å disappeared at 0.327(5) GPa. The second phase was fitted to the orthorhombic phase (*Pnma*) as well, and a representative fit is shown in figure 5.6 b. The new peaks were all indexed by this *Pnma* phase. The second phase transition occurred between 0.571(10) and 0.651(5) GPa when fluorinert is the medium. Here, the diffraction data at 0.609(8) GPa could not be fitted with the orthorhombic model, as in figure 5.6 c. The new peak at 3.42 Å could not be indexed, and it is explicit the phase behaviour is different in the cases with two different PTMs.

When the pressure reached 1.784(6) GPa, the diffraction patterns indicate that the sample peaks become broader, and some diffraction intensity has been lost. Again this is evidence that the sample enters the amorphous phase. The main sample peaks are very broad and almost lost in the diffraction data between 1.784(6) and 1.236(7) GPa, and Rietveld refinements were not performed on these data. After the pressure was released, some peaks were recovered, and the distinct peaks are noticeable between observations at 0.920(8) and 0.255(5) GPa. However, the ambient-pressure tetragonal phase was not completely reproduced upon pressure release as reported in other papers [138]. The peak at 3.25 Å can not be indexed on the orthorhombic structure. Furthermore, the single peak at 3.2 Å is not in agreement with the double peak at the same d-spacing presented in phase I. Rietveld refinement of the 0.255(5) GPa data after decompression is shown in figure 5.6 d.

For completeness, phase I was fitted with the proposed *Fmmm* (see table 5.1) and $I4/mcm$ structures employing the Le Bail method, and the refinements

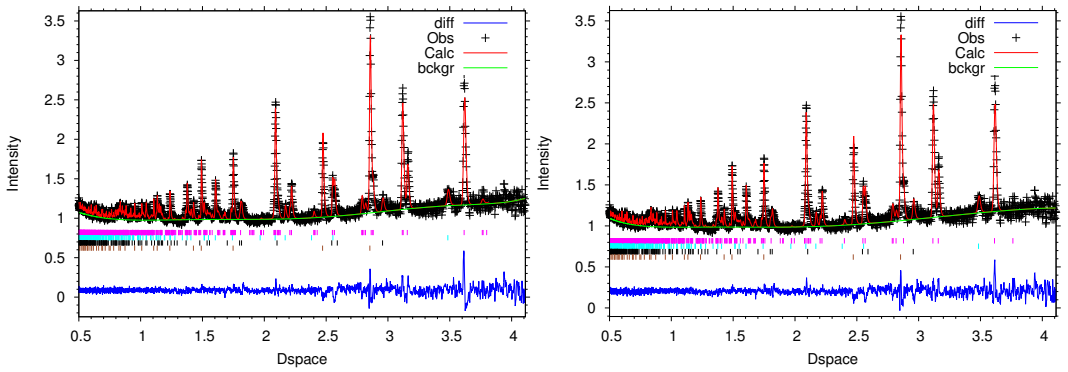

(a) $Fmmm$ (b) $I4/mcm$

Figure 5.5: Le Bail refinement of the 0.177(3) GPa diffraction data with methanol/ethanol, where the starting model is $Fmmm$ [138] and $I4/mcm$. The pink mark denotes the trial model for $MAPbI_3$ sample.

are shown in figure 5.5. The R_{wp} and R_w for $Fmmm$ are 0.0243 and 0.0304, while the R_{wp} and R_w of $I4/mcm$ are 0.0244 and 0.0294. The goodness of the fits by eye are both good and the R-factors are not considerably different. However, more peaks with zero-intensity were observed with the $Fmmm$ space group. In this sense, $Fmmm$ is not adequate for the ambient-pressure structure. Moreover, the tetragonal structure with space group $I4/mcm$ was used as the structure of phase I in Rietveld refinement, and the result is plotted in figure 5.6 a. The step of the compression determines only one pressure is available for the ambient-pressure tetragonal phase (phase I).

5.4 Cell parameters analysis

Unit-cell parameters were obtained via Rietveld refinement, and they were scaled as $a/\sqrt{2}$, $b/\sqrt{2}$ and $c/2$ to give values commensurate with the cubic phase lattice parameter, as shown in figure 5.7. There were three phases in the sequence of compression, ambient-temperature tetragonal phase (phase I), intermediate-pressure orthorhombic phase (phase II) and high-pressure phase phase III. It should be noted two small peaks could not be indexed by

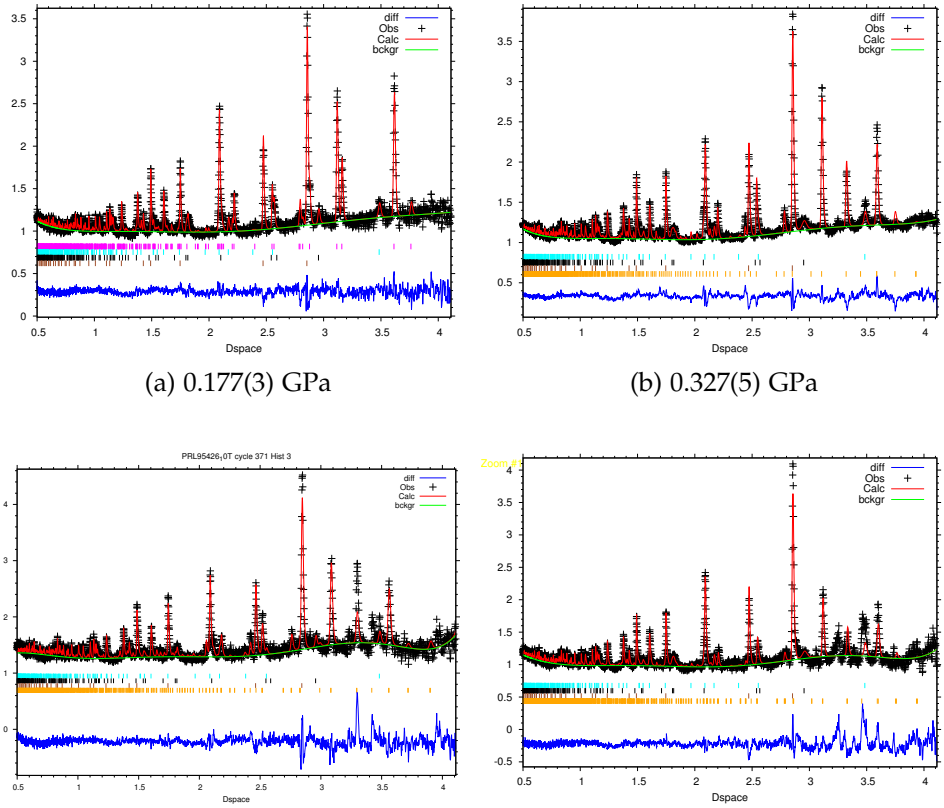

(a) 0.177(3) GPa

(b) 0.327(5) GPa

(c) 0.609(8) GPa

(d) 0.255(5) GPa (decompression)

Figure 5.6: Representative fits of Rietveld refinements on $MAPbI_3$ with PTM being methanol/ethanol.

the *Pnma* space group at high pressure. The change in length of the lattice constants implies the compressibility is similar in all directions. From chapter 4, we know the MA^+ cations are aligned in the low-temperature orthorhombic *Pnma* phase. In a similar manner, there is likely to be cation ordering coupled with contraction in cell parameters during the compression process.

5.5 Equation of state

The bulk modulus is typically defined by the isothermal equation of state

$$B = -V\left(\frac{\partial P}{\partial V}\right)_T \tag{5.1}$$

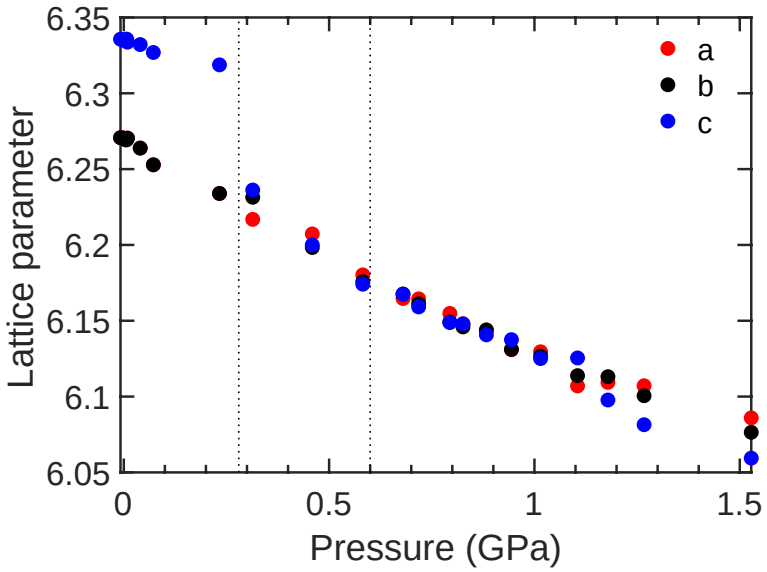

Figure 5.7: Scaled lattice parameters from Rietveld refinements against pressures.

where P and V are the applied pressure and the volume of unit cell. The bulk modulus B describes the compressibility of the solid under uniform compression. The derivative of bulk modulus B' is defined as

$$B' = \left(\frac{\partial B}{\partial P}\right)_T \tag{5.2}$$

The value of B' can be indicative of anomalous structural behaviour, for example, negative values reflect pressure-induced softening [151]. The volume-pressure data were fitted to the third-order Birch-Murnaghan equation of state [152, 153] with the web-based tool *PASCal* [154]

$$P(V) = \frac{3B_0}{2}(\eta^7 - \eta^5)[1 + \frac{3}{4}(B' - 4)(\eta^2 - 1)] \tag{5.3}$$

where $\eta = (V_0/V)^{1/3}$ and V_0 represents the ambient-pressure volume of the unit cell. Equation 5.3 becomes the second-order Birch-Murnaghan when $B' = 4$ and the second term in the bracket vanishes.

The response of the unit cell volume to pressure was fitted to the Birch-Murnaghan equations of state in the fluorinert experiment being fluorinert in figure 5.8. The Birch-Murnaghan method requires the input data from

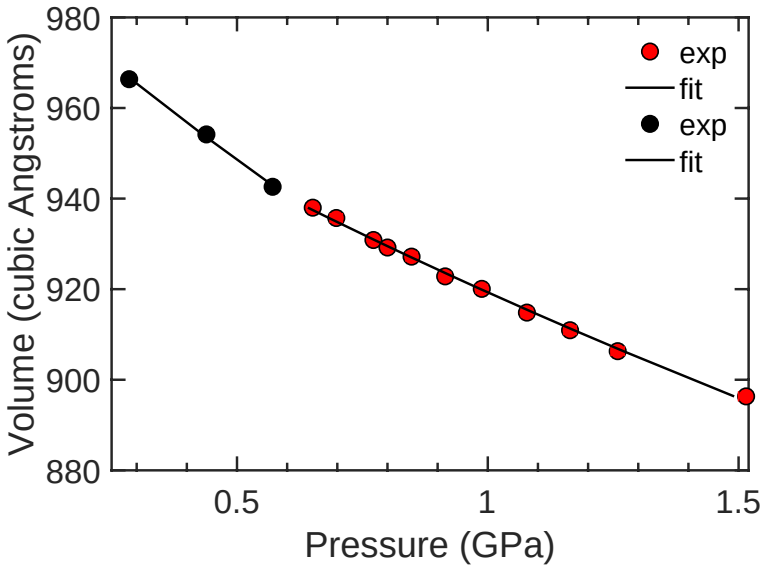

Figure 5.8: Volume-pressure variation fitted with the second-order Birch-Murnaghen equation of state for phase II and III, with the medium as fluorinert.

the same phase, so the unit cell volume of two phases was fitted with two Birch-Murnaghan equation of state, shown in figure 5.8. The fitted value of the bulk modulus, B_0 for phase III is 14.6(3) GPa, which is close to the values reported with the hydrogenous sample, 14.9(6) GPa [138]. When the volume-pressure data were fitted to the third-order Birch-Murnaghan equation of state, B' = 16(7) GPa and the fits were not improved in a significant way. This is because V_0 is not measured directly from this experiment, and the value is very sensitive to small changes in the data. The fitted values of V_0 from second- and third-order equations are remarkably different, 976(1) and 997(10) Å^3. The accuracy of the extrapolation requires the fitting to start from zero pressure, hence the error of the bulk modulus will be significant if V_0 is not accessible. For phase II, there are only three data points and two parameters to be refined, and B_0 = 9.8(5) GPa. The increasing in the bulk modulus from phase II to III indicates phase III is more compressible. Most of the collection points are near ambient pressure for phase I and will not be reported here.

5.6 Summary

Pressure-induced structural behaviour of $MAPbI_3$ was studied with two different pressure-transmitting media, methanol/ethanol and fluorinert, respectively. From the Rietveld refinement, the $I4/mcm$ tetragonal phase remains stable at ambient pressure until the first phase transition, and transforms to the orthorhombic phase $Pnma$ at 0.28 GPa for two different transmitting media. The intermediate pressure data between 0.28 GPa and 0.6 GPa were successfully fitted with the orthorhombic phase, but the structural changes diverged for two media after the pressure above 0.6 GPa. In the case of fluorinert, two small peaks emerge and stay consistent in the diffraction patterns. From the diffraction data using methanol/ethanol, some distortions of the orthorhombic phase were observed although orthorhombic or lower-symmetry structure can not be inferred from the present data. Higher-resolution diffraction data are required to elucidate the high-pressure structure properly, and we have been awarded beam time for a future neutron experiment.

Here, the tetragonal–orthorhombic phase transition is successfully reproduced even changing transmitting medium fluids. Although the choice of PTM does affect the structural changes induced by pressure, the first tetragonal–orthorhombic transition remains unaffected and occurred at 0.3 GPa for both cases and other media from literature.

Chapter 6

Local structures of inorganic perovskites $CsPbCl_3$ and $CsPbBr_3$

6.1 Introduction

As we saw in chapter 3 for $CsPbI_3$, the distribution of nearest-neighbour Pb–I bond distances is highly asymmetrical in the cubic phase, suggesting strong anharmonicity in terms of thermal motion. Other inorganic analogues of this material have also been used for photovoltaic applications, for example, $CsPbBr_3$ [23] and $CsPbCl_3$ [155]. One question is whether these two compounds exhibit similar anharmonic behaviour and if they do, to what extent they change with temperature.

$CsPbBr_3$ and $CsPbCl_3$ both have the same cubic perovskite structure, but their phase transition behaviours are different as a function of temperature. The phase transitions of $CsPbBr_3$ have been investigated using neutron diffraction method [156]. The low-temperature orthorhombic phase with space group $Pmbn$ transforms to the tetragonal structure $P4/mbm$ at 361 K, and to the high-temperature cubic $Pm\bar{3}m$ structure at 403 K. Three crystal structures are displayed in figure 6.1.

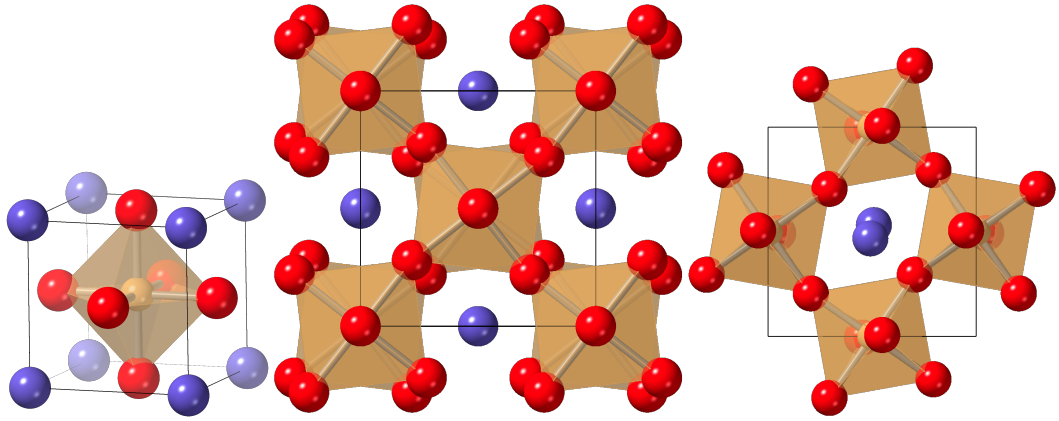

(a) $Pm\bar{3}m$ (b) $P4/mbm$ (c) $Pmbn$

Figure 6.1: Crystal structures of $CsPbBr_3$ in (a) cubic phase and (b) tetragonal phase viewed from [001] direction and (c) orthorhombic phase viewed from [001] direction.

In contrast to $CsPbBr_3$, $CsPbCl_3$ has been reported to have three phase transitions by neutron powder diffraction [157]. It prefers a monoclinic structure with space group $P2_1/m$ below 310 K, but undergoes an intermediate transition to an orthorhombic *Cmcm* structure at 310 K. At 315 K, the orthorhombic *Cmcm* structure transforms to a tetragonal $P4/mbm$ structure. The orthorhombic *Cmcm* structure then becomes cubic with space group $Pm\bar{3}m$ at 320 K. However, Fujii *et al.* did not give any cell parameters for the above structures. The working assumption is that that paper is referring to the known perovskite structures from Stokes and Hatch [158]. A recent X-ray powder diffraction study by Linaburg *et al.* has suggested the low temperature phase has orthorhombic symmetry (space group *Pnma*) rather than the monoclinic structure [159]. The cubic and orthorhombic structures are shown in figure 6.2.

It is surprising that only a few diffraction studies of these two inorganic perovskites have been reported, given the importance of their photovoltaic applications. High-resolution synchrotron X-ray total scattering was used to study the phase transitions and the anharmonicity of these two compounds.

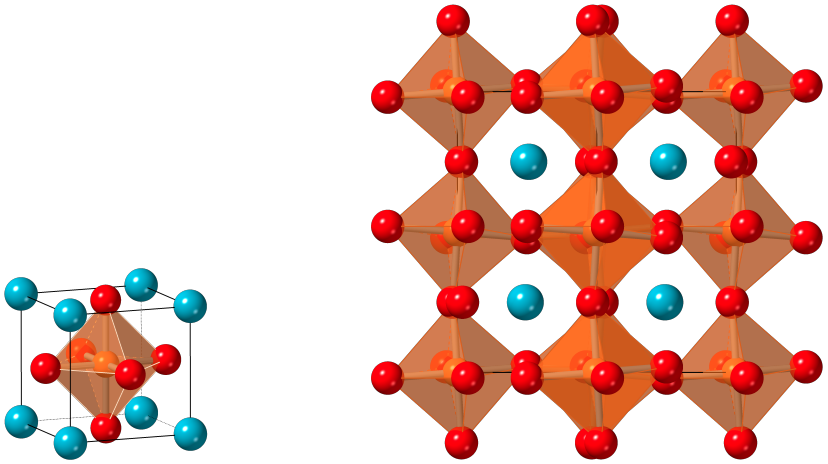

(a) $Pm\bar{3}m$ (b) $Pnma$

Figure 6.2: Crystal structures of (a) cubic phase and (b) orthorhombic phase of $CsPbCl_3$.

6.2 Experimental

6.2.1 X-ray total scattering experiment

X-ray total scattering experiment was carried out on I15-1 (XPDF), Diamond light source. Two powder samples were loaded into glass capillaries with 0.4 mm diameter, and mounted on the sample stage of the XPDF instrument. The incident wavelength is 0.161669 Å, and the measured 2θ range is between 5 to 25°. From these values, Q_{max} can be achieved as high as 32 $Å^{-1}$ for PDF data. The instrument has two large area detectors. One is for Bragg data collection while the other is for PDF data collection. The PDF detector is placed near the sample to collect weaker diffuse scattering, while the Bragg detector is further away for simultaneous collection. While the sample stage rotates, the Bragg detector is shaded by the PDF detector at specific angles. The shading problem influences the diffracted intensity of X-rays, making the peak intensity in the diffraction pattern not robust and reliable at low angles, which makes Rietveld refinement difficult.

Before measuring the sample, empty capillary and empty instrument data

collection was performed. The $CsPbCl_3$ sample was measured at temperatures 120–490 K in steps of 20 K and a finer step of 2 K near transition temperatures using a cryojet nitrogen cooler. Then the sample was measured at higher temperatures, 400–800 K in steps of 25 K with a hot blower. The $CsPbBr_3$ data were collected at temperatures of 120–500 K in steps of 20 K and a smaller step of 4 K in the vicinity of phase transitions. The powder sample was also measured at high temperatures, 400–800 K in steps of 25 K using a hot blower. The scattering data were processed using the *DAWN* program [160].

6.3 Total scattering data correction

Total scattering data correction with the Gudrun program has been discussed in chapter 2. Here, the X-ray total scattering data were corrected to get the normalised differential cross section using the GudrunX program [123].

The Q range of the differential cross section data was set to be from 0.6 to 25 $Å^{-1}$ with a step of 0.01 Å. In the final output of $D(r)$, r_{max} was specified up to 30 Å. The sample geometry and container shape were cylindrical. Corrections for attenuation and multiple scattering were performed automatically by GudrunX based on the sample dimensions.

To put the differential cross section data on an absolute scale, one has to perform a normalisation correction. In contrast to neutron PDF, X-ray PDF is the convolution of the atomic centres and distributions of the electrons represented by a broadening function [161]. The convolution theorem states that

$$f(x) = g(x) \otimes h(x) \tag{6.1a}$$

$$F(k) = G(k) \times H(K) \tag{6.1b}$$

when $F(k)$, $G(k)$ and $H(K)$ are the Fourier transforms of $f(x)$, $g(x)$ and $h(x)$,

respectively. Therefore, the differential cross section needs to be divided by a broadening function in reciprocal space before the Fourier transform to get the atomic PDF. The scattering function is corrected using either function of

$$S_a(Q) = S(Q)/\langle f(Q)\rangle^2 \tag{6.2a}$$

$$S_a(Q) = S(Q)/\langle f(Q)^2\rangle \tag{6.2b}$$

where the Fourier transform of $S_a(Q)$ will give the atomic PDF. $f(Q)$ is the Fourier transform of the electron density. Both two equations in 6.2 are merely approximations of the actual case. If two or more than two atom types are in the system, their X-ray form factors will have different Q dependencies and the average of $f^2(Q)$ over all atom types is never accurate. In this case the diffraction data were normalised to $\langle f(Q)\rangle^2$.

The crystallographic atomic density for $CsPbCl_3$ and $CsPbBr_3$ were 4.2238 and 4.8557 g cm^{-3} respectively. The inner and outer radii of the sample were 0 and 0.2 cm, while the height was 5 cm. Before the Fourier transform, any spurious structure in the low-r region was removed by using minimum radii of 2.5 and 2.7 Å for $CsPbCl_3$ and $CsPbBr_3$, respectively. As discussed in section 4.2.2, the self-scattering background in the total scattering data was removed using the top-hat function. The top-hat width was set as small as $Q_T = 2$ $Å^{-1}$ to generate a top hat function that follows the varying background in the diffraction data. The scattering function was then Fourier transformed to get the pair distribution function $D(r)$.

The corrected and normalised $D(r)$s are plotted in figure 6.3 and figure 6.4 for $CsPbBr_3$ and $CsPbCl_3$, respectively.

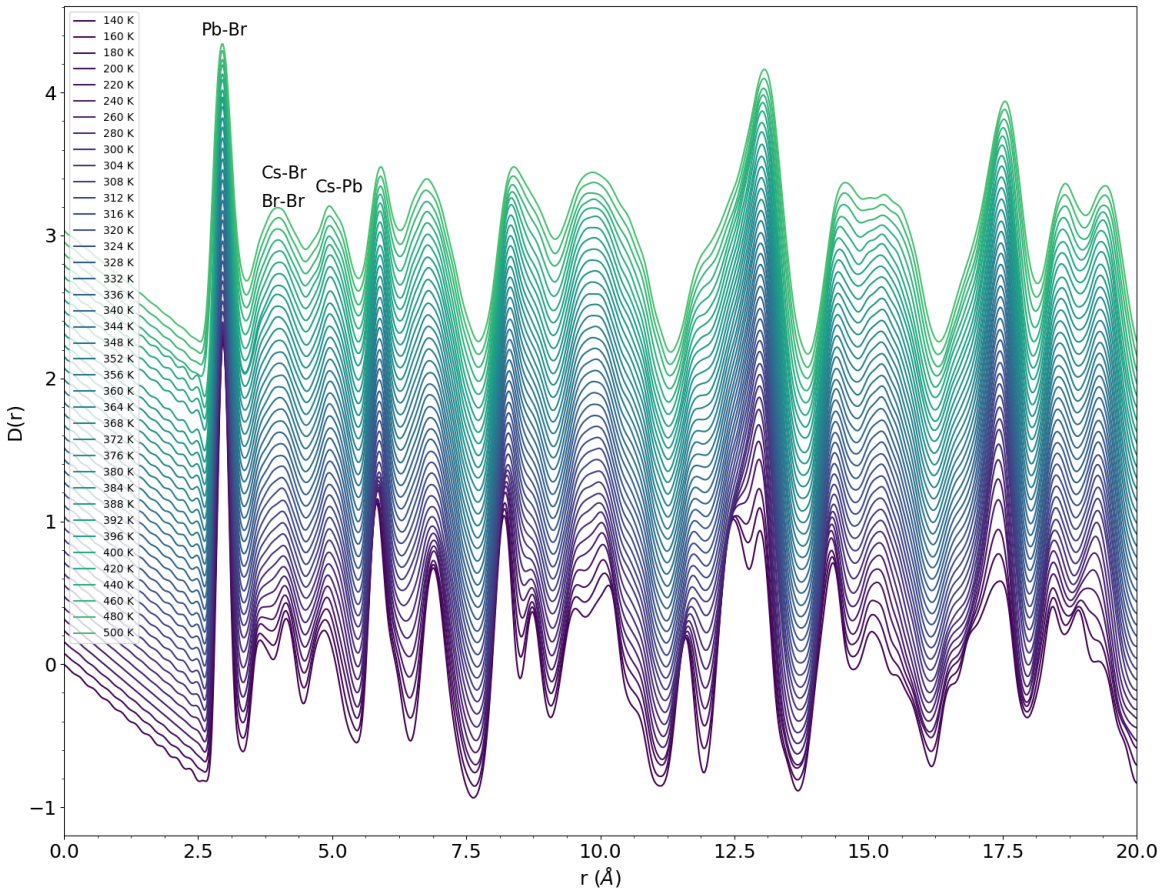

Figure 6.3: The pair distribution functions of $CsPbBr_3$ as a function of temperature.

6.4 Results and discussion

6.4.1 Phase transitions

The diffraction patterns collected with the Bragg detector are shown in figure 6.5. For clarity, the background was fitted by a Chebyschev function for the highest temperature data, and subtracted from the diffraction data for all temperatures. The horizontal axis shown here is transformed from the scattering angle 2θ using

$$\frac{1}{d^2} = \left(\frac{2\sin\theta}{\lambda}\right)^2 \tag{6.3}$$

Figure 6.5 a shows two phase transitions for the $CsPbBr_3$ sample. A phase

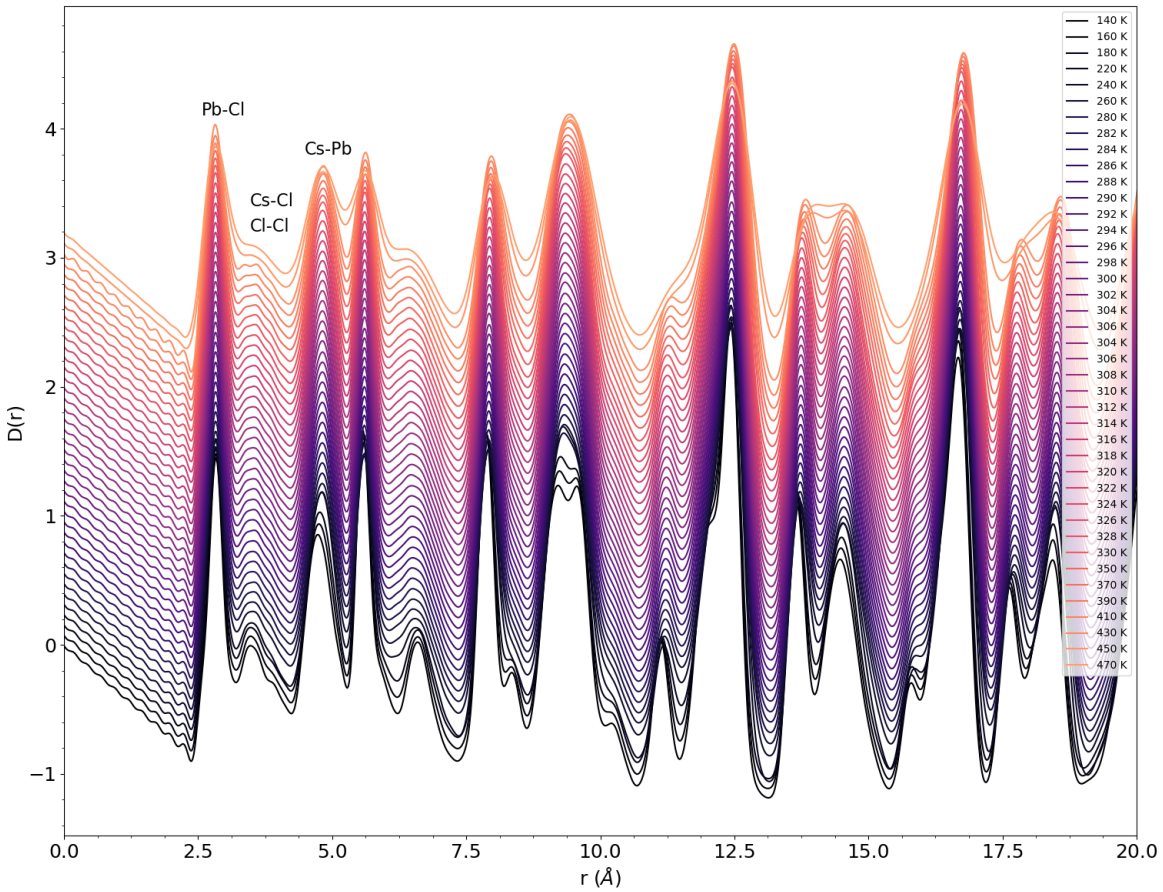

Figure 6.4: The pair distribution functions of $CsPbCl_3$ as a function of temperature.

transition occurs at 410 K, the splitting peaks appear to merge at this temperature. These reflection changes are marked using arrows. The high temperature cubic phase was confirmed to be $Pm\bar{3}m$ using Rietveld refinement. Data collected from lower angles were excluded as the diffracted intensity from this the instrument is not reliable at these angles. Rietveld refinement of the intermediate phase data was not successful. This phase transition temperature is in agreement with literature, 403 K [156]. Another phase transition reported is around 361 K [156], however, there is no phase change observed near this temperature even with small temperature steps (2 K). Instead, a phase transition was observed near 220 K. Below 220 K, many peaks split suggesting a

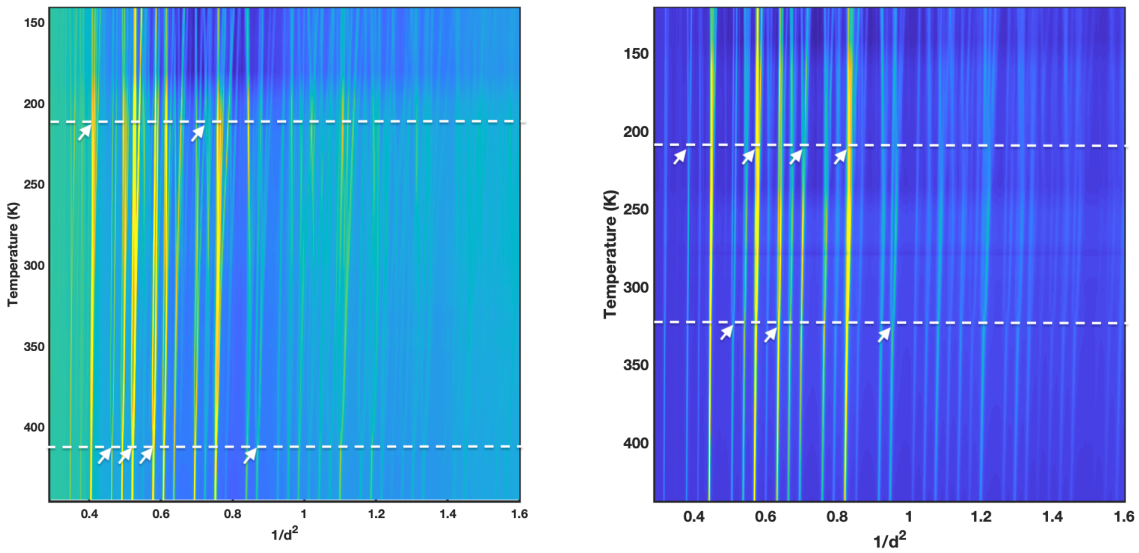

(a) $CsPbBr_3$ (b) $CsPbCl_3$

Figure 6.5: Structural evolution of diffraction patterns as a function of temperature for $CsPbCl_3$ and $CsPbBr_3$, respectively.

lower-symmetry structure.

For the $CsPbCl_3$ sample shown in figure 6.5 b, there are two possible phase transitions occurring at 210 and 330 K. From the literature, there are three successive phase transitions near 310, 315 and 320 K. These results are quite interesting as the sample synthesis is the same as in two studies, but the phase transition behaviour is dramatically different. To confirm the new phase transition, Rietveld refinements should be carried out on these data as future work.

6.4.2 Local structure analysis

In figure 6.3, there are clear structural changes of $CsPbBr_3$ across the measured temperature ranges. The first peak represents the Pb–Br atom pair that has the shortest distance among all the atom pairs. In the average cubic structure, these peaks occur at $d = a/2$. The second peak at 4.3 Å is the mixture of two

atom pairs, Cs-Br and Br-Br. In the high temperature cubic phase, these two bond distance have the same average bond distance, $d = \sqrt{2}a/2$. The third peak belongs to Cs–Pb, whole bond distance is $d = \sqrt{3}a$ from the average structure, as shown in figure 6.1. The first peak remained almost unchanged, indicating the local environment of Pb–Br bond does not vary much. However, the second peak is gradually merged from two peaks at the lowest temperature upon heating. At 140 K, two peaks located at 3.6 and 4.1 Å correspond to Cs–Br and Br–Br respectively.The low temperature phase with space group *Pmbn* has a lower symmetry than the cubic $Pm\bar{3}m$ phase. These two peaks merge at 220 K, indicating the phase transition occurs around this temperature. In the region $r > 5$Å, there is more evidence of the peak changes to support this phase transition. In addition, because of thermal motion, the broadening of the peaks increases with temperature.

In the $CsPbCl_3$ data (figure 6.4), the structural changes are minimal in the low-r region while some are observed at higher r. For example, at 8.43 Å, the peak at low temperatures gradually disappears in the pair distribution function pattern. The first peak at 2.81 Å , corresponding to the Pb-Cl bond, is quite sharp. As seen in the I and Br analogues, this bond is half of the lattice parameter. In PDF, the peak reflects the distribution of distances and the width represents the thermal motion associated with this bond. The second peak corresponding to the Cs–Cl and Cl–Cl bonds is quite broad, partly because of large thermal motion, and the overlapping of two peaks. The shape of the third peak Cs–Pb does not vary significantly, indicating the local environment remains almost the same.

6.4.3 Modelling of the XPDF data

The corrected and normalised $G(r)$ of $CsPbCl_3$ at 450 K was fitted with a series of Gaussian functions. The first 10 peaks from $G(r)$ were used in the modelling. The peak positions were calculated by

$$r = \frac{a\sqrt{h^2 + k^2 + l^2}}{2} \tag{6.4}$$

where a is the unit cell parameter extracted from the Rietveld refinement result and a = 5.61699(6) Å. With a least-square minimisation approach, $G(r)$ was fitted with parameters including the intensity and width σ of each Gaussian function. However, the second and the fifth peak were not well fitted. Additional parameters r_2 and r_5 were then applied to improve the fitting. The improved fit is shown in figure 6.6.

The second peak r_2 corresponds to Cs–Cl and Cl–Cl bonds, and their bond lengths from Rietveld refinement are 3.97 Å. The fitting gives r_2 as 3.63 Å, which is different from the expected distance in average structure. PDF is more accurate in giving bond distances based on the distribution of distances, while in Rietveld analysis only the average over all bonds are given. In addition, the third peak Cs–Pb was well fitted with the average length. Combining these results, the PDF derived distance is shorter reflecting there is large thermal motion associated with Cl atoms while Cs and Pb have a smaller thermal motions. In chapter 3, the halide atom, iodine in $CsPbI_3$ has a large transverse thermal motion normal to the Pb–I–Pb linear bonds. In the cubic phase of $CsPbCl_3$, the Cl atom was refined and has a small U_{11} = 0.0224(20) Å^2 and large $U_{22} = U_{33}$ = 0.1956(11) Å^2 from Rietveld refinement. The overlapping peaks at r_5 makes it difficult to interpret, which includes three different atom pairs Pb–Cl, Cl–Cl and Cs–Cl.

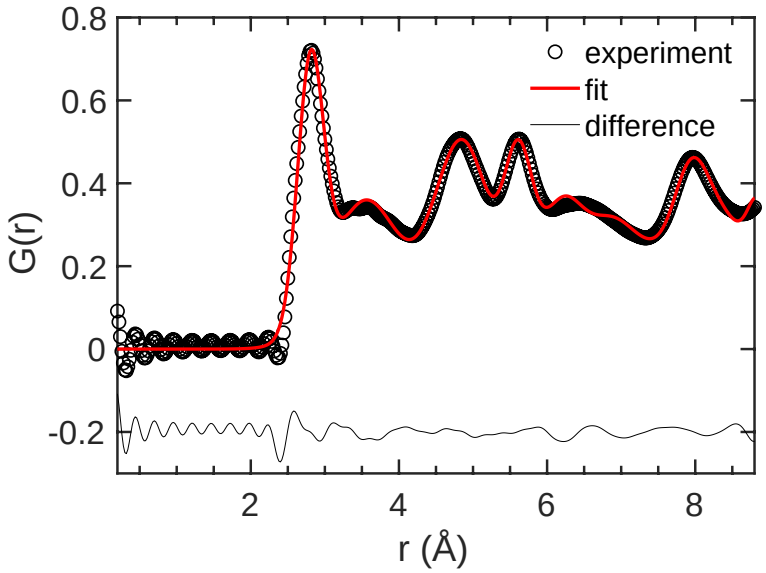

Figure 6.6: The fitting of experimental $G(r)$ of $CsPbCl_3$.

6.5 Future Work

Due to time constraints, more detailed modelling was not performed on both compounds. To study the anharmonicity, I will fit all the cubic phase data with the modelling method at once in section 6.4.3 but with sensible constraints to simulate the temperature effect. The first peak will be fitted to the Morse potential to investigate the bond behaviour of Pb–X.

6.6 Summary

In this chapter, the diffraction patterns of the two materials were examined separately. In both materials, phase transitions were observed but the transition points are not in agreement with the literature. This needs further quantitative confirmation to solve the structures of each phase. X-ray total scattering was performed to investigate the local structure of $CsPbBr_3$ and $CsPbCl_3$. Upon heating, the first transition of two materials occurs near 220 K, and the second phase transition occurs at 330 and 410 K for $CsPbCl_3$ and $CsPbBr_3$ respectively. Local structure analysis indicates that Cs–X and X–X bond distances are

different from the average structure, arising from the large amplitudes of the transverse thermal motions of X atoms. From the pair distribution function analysis, the local structure does not change significantly at the second phase transition for two materials, while they do in the vicinity of the first transition. With further analysis, I anticipate to investigate the anharmonicity of the Pb–X bonds and elucidate the origin of differences between local and average structure.

Chapter 7

Conclusion

The primary goal of this thesis was to understand the local structure of both inorganic perovskites $CsPbX_3$ (X = I, Cl or Br) and hybrid organic-inorganic perovskite $MAPbI_3$. In the journey of exploring that, I have found many more interesting properties of the perovskite materials.

For the perovskite cubic phase of $CsPbI_3$, local structure analysis suggests there are deformations from the average structure, arising from the large transverse atomic motion of iodine atoms. The distance distribution of Pb–I bonds is highly asymmetric and was well fitted to the Morse potential with reasonable vibration frequency and equilibrium bond length. Geometric analysis using GASP on the structural models helped to assess the framework rigidity. By comparing with other perovskites from earlier work [112, 115], the flexibility of PbI_6 framework sits between ScF_3 and $SrTiO_3$, where ScF_3 is extremely flexible and $SrTiO_3$ is relatively rigid.

The investigation of $CsPbBr_3$ and $CsPbCl_3$ using X-ray total scattering suggests the local structure of two materials does not vary significantly with temperature. On the other hand, phase transitions of the two materials are different from what the literature has suggested.

The orientation of the MA cations is the hardest problem to tackle in terms

of structural characterisation [162]. Experimental studies have revealed the rotational dynamics of the hybrid perovskite $MAPbI_3$ occurs at the picosecond timescale. In spite of the methylammonium cation exhibiting orientational disorder, surprisingly limited information can be accessed from conventional crystallographic models. Based on the neutron total scattering data, RMC simulation produced structural models revealing the distributions of molecular orientations and their dependence on temperature and phase. The MA molecules are highly disordered without any preferred orientations in the cubic phase. In the tetragonal phase, an ordering process of the molecules was observed when temperature decreases, despite the molecules being still very disordered. In the low-symmetry orthorhombic phase, MA cations are completely aligned with some thermal motion. The orientational disorder of the molecules has been clearly described for three phases in this work.

Pressure-induced phase transitions in $MAPbI_3$ were studied using neutron powder high-pressure diffraction for the first time. The phase boundary in the pressure-temperature diagram is almost a straight line, indicating the phase behaviour under compression is analogous to cooling. The tetragonal–orthorhombic phase transition would be expected from ambient to low temperature. By carefully tracing structural changes upon compression, this phase transition was successfully reproduced even with different pressure-transmitting fluid. There have been no reports on this phase transition from the literature. The inhomogeneous pressure caused by the lack of PTM could be responsible for the structural diversity. For the $MAPbI_3$, although the structure of the high-pressure phase has not been solved yet, the clear signatures of the first phase transition helps to decipher future pressure studies on $MAPbI_3$.

The application of total scattering + RMC on both inorganic and hybrid organic-inorganic systems demonstrate the usefulness of the method itself. On one hand, the 'snapshot' configurations capture both the average structure

and local structure that describes correlated atomic fluctuations. That is, the distribution of Pb–I distances offers a direct probe into the energy profile. On the other hand, the orientational disorder was properly quantified for the disordered phases of $MAPbI_3$. Another orientational disordered molecular crystal, adamantane has been demonstrated to be disordered over two orientations using RMC method [58].

Related orientationally disordered solids, like formamidinium lead iodide [88] will also benefit from the techniques presented. These are structural problems that can only be poorly tackled by conventional diffraction and Rietveld refinement, where usually it is necessary to define specific positions for atoms, albeit allowing the use of partial occupancy and broad atomic displacement parameters. In such cases, it can be challenging to identify a molecule from the collection of atomic positions, as indeed is the case in the two disordered phases of $MAPbI_3$. This is where total scattering + RMC can be so valuable because as a configuration-based simulation technique, the orientational distribution function can be constructed directly from all the molecules with appropriate interatomic potentials as the constraint.

Electronic and optical properties are determined by the structures and dynamics. The ultimate aim of exploring the fundamental physical properties of these perovskites is to comprehend the structure-property relationship. Despite the limited scope provided for device design, we can still gain some insight from the structural analysis. The vibrational properties of these materials will tell how the bonds behave at the operating temperature of perovskite-based devices. An interplay of the orientational disorder of the molecules and the framework flexibility, in turn, affects the band gap.

Beyond this thesis, future work on these perovskites will involve several aspects. The high pressure phase of $MAPbI_3$ will be investigated using neutron diffraction with a high-resolution diffractometer. Another hybrid perovskite

$FAPbI_3$ will be studied using neutron total scattering and RMC to understand the orientational disorder. The data have been collected already and require further analysis. For the inorganic perovskites $CsPbBr_3$ and $CsPbCl_3$, their structures were not solved using the synchrotron data because of the shading problem. There will be further high-resolution X-ray diffraction experiments on these two compounds. Anharmonicity of the Pb–I bonds will be studied using RMC method as on 3.

Overall, local structure combined with average structure reveals unique properties of the perovskite analogues, including but not exclusive to framework flexibility, bond anharmonicity and orientational disorder. They are of significant importance in understanding the physical and chemical properties for photovoltaic devices, and hopefully they will shed light on further device design in achieving tuneable high-efficiency.

Appendix A

Rietveld results

A.1 $CsPbI_3$

T (K)	a (Å)	a (Å)	b (Å)	c (Å)	R_{wp} (%)	R_p (%)
293	–	10.4670(2)	4.80524(6)	17.7908(3)	2.80	1.92
543	–	10.582(1)	4.8576(9)	17.988(2)	12.01	7.51
553	–	10.5834(9)	4.8594(3)	17.989(1)	11.23	7.37
563	–	10.5825(9)	4.8601(3)	17.998(1)	11.46	7.60
573	–	10.5917(9)	4.8617(3)	18.000(1)	11.03	7.38
583	6.295(2)	10.5911(9)	4.8632(3)	18.002(2)	10.79	7.07
593	6.2903(4)	10.592(1)	4.8622(4)	18.006(2)	11.61	7.39
603	6.2898(3)	10.591(3)	4.864(1)	17.996(4)	11.54	7.47
613	6.2922(2)	–	–	–	11.21	7.73
623	6.2996(2)	–	–	–	10.80	7.62
633	6.3034(2)	–	–	–	10.82	7.57
643	6.3054(2)	–	–	–	11.01	7.50
653	6.3088(2)	–	–	–	10.60	7.55
663	6.3090(2)	–	–	–	10.77	7.67
673	6.31306(4)	–	–	–	3.68	2.74

Table A.1: Refined values of the lattice parameters (a, b and c) for both phases of $CsPbI_3$ obtained by Rietveld refinement of neutron powder diffraction data through all temperatures. In the temperature range 583–603 K the diffraction patterns contains both phases. The final two columns give the weighted (R_{wp}) and unweighted (R_p) R-factors for the Rietveld fit to the diffraction data. Here those parameters for 293 K and 673 K are extremely small compared to others, which is merely an effect of using longer-collected data with better statistics.

T (K)	Pb U_{iso} (Å^2)	Cs U_{iso} (Å^2)	I U_{11} (Å^2)	I U_{22} (Å^2)	Pb U_{iso} (Å^2)	Cs U_{iso}	I U_{iso} (Å^2)
293	–	–	–	–	0.024(1)	0.031(2)	0.019(1)
543	–	–	–	–	0.059(5)	0.073(9)	0.051(5)
553	–	–	–	–	0.049(5)	0.050(8)	0.050(4)
563	–	–	–	–	0.044(5)	0.050)(9)	0.035(4)
573	–	–	–	–	0.051(5)	0.074(9)	0.056(5)
583	0.03(4)	0.10(6)	0.04(9)	0.17(6)	0.059(5)	0.071(9)	0.066(5)
593	0.06(1)	0.15(1)	-0.004(17)	0.31(1)	0.071(7)	0.08(1)	0.061(6)
603	0.058(5)	0.182(7)	0.017(10)	0.282(7)	0.051(10)	0.045(9)	0.048(8)
613	0.061(3)	0.201(5)	0.048(7)	0.279(5)	–	–	–
623	0.057(3)	0.208(5)	0.040(6)	0.298(5)	–	–	–
633	0.058(3)	0.187(5)	0.035(7)	0.288(5)	–	–	–
643	0.065(3)	0.214(5)	0.044(7)	0.304(5)	–	–	–
653	0.074(3)	0.227(5)	0.044(7)	0.335(5)	–	–	–
663	0.083(4)	0.228(5)	0.040(7)	0.328(5)	–	–	–
673	0.066(1)	0.215(2)	0.038(2)	0.303(2)	–	–	–

Table A.2: Refined isotropic thermal displacement parameters U_{iso} and anisotropic thermal displacement parameters U_{ij} for two phases of $CsPbI_3$.

T (K)	Cs x	Cs z	Pb x	Pb z	I1 x	I1 z	I2 x	I2 z	I3 x	I3 z
293	0.4154(3)	0.6711(2)	0.1605(2)	0.4377(1)	0.1640(3)	0.0022(2)	0.2978(2)	0.2869(12)	0.0335(3)	0.6145(2)
543	0.411(1)	0.6709(8)	0.1607(8)	0.4370(5)	0.164(2)	0.0036(9)	0.297(1)	0.287(1)	0.027(1)	0.613(1)
553	0.410(1)	0.6704(7)	0.1604(7)	0.4369(4)	0.1685(16)	0.0033(8)	0.3016(12)	0.2894(9)	0.0203(11)	0.6137(9)
563	0.4127(12)	0.6685(7)	0.1597(8)	0.6116(9)	0.165(2)	0.0040(9)	0.297(1)	0.032(1)	0.032(1)	0.6116(9)
573	0.4150(12)	0.6703(8)	0.1606(7)	0.4362(5)	0.1710(15)	0.0043(8)	0.2998(11)	0.2865(9)	0.0310(11)	0.6144(9)
583	0.4168(12)	0.6694(7)	0.1620(8)	0.4372(5)	0.162(2)	0.003(1)	0.299(1)	0.287(1)	0.030(1)	0.6136(9)
593	0.411(2)	0.670(1)	0.159(1)	0.4377(6)	0.171(2)	0.002(1)	0.304(2)	0.290(1)	0.027(2)	0.614(1)
603	0.411(3)	0.675(2)	0.164(2)	0.439(1)	0.168(4)	0.002(2)	0.299(3)	0.289(2)	0.026(3)	0.618(3)

Table A.3: Fractional atomic coordinates (x, y, z) from Rietveld refinement.

T (K)	a (Å)	Pb U_{iso} (Å^2)	I U_{11} (Å^2)	I U_{22} (Å^2)
300	6.309(2)	−1.6(9)	−9(1)	26(6)
310	6.2968(7)	0.7(6)	−5.9(5)	20(2)
320	6.2989(7)	1.1(5)	−3.8(6)	16(1)
330	6.3007(6)	1.2(4)	−3.7(4)	16(1)
340	6.3023(1)	2.93(9)	1.4(3)	16.1(3)
350	6.3052(1)	3.03(9)	2.2(3)	16.4(3)
360	6.3077(1)	3.15(9)	1.9(3)	15.8(3)
370	6.3106(1)	3.17(10)	2.1(3)	16.3(3)
380	6.3133(1)	3.05(9)	2.5(3)	16.2(3)
390	6.3158(1)	3.38(10)	2.3(3)	16.2(3)
400	6.3184(1)	3.54(10)	2.5(3)	15.6(3)

Table A.4: Lattice parameters and atomic displacement parameters (ADPs) for the Pb and I atoms in the cubic phase of methylammomium lead iodide (space group $Pm\bar{3}m$). The Pb atom has fractional coordinates $(0, 0, 0)$, and the I atom has fractional coordinates $(1/2, 0, 0)$. We do not report the refined positions of the atoms in the methylammonium molecular anion because we do not treat them as more than fitting parameters to represent, together with the ADPs, a highly-disordered arrangement of atoms. A reader can take these from references [60] and [119].

A.2 $CD_3ND_3PbI_3$

T (K)	a (Å)	c (Å)	Pb U_{iso} (Å^2)	I1 U_{iso} (Å^2)	I2 x	I2 U_{iso} (Å^2)
170	8.7929(3)	12.6983(6)	0.95(9)	2.7(3)	0.1993(4)	2.1(2)
180	8.7965(3)	12.6970(6)	1.4(3)	2.7(1)	0.2000(4)	2.4(2)
190	8.8013(3)	12.6974(6)	1.1(1)	3.2(1)	0.1999(4)	2.7(2)
200	8.8078(3)	12.6999(6)	1.5(5)	3.0(1)	0.1999(4)	2.2(2)
210	8.8133(3)	12.6976(6)	1.4(1)	3.1(2)	0.2003(4)	2.1(2)
220	8.8184(3)	12.6980(6)	1.3(1)	3.4(2)	0.2008(4)	2.7(2)
230	8.8230(3)	12.6973(6)	1.4(1)	3.9(2)	0.2026(4)	2.7(2)
240	8.8294(3)	12.6945(6)	1.3(1)	3.7(2)	0.2020(4)	2.8(2)
250	8.8357(3)	12.6956(6)	1.5(1)	4.4(2)	0.2038(5)	2.7(2)
260	8.8411(3)	12.6924(7)	1.7(1)	4.1(2)	0.2047(5)	3.0(3)
270	8.8468(3)	12.6863(7)	1.7(1)	4.3(2)	0.2054(5)	3.3(3)
280	8.8535(3)	12.6844(7)	1.6(1)	4.3(2)	0.2065(5)	3.6(3)
290	8.8601(3)	12.6783(7)	1.7(1)	4.5(2)	0.2084(6)	3.5(3)
300	8.8695(4)	12.6735(8)	3.4(2)	5.8(3)	0.2125(7)	5.6(5)
310	8.8685(4)	12.6594(8)	3.4(2)	6.6(3)	0.2131(8)	7.1(5)
320	8.8804(4)	12.6470(10)	3.5(3)	6.9(4)	0.2125(10)	8.5(7)
330	8.8981(6)	12.6185(19)	4.2(4)	7.3(5)	0.2204(15)	12(2)

Table A.5: Lattice parameters, fractional coordinates and temperature factors for the Pb and I atoms for the tetragonal phases of methylammomium lead iodide (space group $I4/mcm$). Pb has fractional coordinates $(0, 0, 0)$, I1 has fractional coordinates $(x, 1/2 - x, 1/2)$, and I2 has fractional coordinates $(1/2, 1/2, 3/4)$.

T (K)	a (Å)	c (Å)	Pb U_{iso} (Å^2)	I1 x	I1 U_{iso} (Å^2)	I2 U_{iso} (Å^2)
170	8.7929(3)	12.6983(6)	0.95(9)	0.1993(4)	2.7(3)	2.1(2)
180	8.7965(3)	12.6970(6)	1.4(3)	0.2000(4)	2.7(1)	2.4(2)
190	8.8013(3)	12.6974(6)	1.1(1)	0.1999(4)	3.2(1)	2.7(2)
200	8.8078(3)	12.6999(6)	1.5(5)	0.1999(4)	3.0(1)	2.2(2)
210	8.8133(3)	12.6976(6)	1.4(1)	0.2003(4)	3.1(2)	2.1(2)
220	8.8184(3)	12.6980(6)	1.3(1)	0.2008(4)	3.4(2)	2.7(2)
230	8.8230(3)	12.6973(6)	1.4(1)	0.2026(4)	3.9(2)	2.7(2)
240	8.8294(3)	12.6945(6)	1.3(1)	0.2020(4)	3.7(2)	2.8(2)
250	8.8357(3)	12.6956(6)	1.5(1)	0.2038(5)	4.4(2)	2.7(2)
260	8.8411(3)	12.6924(7)	1.7(1)	0.2047(5)	4.1(2)	3.0(3)
270	8.8468(3)	12.6863(7)	1.7(1)	0.2054(5)	4.3(2)	3.3(3)
280	8.8535(3)	12.6844(7)	1.6(1)	0.2065(5)	4.3(2)	3.6(3)
290	8.8601(3)	12.6783(7)	1.7(1)	0.2084(6)	4.5(2)	3.5(3)
300	8.8695(4)	12.6735(8)	3.4(2)	0.2125(7)	5.8(3)	5.6(5)
310	8.8685(4)	12.6594(8)	3.4(2)	0.2131(8)	6.6(3)	7.1(5)
320	8.8804(4)	12.6470(10)	3.5(3)	0.2125(10)	6.9(4)	8.5(7)
330	8.8981(6)	12.6185(19)	4.2(4)	0.2204(15)	7.3(5)	12(2)

Table A.6: Lattice parameters, fractional coordinates and ADPs for the Pb and I atoms for the tetragonal phases of methylammomium lead iodide (space group $I4/mcm$). Pb has fractional coordinates $(0, 0, 0)$, I1 has fractional coordinates $(x, 1/2 - x, 1/2)$, and I2 has fractional coordinates $(1/2, 1/2, 3/4)$. As in Table A.4 we do not report data for the atoms in the methylammonium molecular anion.

T (K)	a (Å)	b (Å)	c (Å)	Pb U_{iso} (Å^2)	I1 x	I1 z	I2 x	I2 y	I2 z	I U_{iso} (Å^2)
10	8.8136(2)	12.5963(2)	8.5644(2)	0.4841(3)	−0.0545(3)	0.1867(2)	0.0165(1)	0.1842(2)	−0.28(3)	-0.14(3)
20	8.8161(3)	12.5961(4)	8.5628(3)	0.4846(5)	−0.0551(5)	0.1867(4)	0.0162(2)	0.1835(3)	−0.27(4)	-0.13(4)
30	8.8201(3)	12.5976(4)	8.5630(3)	0.4845(5)	−0.0545(5)	0.1874(3)	0.0168(2)	0.1845(4)	−0.27(4)	-0.08(5)
40	8.8249(3)	12.6003(4)	8.5620(3)	0.4844(6)	−0.0537(5)	0.1876(4)	0.0172(2)	0.1855(4)	−0.16(5)	-0.02(5)
50	8.8298(3)	12.6032(4)	8.5618(3)	0.4848(6)	−0.0545(6)	0.1875(4)	0.0167(3)	0.1852(4)	−0.19(5)	0.08(6)
60	8.8344(3)	12.6039(4)	8.5625(3)	0.4850(6)	−0.0546(6)	0.1887(4)	0.0177(3)	0.1849(4)	−0.12(5)	0.09(6)
70	8.8398(3)	12.6066(4)	8.5628(3)	0.4842(6)	−0.0553(6)	0.1898(4)	0.0170(3)	0.1855(4)	−0.07(5)	0.25(7)
80	8.8442(3)	12.6078(4)	8.5640(3)	0.4835(7)	−0.0547(6)	0.1896(4)	0.0181(3)	0.1859(5)	0.00(5)	0.20(7)
90	8.8483(3)	12.6109(4)	8.5658(4)	0.4847(7)	−0.0541(6)	0.1897(5)	0.0175(3)	0.1871(5)	0.01(6)	0.35(8)
100	8.8526(3)	12.6137(4)	8.5681(4)	0.4829(7)	−0.0534(6)	0.1907(4)	0.0183(3)	0.1877(5)	0.04(5)	0.38(7)
110	8.8587(3)	12.6172(4)	8.5723(4)	0.4843(7)	−0.0534(7)	0.1907(5)	0.0182(3)	0.1879(5)	0.19(6)	0.62(8)
120	8.8616(3)	12.6199(4)	8.5754(4)	0.4835(8)	−0.0528(7)	0.1920(5)	0.0186(4)	0.1880(5)	0.06(6)	0.74(9)
130	8.8645(4)	12.6220(4)	8.5790(4)	0.4820(8)	−0.0521(7)	0.1914(5)	0.0191(4)	0.1888(5)	0.14(6)	0.67(9)
140	8.8662(4)	12.6247(5)	8.5847(4)	0.4822(9)	−0.0526(7)	0.1933(5)	0.0186(4)	0.1901(6)	0.25(7)	0.69(9)
150	8.8682(4)	12.6267(5)	8.5905(4)	0.4845(10)	−0.0519(8)	0.1942(6)	0.0198(4)	0.1909(6)	0.16(7)	0.91(10)
155	8.8698(4)	12.6280(5)	8.5944(4)	0.4823(10)	−0.0501(8)	0.1939(6)	0.0184(4)	0.1915(6)	0.30(7)	1.00(11)

Table A.7: Lattice parameters, fractional coordinates and temperature factors for the Pb and I atoms for the orthorhombic phases of $MAPbI_3$ (space group *Pnma*). Pb has fractional coordinates $(1/2, 0, 0)$, I1 has fractional coordinates $(x, 1/4, z)$.

T (K)	R_4^+ (Å)	T (K)	M_3^+ (Å)	R_4^+ (Å)	X_5^+ (Å)	R_5^+ (Å)	M_2^+ (Å)
170	0.9061	10	1.1543	0.5526	0.1425	0.1366	0.0222
180	0.8936	20	1.1601	0.5525	0.1376	0.1438	0.0284
190	0.8953	30	1.1445	0.5568	0.1385	0.1320	0.0261
200	0.8953	40	1.1340	0.5562	0.1394	0.1225	0.0188
210	0.8882	50	1.1375	0.5554	0.1358	0.1333	0.0206
220	0.8793	60	1.1295	0.5682	0.1341	0.1218	0.0340
230	0.8471	70	1.1143	0.5638	0.1412	0.1351	0.0384
240	0.8578	80	1.1125	0.5739	0.1475	0.1174	0.0331
250	0.8256	90	1.1009	0.5629	0.1367	0.1208	0.0233
260	0.8096	100	1.0866	0.5682	0.1528	0.1067	0.0268
270	0.7971	110	1.0848	0.5669	0.1403	0.1079	0.0250
280	0.7774	120	1.0723	0.5687	0.1475	0.0986	0.0358
290	0.7435	130	1.0705	0.5706	0.1609	0.0879	0.0233
300	0.6702	140	1.0419	0.5674	0.1591	0.0973	0.0286
310	0.6594	150	1.0267	0.5782	0.1385	0.0777	0.0295
320	0.6702	155	1.0240	0.5491	0.1582	0.0841	0.0215
330	0.5290						

Table A.8: Symmetry mode amplitudes of $MAPbI_3$.

Appendix B

RMC results

B.1 $CsPbI_3$

T(K)	573	613	643	673
Cs U_{iso} (Å^2)	0.210(11)	0.217(10)	0.216(6)	0.221(12)
Pb U_{iso} (Å^2)	0.076(4)	0.081(5)	0.082(5)	0.083(4)
I U_{22} (Å^2)	0.30(4)	0.29(4)	0.30(4)	0.29(4)
I U_{11} (Å^2)	0.014(3)	0.016(3)	0.013(2)	0.015(3)

Table B.1: From the supercell configuration, an average unit cell is produced to show the small displacements of each atom. 30 configurations have been used for calculations at each temperature to get good statistics. This can be a direct comparison with refined anisotropic displacement parameters in A.2.

Bibliography

[1] S. Kazim, M. K. Nazeeruddin, M. Grätzel, S. Ahmad, *Angewandte Chemie - International Edition* **2014**, *53*, 2812–2824.

[2] D. M. Chapin, C. S. Fuller, G. L. Pearson, *Journal of Applied Physics* **1954**, *25*, 676–677.

[3] K. Yoshikawa, H. Kawasaki, W. Yoshida, T. Irie, K. Konishi, K. Nakano, T. Uto, D. Adachi, M. Kanematsu, H. Uzu, K. Yamamoto, *Nature Energy* **2017**, *2*, 17032.

[4] J. Britt, C. Ferekides, *Applied Physics Letters* **1993**, *62*, 2851–2852.

[5] M. Powalla, S. Paetel, D. Hariskos, R. Wuerz, F. Kessler, P. Lechner, W. Wischmann, T. M. Friedlmeier, *Engineering* **2017**, *3*, 445–451.

[6] B. O'Regan, M. Grätzel, *Nature* **1991**, *353*, 737–740.

[7] A. Kojima, K. Teshima, Y. Shirai, T. Miyasaka, *Journal of the American Chemical Society* **2009**, *131*, 6050–6051.

[8] C. G. Wu, C. H. Chiang, Z. L. Tseng, M. K. Nazeeruddin, A. Hagfeldt, M. Grätzel, *Energy and Environmental Science* **2015**, *8*, 2725–2733.

[9] A. R. Chakhmouradian, P. M. Woodward, *Physics and Chemistry of Minerals* **2014**, *41*, 387–391.

[10] D. A. Egger, A. M. Rappe, L. Kronik, *Accounts of Chemical Research* **2016**, *49*, 573–581.

[11] E. Salje, *Philosophical Transactions of the Royal Society A: Mathematical Physical and Engineering Sciences* **1989**, *328*, 409–416.

[12] V. M. Goldschmidt, *Die Naturwissenschaften* **1926**, *14*, 477–485.

[13] J. He, C. Franchini, *Physical Review B - Condensed Matter and Materials Physics* **2014**, *89*, 1–8.

[14] Z. Li, M. Yang, J.-s. S. Park, S.-h. H. Wei, J. J. Berry, K. Zhu, *Chemistry of Materials* **2016**, *28*, 284–292.

[15] G. Kieslich, S. Sun, A. K. Cheetham, *Chemical Science* **2015**, *6*, 3430–3433.

[16] Y. Liao, H. Liu, W. Zhou, D. Yang, Y. Shang, Z. Shi, B. Li, X. Jiang, L. Zhang, L. N. Quan, R. Quintero-Bermudez, B. R. Sutherland, Q. Mi, E. H. Sargent, Z. Ning, *Journal of the American Chemical Society* **2017**, *139*, 6693–6699.

[17] R. L. Milot, R. J. Sutton, G. E. Eperon, A. A. Haghighirad, J. Martinez Hardigree, L. Miranda, H. J. Snaith, M. B. Johnston, L. M. Herz, *Nano Letters* **2016**, *16*, 7001–7007.

[18] M. Saliba, *Energy & Environmental Science* **2016**, *9*, 1989–1997.

[19] J. Lin, M. Lai, L. Dou, C. S. Kley, H. Chen, F. Peng, J. Sun, D. Lu, S. A. Hawks, C. Xie, F. Cui, A. P. Alivisatos, D. T. Limmer, P. Yang, *Nature Materials* **2018**, *17*, 261–267.

[20] A. Swarnkar, A. R. Marshall, E. M. Sanehira, B. D. Chernomordik, D. T. Moore, J. A. Christians, T. Chakrabarti, J. M. Luther, *Science* **2016**, *354*, 92 LP –95.

[21] K. Wang, Z. Jin, L. Liang, H. Bian, D. Bai, H. Wang, J. Zhang, Q. Wang, L. Shengzhong, *Nature Communications* **2018**, *9*, 4544.

[22] Q. Chen, J. Wu, X. Ou, B. Huang, J. Almutlaq, A. A. Zhumekenov, X. Guan, S. Han, L. Liang, Z. Yi, J. Li, X. Xie, Y. Wang, Y. Li, D. Fan, D. B. L. Teh, A. H. All, O. F. Mohammed, O. M. Bakr, T. Wu, M. Bettinelli, H. Yang, W. Huang, X. Liu, *Nature* **2018**, *561*, 88–93.

[23] M. Kulbak, D. Cahen, G. Hodes, *Journal of Physical Chemistry Letters* **2015**, *6*, 2452–2456.

[24] W. Li, Z. Wang, F. Deschler, S. Gao, R. H. Friend, A. K. Cheetham, *Nature Reviews Materials* **2017**, *2*, 16099.

[25] G. Kieslich, A. L. Goodwin, *Materials Horizons* **2017**, *4*, 362–366.

[26] J. M. Frost, K. T. Butler, F. Brivio, C. H. Hendon, M. van Schilfgaarde, A. Walsh, *Nano Letters* **2014**, *14*, 2584–2590.

[27] S. Van Reenen, M. Kemerink, H. J. Snaith, *Journal of Physical Chemistry Letters* **2015**, *6*, 3808–3814.

[28] P. Calado, A. M. Telford, D. Bryant, X. Li, J. Nelson, B. C. O'Regan, P. R. Barnes, *Nature Communications* **2016**, *7*, 1–10.

[29] H. W. Chen, N. Sakai, M. Ikegami, T. Miyasaka, *Journal of Physical Chemistry Letters* **2015**, *6*, 164–169.

[30] Z. Fan, J. Xiao, K. Sun, L. Chen, Y. Hu, J. Ouyang, K. P. Ong, K. Zeng, J. Wang, *Journal of Physical Chemistry Letters* **2015**, *6*, 1155–1161.

[31] G. E. Eperon, G. M. Paternò, R. J. Sutton, A. Zampetti, A. A. Haghighirad, F. Cacialli, H. J. Snaith, *Journal of Materials Chemistry A* **2015**, *3*, 19688–19695.

[32] C. G. Wu, C. H. Chiang, Z. L. Tseng, M. K. Nazeeruddin, A. Hagfeldt, M. Grätzel, *Energy and Environmental Science* **2015**, *8*, 2725–2733.

[33] N.-K. Kim, Y. H. Min, S. Noh, E. Cho, G. Jeong, M. Joo, S.-W. Ahn, J. S. Lee, S. Kim, K. Ihm, H. Ahn, Y. Kang, H.-S. Lee, D. Kim, *Scientific Reports* **2017**, *7*, 4645.

[34] Q. Han, S. H. Bae, P. Sun, Y. T. Hsieh, Y. Yang, Y. S. Rim, H. Zhao, Q. Chen, W. Shi, G. Li, Y. Yeng, *Advanced Materials* **2016**, *28*, 2253–2258.

[35] W. S. Yang, J. H. Noh, N. J. Jeon, Y. C. Kim, S. Ryu, J. Seo, S. I. Seok, *Science* **2015**, *348*, 1234–1237.

[36] J. Even, M. Carignano, C. Katan, *Nanoscale* **2016**, *8*, 6222–6236.

[37] T. Chen, W.-L. Chen, B. J. Foley, J. Lee, J. P. C. Ruff, J. Y. P. Ko, C. M. Brown, L. W. Harriger, D. Zhang, C. Park, M. Yoon, Y.-M. Chang, J. J. Choi, S.-H. Lee, *Proceedings of the National Academy of Sciences* **2017**, *114*, 7519–7524.

[38] O. Yaffe, Y. Guo, L. Z. Tan, D. A. Egger, T. Hull, C. C. Stoumpos, F. Zheng, T. F. Heinz, L. Kronik, M. G. Kanatzidis, J. S. Owen, A. M. Rappe, M. A. Pimenta, L. E. Brus, *Physical Review Letters* **2017**, *118*, 1–6.

[39] C. S. Ponseca, T. J. Savenije, M. Abdellah, K. Zheng, A. Yartsev, T. Pascher, T. Harlang, P. Chabera, T. Pullerits, A. Stepanov, J. P. Wolf, V. Sundström, *Journal of the American Chemical Society* **2014**, *136*, 5189–5192.

[40] S. D. Stranks, V. M. Burlakov, T. Leijtens, J. M. Ball, A. Goriely, H. J. Snaith, *Physical Review Applied* **2014**, *2*, 1–8.

[41] H. Zhou, Q. Chen, G. Li, S. Luo, T.-b. Song, H.-S. Duan, Z. Hong, J. You, Y. Liu, Y. Yang, *Science* **2014**, *345*, 542–546.

[42] I. C. Smith, M. D. Smith, A. Jaffe, Y. Lin, H. I. Karunadasa, *Chemistry of Materials* **2017**, *29*, 1868–1884.

[43] S. Ryu, J. Seo, S. S. Shin, Y. C. Kim, N. J. Jeon, J. H. Noh, S. I. Seok, *Journal of Materials Chemistry A* **2015**, *3*, 3271–3275.

[44] F. Ye, W. Yang, D. Luo, R. Zhu, Q. Gong, *Journal of Semiconductors* **2017**, *38*, 011003.

[45] D. Ghosh, P. Walsh Atkins, M. S. Islam, A. B. Walker, C. Eames, *ACS Energy Letters* **2017**, *2*, 2424–2429.

[46] H. Choi, J. Jeong, H. B. Kim, S. Kim, B. Walker, G. H. Kim, J. Y. Kim, *Nano Energy* **2014**, *7*, 80–85.

[47] K. Miyata, D. Meggiolaro, M. T. Trinh, P. P. Joshi, E. Mosconi, S. C. Jones, F. De Angelis, X.-Y. Zhu, *Science Advances* **2017**, *3*, e1701217.

[48] J. S. Bechtel, A. Van der Ven, *Physical Review Materials* **2018**, *2*, 025401.

[49] G. M. Bernard, R. E. Wasylishen, C. I. Ratcliffe, V. Terskikh, Q. Wu, J. M. Buriak, T. Hauger, *Journal of Physical Chemistry A* **2018**, *122*, 1560–1573.

[50] T. Chen, B. J. Foley, B. Ipek, M. Tyagi, J. R. D. Copley, C. M. Brown, J. J. Choi, S.-H. Lee, *Physical Chemistry Chemical Physics* **2015**, *17*, 31278–31286.

[51] Y. Guo, O. Yaffe, D. W. Paley, A. N. Beecher, T. D. Hull, G. Szpak, J. S. Owen, L. E. Brus, M. A. Pimenta, *Physical Review Materials* **2017**, *1*, 042401.

[52] F. Brivio, J. M. Frost, J. M. Skelton, A. J. Jackson, O. J. Weber, M. T. Weller, A. R. Goñi, A. M. Leguy, P. R. Barnes, A. Walsh, *Physical Review B - Condensed Matter and Materials Physics* **2015**, *92*, 1–8.

[53] J. H. Heo, S. H. Im, J. H. Noh, T. N. Mandal, C.-s. Lim, J. A. Chang, Y. H. Lee, H.-j. Kim, A. Sarkar, M. K. Nazeeruddin, M. Grätzel, S. I. Seok, *Nature Photonics* **2013**, *7*, 486–491.

[54] D. C. Jordan, S. R. Kurtz, *Progress in Photovoltaics: Research and Applications* **2013**, *21*, 12–29.

[55] T. A. Berhe, W. N. Su, C. H. Chen, C. J. Pan, J. H. Cheng, H. M. Chen, M. C. Tsai, L. Y. Chen, A. A. Dubale, B. J. Hwang, *Energy and Environmental Science* **2016**, *9*, 323–356.

[56] F. Hao, C. C. Stoumpos, D. H. Cao, R. P. Chang, M. G. Kanatzidis, *Nature Photonics* **2014**, *8*, 489–494.

[57] K. H. Michel, K. Parlinski, *Physical Review B* **1985**, *31*, 1823–1835.

[58] E. O. Beake, M. G. Tucker, M. T. Dove, A. E. Phillips, *ChemPhysChem* **2017**, *18*, 459–464.

[59] M. T. Dove, R. M. Lynden-Bell, *Journal of Physics C: Solid State Physics* **1986**, *19*, 3343–3363.

[60] M. T. Weller, O. J. Weber, P. F. Henry, M. D. Pumpo, T. C. Hansen, *Chemical Communications* **2015**, *51*, 4180–4183.

[61] T. Chen, B. J. Foley, B. Ipek, M. Tyagi, J. R. D. Copley, C. M. Brown, J. J. Choi, S.-H. Lee, *Physical Chemistry Chemical Physics* **2015**, *17*, 31278–31286.

[62] B. M. Powell, G. Dolling, *Canadian Journal of Chemistry* **1988**, *66*, 897–903.

[63] R. W. Havenith, H. D. de Gier, R. Broer, *Molecular Physics* **2012**, *110*, 2445–2454.

[64] S. K. Garg, *The Journal of Chemical Physics* **1977**, *66*, 2517–2524.

[65] M. T. Dove, G. S. Pawley, *Journal of Physics C: Solid State Physics* **1984**, *17*, 6581–6599.

[66] B. J. Wuensch, K. W. Eberman, *Jom* **2000**, *52*, 19–21.

[67] I. K. Jeong, T. Proffen, F. Mohiuddin-Jacobs, S. J. Billinge, *Journal of Physical Chemistry A* **1999**, *103*, 921–924.

[68] P. W. H. Bragg, W. L. Bragg, **1913**, *17*, 428–438.

[69] J. R. Santisteban, L. Edwards, A. Steuwer, P. J. Withers, *Journal of Applied Crystallography* **2001**, *34*, 289–297.

[70] G. L. Squires, *Introduction to the Theory of Thermal Neutron Scattering*, Cambridge University Press, Cambridge, **2012**.

[71] A. C. Hannon, *Nuclear Instruments and Methods in Physics Research Section A: Accelerators Spectrometers Detectors and Associated Equipment* **2005**, *551*, 88–107.

[72] ISIS-II working report, `https://www.isis.stfc.ac.uk/Pages/isis-ii-working-group-report16266.pdf`.

[73] J. P. Sutter, P. A. Chater, M. R. Hillman, D. S. Keeble, M. G. Tucker, H. Wilhelm in, **2016**, p. 040005.

[74] H. M. Rietveld, *Journal of Applied Crystallography* **1969**, *2*, 65–71.

[75] B. H. Toby, *Powder Diffraction* **2006**, *21*, 67–70.

[76] B. H. Toby, *Journal of Applied Crystallography* **2001**, *34*, 210–213.

[77] B. H. Toby, R. B. Von Dreele, *Powder Diffraction* **2014**, *29*, S2–S6.

[78] P Scardi, L. B. Mccusker, R. B. V. Dreele, D. E. Cox, D Loue, *Journal of Applied Crystallography* **1999**, 36–50.

[79] R. Smith, Refinement of time-of-flight Profile Parameters in GSAS, `https://www.isis.stfc.ac.uk/Pages/refinement-of-profile-parameters-with-polaris-data.pdf`.

[80] J. Thompson, P., Cox, D.E., Hasting, *Jorunal of Apply Crystallographica* **1987**, *20*, 79–83.

[81] T Egami, S. J. L. Billinge, *Underneath the Bragg peaks, Structural analysis of complex materials*, Elsevier, **2012**.

[82] W. G. Williams, R. M. Ibberson, P. Day, J. E. Enderby, *Physica B: Condensed Matter* **1997**, *241-243*, 234–236.

[83] Upgraded Polaris provides successful initial results, `https://www.isis.stfc.ac.uk/Pages/Upgraded-Polaris-provides-successful-initial-results.aspx` (visited on 10/18/2019).

[84] C. L. Bull, N. P. Funnell, M. G. Tucker, S Hull, D. J. Francis, W. G. Marshall, *High Pressure Research* **2016**, *36*, 493–511.

[85] Diamond XPDF (I15-1), `https://www.diamond.ac.uk/Instruments/Crystallography/I15-1.html` (visited on 10/18/2019).

[86] C. C. Stoumpos, C. D. Malliakas, J. A. Peters, Z. Liu, M. Sebastian, J. Im, T. C. Chasapis, A. C. Wibowo, D. Y. Chung, A. J. Freeman, B. W. Wessels, M. G. Kanatzidis, *Crystal Growth and Design* **2013**, *13*, 2722–2727.

[87] T. Baikie, Y. Fang, J. M. Kadro, M. Schreyer, F. Wei, S. G. Mhaisalkar, M. Graetzel, T. J. White, *Journal of Materials Chemistry A* **2013**, *1*, 5628–5641.

[88] T. Chen, B. J. Foley, C. Park, C. M. Brown, L. W. Harriger, J. Lee, J. Ruff, M. Yoon, J. J. Choi, S.-H. Lee, *Science Advances* **2016**, *2*, e1601650.

[89] T Sakuma, *Solid State Ionics* **2002**, *154-155*, 237–242.

[90] J. Li, H. Zhang, S. Wang, D. Long, M. Li, Y. Guo, Z. Zhong, K. Wu, D. Wang, T. Zhang, *RSC Advances* **2017**, *7*, 54002–54007.

[91] S. J. L. Billinge, M. G. Kanatzidis, *Chemical Communications* **2004**, 749.

[92] D. A. Keen, *Journal of Applied Crystallography* **2001**, *34*, 172–177.

[93] M. T. Dove, M. G. Tucker, D. a. Keen, *European Journal of Mineralogy* **2002**, *14*, 331–348.

[94] A. K. Soper, E. R. Barney, *Journal of Applied Crystallography* **2012**, *45*, 1314–1317.

[95] A. K. Soper, *Molecular Physics* **2009**, *107*, 1667–1684.

[96] R. L. Mcgreevy, L. Pusztai, *Molecular Simulation* **1988**, *1*, 359–367.

[97] M. G. Tucker, D. A. Keen, M. T. Dove, A. L. Goodwin, Q. Hui, *Journal of Physics: Condensed Matter* **2007**, *19*, 335218.

[98] M. Tucker, M. Dove, A. Goodwin, D. Keen, RMCProfile User Manual, **2012**, `http://www.rmcprofile.org/imagesFhj/b/ba/Rmcprofile_v6_manual.pdf`.

[99] S. S. A. Wells, M. M. T. M. Dove, M. M. G. Tucker, *Journal of Physics: Condensed Matter* **2002**, *14*, 4567–4584.

[100] S. A. Wells, A. Sartbaeva, *Molecular Simulation* **2015**, *41*, 1409–1421.

[101] G. E. Eperon, G. M. Paternò, R. J. Sutton, A. Zampetti, A. A. Haghighirad, F. Cacialli, H. J. Snaith, *Journal of Materials Chemistry A* **2015**, *3*, 19688–19695.

[102] D. Trots, S. Myagkota, *Journal of Physics and Chemistry of Solids* **2008**, *69*, 2520–2526.

[103] A. Marronnier, G. Roma, S. Boyer-Richard, L. Pedesseau, J. M. Jancu, Y. Bonnassieux, C. Katan, C. C. Stoumpos, M. G. Kanatzidis, J. Even, *ACS Nano* **2018**, *12*, 3477–3486.

[104] R. J. Sutton, M. R. Filip, A. A. Haghighirad, N. Sakai, B. Wenger, F. Giustino, H. J. Snaith, *ACS Energy Letters* **2018**, *3*, 1787–1794.

[105] J Hutton, R. J. Nelmes, G. M. Meyer, V. R. Eiriksson, *Journal of Physics C: Solid State Physics* **1979**, *12*, 5393–5410.

[106] J Hutton, R. J. Nelmes, *Journal of Physics C: Solid State Physics* **1981**, *14*, 1713–1736.

[107] Y. Fujii, S. Hoshino, Y. Yamada, G. Shirane, *Physical Review B* **1974**, *9*, 4549–4559.

[108] A. Marronnier, H. Lee, B. Geffroy, J. Even, Y. Bonnassieux, G. Roma, *Journal of Physical Chemistry Letters* **June 15, 2017**, *8*, 2659–2665.

[109] R. X. Yang, J. M. Skelton, E. L. Da Silva, J. M. Frost, A. Walsh, *Journal of Physical Chemistry Letters* **2017**, *8*, 4720–4726.

[110] O. Arnold et al., *Nuclear Instruments and Methods in Physics Research Section A: Accelerators Spectrometers Detectors and Associated Equipment* **Nov. 2014**, *764*, 156–166.

[111] A. C. Larson, R. B. V. Dreele, General Structure Analysis System (GSAS), Technical Report 86-748, Los Alamos National Laboratory, NM, U.S.A., **1994**.

[112] Q. Hui, M. G. Tucker, M. T. Dove, S. A. Wells, D. A. Keen, *Journal of Physics: Condensed Matter* **2005**, *17*, S111–S124.

[113] A. L. Goodwin, S. A. T. Redfern, M. T. Dove, D. A. Keen, M. G. Tucker, *Physical Review B* **2007**, *76*, 174114.

[114] S. Wells, M. Dove, M. Tucker, *Journal of Applied Crystallography* **2004**, *37*, 536–544.

[115] M. T. Dove, J. Du, D. A. Keen, M. G. Tucker, A. E. Phillips, **in press**.

[116] M. T. Dove, *Structure and dynamics*, Oxford University Press, Oxford, **2002**.

[117] A. M. Glazer, *Acta Crystallographica Section B Structural Crystallography and Crystal Chemistry* **1972**, *28*, 3384–3392.

[118] A. M. Glazer, *Acta Crystallographica Section A* **Nov. 1975**, *31*, 756–762.

[119] P. S. Whitfield, N Herron, W. E. Guise, K Page, Y. Q. Cheng, I Milas, M. K. Crawford, *Scientific Reports* **2016**, *6*, 35685.

[120] C. L. Farrow, P. Juhas, J. W. Liu, D. Bryndin, E. S. Božin, J. Bloch, T. Proffen, S. J. L. Billinge, *Journal of Physics: Condensed Matter* **2007**, *19*, 335219.

[121] J. Li, P. Rinke, *Physical Review B* **2016**, *94*, 1–12.

[122] A. M. Leguy, J. M. Frost, A. P. McMahon, V. G. Sakai, W. Kochelmann, C. Law, X. Li, F. Foglia, A. Walsh, B. C. O'Regan, J. Nelson, J. T. Cabral, P. R. Barnes, *Nature Communications* **2015**, DOI `10.1038/ncomms8124`.

[123] A. K. Soper, **2012**.

[124] M. L. Klein, I. R. McDonald, Y. Ozaki, *The Journal of Chemical Physics* **1983**, *79*, 5579–5587.

[125] G Dolling, B. M. Powell, V. F. Sears, English, *Molecular Physics* **June 1979**, *37*, 1859–1883.

[126] A. Mehdizadeh, S. F. Akhtarianfar, S. Shojaei, *Journal of Physical Chemistry C* **2019**, *123*, 6725–6734.

[127] J. Du, A. E. Phillips, D. C. Arnold, D. A. Keen, M. G. Tucker, M. T. Dove, "Structural study of bismuth ferrite, $BiFeO_3$, by neutron total scattering and the reverse Monte Carlo method", **In press**.

[128] J. Du, PhD dissertation, Queen Mary university of London, **2018**.

[129] R. Cowley, *Advances in Physics* **1980**, *29*, 1–110.

[130] M. A. Carpenter, A. I. Bacerro, F. Seiferi, *American Mineralogist* **2001**, *86*, 348–363.

[131] J. R. Harwell, J. L. Payne, M. T. Sajjad, F. J. Heutz, D. M. Dawson, P. S. Whitfield, J. T. Irvine, I. D. Samuel, M. A. Carpenter, *Physical Review Materials* **2018**, *2*, 1–13.

[132] N. Onoda-Yamamuro, T. Matsuo, H. Suga, *Journal of Physics and Chemistry of Solids* **1990**, *51*, 1383–1395.

[133] O. Knop, R. E. Wasylishen, M. A. White, T. S. Cameron, M. J. M. V. Oort, *Canadian Journal of Chemistry* **2006**, *68*, 412–422.

[134] J. M. Perez-Mato, D. Orobengoa, M. I. Aroyo, *Mode crystallography of distorted structures*, *Vol. 66*, International Union of Crystallography, **2010**, pp. 558–590.

[135] D. Orobengoa, C. Capillas, M. I. Aroyo, J. M. Perez-Mato, *Journal of Applied Crystallography* **2009**, *42*, 820–833.

[136] M. Szafrański, A. Katrusiak, *Journal of Physical Chemistry Letters* **2016**, *7*, 3458–3466.

[137] H. N. Lee, H. M. Christen, M. F. Chisholm, C. M. Rouleau, D. H. Lowndes, *Nature* **2005**, *433*, 395–399.

[138] A. Jaffe, Y. Lin, C. M. Beavers, J. Voss, W. L. Mao, H. I. Karunadasa, *ACS Central Science* **2016**, *2*, 201–209.

[139] Y. Wang, X. Lü, W. Yang, T. Wen, L. Yang, X. Ren, L. Wang, Z. Lin, Y. Zhao, *Journal of the American Chemical Society* **2015**, *137*, 11144–11149.

[140] S. Jiang, Y. Fang, R. Li, H. Xiao, J. Crowley, C. Wang, T. J. White, W. A. Goddard, Z. Wang, T. Baikie, J. Fang, *Angewandte Chemie - International Edition* **2016**, *55*, 6540–6544.

[141] I. P. Swainson, M. G. Tucker, D. J. Wilson, B. Winkler, V. Milman, *Chemistry of Materials* **2007**, *19*, 2401–2405.

[142] L. Wang, K. Wang, G. Xiao, Q. Zeng, B. Zou, *Journal of Physical Chemistry Letters* **2016**, *7*, 5273–5279.

[143] F. Capitani, C. Marini, S. Caramazza, P. Postorino, G. Garbarino, M. Hanfland, A. Pisanu, P. Quadrelli, L. Malavasi, *Journal of Applied Physics* **2016**, *119*, DOI 10.1063/1.4948577.

[144] A. Arakcheeva, V. Svitlyk, E. Polini, L. Henry, D. Chernyshov, A. Sienkiewicz, G. Giriat, A. Glushkova, M. Kollar, B. Náfrádi, L. Forro, E. Horváth, *Acta Crystallographica Section B Structural Science Crystal Engineering and Materials* **2019**, *75*, 361–370.

[145] X. Lü, W. Yang, Q. Jia, H. Xu, *Chem. Sci.* **2017**, *8*, 6764–6776.

[146] P. Postorino, L. Malavasi, *Journal of Physical Chemistry Letters* **2017**, *8*, 2613–2622.

[147] R. Zhang, W. Cai, T. Bi, N. Zarifi, T. Terpstra, C. Zhang, Z. V. Verdeny, E. Zurek, S. Deemyad, *Journal of Physical Chemistry Letters* **2017**, *8*, 3457–3465.

[148] G. J. Piermarini, S. Block, J. Barnett, *Journal of Applied Physics* **1973**, *44*, 5377–5382.

[149] S. Klotz, J.-C. Chervin, P. Munsch, G. Le Marchand, *Journal of Physics D: Applied Physics* **2009**, *42*, 075413.

[150] H. Y. Playford, M. G. Tucker, C. L. Bull, *Journal of Applied Crystallography* **2017**, *50*, 87–95.

[151] H. Fang, A. E. Phillips, M. T. Dove, M. G. Tucker, A. L. Goodwin, *Physical Review B - Condensed Matter and Materials Physics* **2013**, *88*, 1–8.

[152] F. Birch, *Journal of Applied Physics* **1938**, *9*, 279–288.

[153] F. D. Murnaghan, *American Journal of Mathematics* **1937**, *59*, 235.

[154] M. J. Cliffe, A. L. Goodwin, *Journal of Applied Crystallography* **2012**, *45*, 1321–1329.

[155] Q. Wang, X. Zhang, Z. Jin, J. Zhang, Z. Gao, Y. Li, S. F. Liu, *ACS Energy Letters* **2017**, *2*, 1479–1486.

[156] S. Hirotsu, J. Harada, M. Iizumi, K. Gesi, *Journal of the Physical Society of Japan* **1974**, *37*, 1393–1398.

[157] Y. Fujii, S. Hoshino, Y. Yamada, G. Shirane, *Physical Review B* **1974**, *9*, 4549–4559.

[158] C. J. Howard, H. T. Stokes, *Acta Crystallographica Section A: Foundations of Crystallography* **2005**, *61*, 93–111.

[159] M. R. Linaburg, E. T. McClure, J. D. Majher, P. M. Woodward, *Chemistry of Materials* **2017**, *29*, 3507–3514.

[160] M. Basham, J. Filik, M. T. Wharmby, P. C. Y. Chang, B. El Kassaby, M. Gerring, J. Aishima, K. Levik, B. C. A. Pulford, I. Sikharulidze, D. Sneddon, M. Webber, S. S. Dhesi, F. Maccherozzi, O. Svensson, S. Brockhauser, G. Náray, A. W. Ashton, *Journal of Synchrotron Radiation* **2015**, *22*, 853–858.

[161] A. K. Soper, E. R. Barney, *Journal of Applied Crystallography* **2011**, *44*, 714–726.

[162] C. Quarti, E. Mosconi, F. De Angelis, *Phys. Chem. Chem. Phys.* **2015**, *17*, 9394–9409.